The Mercury Dual Imaging System on the MESSENGER Spacecraft

**S. Edward Hawkins, III · John D. Boldt · Edward H. Darlington · Raymond Espiritu ·
Robert E. Gold · Bruce Gotwols · Matthew P. Grey · Christopher D. Hash ·
John R. Hayes · Steven E. Jaskulek · Charles J. Kardian, Jr. · Mary R. Keller ·
Erick R. Malaret · Scott L. Murchie · Patricia K. Murphy · Keith Peacock ·
Louise M. Prockter · R. Alan Reiter · Mark S. Robinson · Edward D. Schaefer ·
Richard G. Shelton · Raymond E. Sterner, II · Howard W. Taylor ·
Thomas R. Watters · Bruce D. Williams**

Abstract The Mercury Dual Imaging System (MDIS) on the MESSENGER spacecraft will
provide critical measurements tracing Mercury's origin and evolution. MDIS consists of a
monochrome narrow-angle camera (NAC) and a multispectral wide-angle camera (WAC).
The NAC is a 1.5° field-of-view (FOV) off-axis reflector, coaligned with the WAC, a four-
element refractor with a 10.5° FOV and 12-color filter wheel. The focal plane electronics
of each camera are identical and use a $1{,}024 \times 1{,}024$ Atmel (Thomson) TH7888A charge-
coupled device detector. Only one camera operates at a time, allowing them to share a com-
mon set of control electronics. The NAC and the WAC are mounted on a pivoting platform
that provides a 90° field-of-regard, extending 40° sunward and 50° anti-sunward from the
spacecraft $+Z$-axis—the boresight direction of most of MESSENGER's instruments. On-
board data compression provides capabilities for pixel binning, remapping of 12-bit data
into 8 bits, and lossless or lossy compression. MDIS will acquire four main data sets at Mer-
cury during three flybys and the two-Mercury-solar-day nominal mission: a monochrome

S.E. Hawkins, III (✉) · J.D. Boldt · E.H. Darlington · R.E. Gold · B. Gotwols · M.P. Grey · J.R. Hayes ·
S.E. Jaskulek · C.J. Kardian, Jr. · M.R. Keller · S.L. Murchie · P.K. Murphy · K. Peacock ·
L.M. Prockter · R.A. Reiter · E.D. Schaefer · R.G. Shelton · R.E. Sterner, II · H.W. Taylor ·
B.D. Williams
The Johns Hopkins University Applied Physics Laboratory, Laurel, MD 20723, USA
e-mail: ed.hawkins@jhuapl.edu

R. Espiritu · C.D. Hash · E.R. Malaret
Applied Coherent Technology, Herndon, VA 20170, USA

M.S. Robinson
School of Earth and Space Exploration, Arizona State University, Box 871404, Tempe, AZ 85287-1404,
USA

T.R. Watters
Center for Earth and Planetary Studies, National Air and Space Museum, Smithsonian Institution,
Washington, DC 20013, USA

global image mosaic at near-zero emission angles and moderate incidence angles, a stereo-complement map at off-nadir geometry and near-identical lighting, multicolor images at low incidence angles, and targeted high-resolution images of key surface features. These data will be used to construct a global image base map, a digital terrain model, global maps of color properties, and mosaics of high-resolution image strips. Analysis of these data will provide information on Mercury's impact history, tectonic processes, the composition and emplacement history of volcanic materials, and the thickness distribution and compositional variations of crustal materials. This paper summarizes MDIS's science objectives and technical design, including the common payload design of the MDIS data processing units, as well as detailed results from ground and early flight calibrations and plans for Mercury image products to be generated from MDIS data.

1 Introduction

Mariner 10, from its three flybys of Mercury in 1974–1975, provided a reconnaissance view of one hemisphere and measured the planet's magnetic field and interaction with the space environment. No spacecraft has returned in the intervening 30 years, however, and our knowledge of Mercury's composition, origin, and evolution is therefore limited. From its high bulk density, Mariner 10 observations (Murray 1975), and Earth-based remote sensing, Mercury is known to have a high metal-to-silicate ratio, a crust low in FeO (Rava and Hapke 1987; Vilas 1988; Blewett et al. 1997; Robinson and Taylor 2001), and an exosphere with such species as Na and K (Potter and Morgan, 1985, 1986). Even though our understanding of Mercury's bulk composition is limited, some constraints on models of planetary formation and evolution are possible. If Mercury condensed from the inner refractory portion of a hot early nebula, it should be strongly deficient in volatiles and FeO (e.g., Lewis 1972, 1974). The possibility that Mercury's semimajor axis experienced large excursion during growth of the inner planets (Wetherill 1994) is permissive of Mercury having greater fractions of volatiles and FeO.

Mariner 10 images showed a heavily cratered surface grossly similar to that of the Earth's Moon (Murray et al. 1975; Spudis and Guest 1988). One of the more distinctive morphologic features discovered by Mariner 10 is a class of tectonic features known as lobate scarps, interpreted to reflect large-scale contractional deformation of Mercury's crust. Lobate scarps are thought to be the surface expression of thrust faults formed as the planet's interior cooled and contracted, possibly during a period in which tidal despinning was also occurring (Strom et al. 1975; Cordell and Strom 1977; Melosh and Dzurisin 1978; Pechmann and Melosh 1979; Melosh and McKinnon 1988; Watters et al. 2004). Another distinguishing feature of Mercury is the smooth plains. Smooth plains are comparable in morphology to lunar mare deposits, but they lack the distinctive low albedo of their lunar counterparts, because of the very low FeO content (Trask and Guest 1975; Strom 1977; Kiefer and Murray 1987; Rava and Hapke 1987; Spudis and Guest 1988). Whether the smooth plains are volcanic or impact deposits is still debated (Wilhelms 1976; Kiefer and Murray 1987; Robinson and Lucey 1997).

Earth-based radar images of Mercury rival those obtained by Mariner 10 (Harmon et al. 2001). More importantly, radar led to the discovery of an anomalous class of materials inside permanently shadowed crater interiors in both polar regions. These materials exhibit high

radar reflectivity and a circular polarity inversion consistent with a volume scatterer (Slade et al. 1992; Harmon and Slade 1992). Water ice remains the leading candidate material to explain the shadowed deposits, but many unanswered issues remain and final resolution must await orbital observations (Harmon et al. 2001).

The MErcury Surface, Space ENvironment, GEochmistry, and Ranging (MESSENGER) spacecraft was conceived, designed, and built to address six fundamental science questions regarding the formation and evolution of Mercury (Solomon et al. 2001). (1) What planetary formational processes led to the planet's high metal-to-silicate ratio? (2) What is Mercury's geological history? (3) What are the nature and origin of Mercury's magnetic field? (4) What are the structure and state of Mercury's core? (5) What are the radar-reflective materials at Mercury's poles? (6) What are the important volatile species and their sources and sinks on and near Mercury?

The process of selecting the scientific instrumentation to investigate these diverse questions balanced the available mission resources for mass, power, mechanical accommodation, schedule, and money. For MESSENGER, the mass and mechanical accommodation issues were very significant design constraints. The payload mass was limited because of the large amount of propellant needed for orbital insertion. The mechanical accommodation was difficult because of the unique thermal constraints faced in the mission. Taking into account all these factors, MESSENGER carries seven miniaturized instruments (Gold et al. 2003): the Mercury Dual Imaging System (MDIS), Gamma-Ray and Neutron Spectrometer (GRNS), X-Ray Spectrometer (XRS), Mercury Laser Altimeter (MLA), Magnetometer (MAG), Mercury Atmospheric and Surface Composition Spectrometer (MASCS), and Energetic Particle and Plasma Spectrometer (EPPS). Additionally, a radio science investigation will address key measurements such as Mercury's physical libration and gravity field.

The MESSENGER spacecraft was launched from Cape Canaveral on August 3, 2004, in a spectacular nighttime launch. On August 1, 2005, the spacecraft successfully completed an Earth gravity assist to slow the spacecraft and redirect it toward the inner solar system. En route to its primary mission at Mercury, MESSENGER experiences two Venus flybys and three Mercury flybys. The first Venus flyby occurred on October 24, 2006, and the second occurred on June 5, 2007. The three Mercury flybys will take place on January 14, 2008, October 6, 2008, and September 29, 2009, during which regions unexplored by Mariner 10 will be imaged by MDIS. Mercury orbit insertion will occur on March 18, 2011, and the spacecraft will begin the orbital phase of its mission, which is one Earth year in duration. The orbital mission is slightly longer than two Mercury solar days.

2 MDIS Measurement Objectives and Design Implementation

MDIS consists of two cameras, a monochrome narrow-angle camera (NAC) and a multispectral wide-angle camera (WAC), coaligned on a common pivot platform. The passively cooled detectors in each camera are thermally tied to its complex thermal system. This arrangement allows the detectors to be maintained within their operating temperature, even during the hottest portion of the orbit at Mercury. The pivot platform provides an added degree of freedom to point the dual cameras with minimal impact on the spacecraft. The full design details of the instrument are given in Sect. 3. Specifications of the two cameras, given in Table 1, are tailored to the orbit and imaging requirements of the MESSENGER mission.

MESSENGER will be placed in a highly eccentric orbit with a periapsis altitude of 200 km, a periapsis latitude of ∼60°N, and an apoapsis altitude of 15,200 km. The orbit has a 12-hour period, is inclined 80° to the planet's equatorial plane, and is not Sun synchronous. During one Mercury solar day (noon to noon), the planet completes three full rotations

Table 1 MDIS camera specifications

	Narrow angle	Wide angle
Field of view	1.5° × 1.5°	10.5° × 10.5°
Pivot range	−40° to +50°	
(observational)	(Sunward) (Planetward)	
Exposure time	1 ms to ∼10 s	
Frame transfer time	3.84 ms	
Image readout time[a]	1 s	
Spectral filters	1	12 positions
Spectral range	700–800 nm	395–1,040 nm
Focal length	550 mm	78 mm
Collecting area	462 mm^2	48 mm^2
Detector-TH7888A	CCD 1024 × 1024, 14-μm pixels	
IFOV	25 μrad	179 μrad
Pixel FOV	5.1 m at 200-km altitude	35.8 m at 200-km altitude
Quantization	12 bits per pixel	
Hardware compression	Lossless, multi-resolution lossy, 12-to-n bits	
	MDIS Assembly	**MDIS DPU-A or -B**
Mass	7.8 kg	1.5 kg
Power[b]	7.6 W	12.3 W
Footprint	398 × 270 × 318 mm	157 × 117 × 104 mm
Data rate	16 Mbps (to DPU)	3 Mbps (to SSR)

[a]Transfer to DPU

[b]Nominal power configuration (DISE + NAC or WAC; DPU + MDIS motor + resolvers)

relative to the spacecraft orbital plane. At times the ground track is near the terminator (the "dawn–dusk orbit"); 22 days later it passes over the subsolar point (the "noon–midnight" orbit).

The two primary imaging objectives during the flybys are (1) acquisition of near-global coverage at ∼500 m/pixel, and (2) multispectral mapping at ∼2 km/pixel. During the flyby departures, large portions of the planet will be viewed at uniform low phase angles.

From orbit, gaps in color imaging acquired during the flybys will be filled with images taken at a wide variety of lighting geometries. Total flyby coverage will exclude only the polar regions and two narrow longitudinal bands. The flybys each have one of two basic geometries (Table 2), and similar observation strategies will be used for each (Table 3). During the flyby phase, 85% of the planet will be imaged in monochrome at a resolution averaging ∼500 m/pixel, and greater than 60% will be imaged in color at about 2 km/pixel. Half of the planet will be covered in color at ∼1 km/pixel. High-resolution NAC swaths will contain monochrome images at better than 125 m/pixel.

During the orbital phase of the mission the MDIS observation strategy will shift to acquisition of four key data sets: (1) a nadir-looking monochrome (750-nm) global photomosaic at moderate solar incidence angles (55°–75°) and 250 m/pixel or better sampling; (2) a 25°-off-nadir mosaic to complement the nadir-looking mosaic for stereo; (3) completion of the multispectral mapping begun during the flybys; and (4) high-resolution (20–50 m/pixel) image strips across features representative of major geologic units and structures.

Table 2 Key parameters describing the three MESSENGER Mercury flybys

Date	CA altitude	CA lon	Inbound lon	Outbound lon	Illuminated lon	Key features
1/14/08	200	40°	308°	132°	276° to 96°	Caloris, EUH
10/06/08	200	230°	136°	324°	94° to 274°	Kuiper, WUH, MG
09/29/09	200	212°	108°	315°	90° to 270°	Kuiper, WUH, MG

All closest approach (CA) latitudes are near-equatorial, and range is listed in kilometers; closest approach occurs on the nightside of the planet for all three flybys. The columns "Inbound lon" and "Outbound lon" indicate subspacecraft longitudes at 20,000 km range during the inbound and outbound legs of the respective flyby. Comments indicate the portion of Mercury imaged during each flyby (Caloris = Caloris basin, EUH = eastern half of hemisphere unseen by Mariner 10, Kuiper = Kuiper crater, WUH = western half of hemisphere unseen by Mariner 10, MG = Mariner 10 gore). All longitudes are positive east. During the three Mariner 10 flybys Mercury was illuminated from 350°E to 170°E

Both the nadir and off-nadir image mosaics will be acquired with the NAC for southern latitudes when altitude is high and with the WAC at lower altitudes over the northern hemisphere. This two-camera strategy results in near-uniform global coverage with an average spatial resolution of 140 m/pixel. The off-nadir mosaic will be acquired under nearly identical lighting geometries to the nadir map to facilitate automated stereo matching. The global digital elevation model derived from stereo imaging will have a spatial resolution of 1–4 km horizontally and 100–500 m vertically, depending on latitude. MDIS stereo imaging will be the main source of surface elevation mapping for the southern hemisphere, as MLA's 1,000-km slant range (Cavanaugh et al. 2007) largely limits laser altimetry to the northern hemisphere. Filling gaps in color coverage is a relatively simple matter of pointing at and imaging a particular location during times of favorable lighting, except at low altitudes over high northern latitudes. At northern mid-latitudes, low spacecraft altitudes will limit viewing opportunities and probably require gap-filling images to be taken in long strips. At the time of writing, the strategy for gap-filling of flyby color mapping is still being defined. High-resolution NAC imaging is effectively limited by ground motion smear to about 20 m/pixel in the along-track direction; accurate postprocessing correction for electronics artifacts (Sect. 4.3) requires exposure times of ~7 ms or longer, equivalent to <20 m of along-track motion smear.

2.1 Science Traceability

The flowdown of requirements from science objectives to instrument design and data acquisition strategy are summarized in Table 4, which also compares the instrument requirements to as-built performance. Key constraints on the design of the MDIS investigation are the spacecraft's thermal environment, its highly eccentric orbit, the vertical accuracy required of stereo imaging, the low downlink rates, and the need to support optical navigation (opnav) prior to each Mercury flyby.

At Mercury, the intensity of the solar radiation varies from about 7 to 10 times the total irradiance falling on the Earth. A large sunshade protects MESSENGER from this intense solar illumination but constrains the spacecraft pointing ability (Leary et al. 2007). To support optical navigation during the flybys, Mercury will be imaged against the star background; MDIS thus had to be designed to image at phase angles as high as 140°. At the other extreme, flyby science observations require imaging at phase angles of 32°. To compensate for the restricted pointing capability of the spacecraft imposed by the sunshade,

Table 3 Mercury flyby imaging plan

Description	km/pix	Filters	Pixel binning	Approx. hardware comp. ratio	Bits/pixel	Wavelet comp. ratio	Cum. images	Cum. Gib, uncompressed	Cum. Gib, hardware compressed	Cum. Gib, compressed[b]
Approach opnavs		1	–	1.3	12	1	6	0.070	0.054	0.054
Approach movie		1	–	2.5	8	12	36	0.305	0.148	0.062
Approach color image	5	11	–	1.3	12	2	47	0.434	0.247	0.111
Approach mosaic	0.5	1	–	2.5	8	8	87	0.746	0.372	0.127
High-resolution mosaic 1	0.06	1	–	2.5	8	8	147	1.215	0.559	0.151
High-resolution color mosaic	1	11	–	1.3	12	2	246	2.375	1.452	0.597
Color photometry sequence[a]	–	11	2 × 2	1.3	12	2	345	2.665	1.675	0.708
High-resolution mosaic 2	0.2	1	–	2.5	8	8	499	3.868	2.156	0.768
Departure color mosaic	2	11	–	1.3	12	2	598	5.028	3.049	1.215
1st departure mosaic	0.4	1	–	2.5	8	6	697	5.802	3.358	1.266
2nd departure mosaic	0.5	1	–	2.5	8	6	796	6.575	3.667	1.318
Departure color image	5	11	–	1.3	12	2	807	6.704	3.767	1.367
3rd (stereo) mosaic	0.7	1	–	2.5	8	6	842	6.978	3.876	1.386
4th (stereo) mosaic	0.8	1	–	2.5	8	6	877	7.251	3.985	1.404
Departure opnavs		1	–	1.3	12	1	883	7.321	4.039	1.458
Departure movie		1	–	2.5	8	12	913	7.556	4.133	1.466

[a] Same spot at phase angles 50°–130° in 10° increments

[b] Total space available on solid-state recorder is 8 Gib

Table 4a Derived MDIS requirements and as-built performance for field-of-view, pointing, and spatial resolution

Measurement objective	Measurement requirement	Instrument / spacecraft requirement	As-built performance	Method of verification
Flyby near global monochrome map at 500 m/pixel	Image Mercury outbound on all three flybys; maximize area imaged in orbit at near-0° emission angle	Point from nadir to >40° antisunward, >50° sunward maintaining unobstructed FOV	Unobstructed FOV to 64° antisunward, 52° sunward using pivot and spacecraft slew	By design
Provide optical navigation support for Mercury flybys	Opnavs earlier than encounter (E) – 2.5 days at flybys	Availability of imaging at 31°–142° phase angles at center of FOV, from combination of pivoting and spacecraft slewing, provides: • NAC imaging at E-6.0 days @ flyby 1, E-3.7 days @ flyby 2, E-7.2 days @ flyby 3 • WAC imaging at E-7.0 days @ flyby 1, E-4.7 days @ flyby 2, E-8.0 days @ flyby 3		Trajectory analysis
Near-nadir global monochrome map at 250 m/pixel	FOV wide enough for cross-track continuity, average dayside altitude	>9.3° WAC FOV for baseline orbit (>160 μrad pixel)	10.5° WAC FOV (179 μrad pixel)	Geometric calibration
	Cross-track continuity maintained at lowest altitudes using pivoting of FOV	1.1°/s pivot rate to stagger WAC FOVs to produce 15°-wide composite image strips	1.1°/s	Pivot testing
	Acquire image strips without cross-track gores or excessive cross-track overlap	Acquire rectangular subframes at up to 1 Hz to manage downlink volume	Arbitrarily defined rectangular subframes available at 1 Hz	Spacecraft functional testing
	<250 m/pixel sampling, globally, with low emission angle	WAC and NAC IFOVs provide <250 m/pixel average sampling for nominal orbit	140 m/pixel average sampling of surface at optimal lighting	Coverage simulations
		WAC and NAC PSF support sampling at <2× average requirement	Projected FWHM of NAC PSF ~700 m in southern high latitudes; onground PSF measurement to be used for image restoration	Radiometric calibration and analytical modeling
		Main processor and downlink volume allow average spatial resolution of binned pixels <250 m/pixel with moderate compression	25.9 Gb MDIS downlink (d/l) allocation allows d/l of 140 m/pixel using 8:1 compression; MP loading requires on-chip 2 × 2 binning for portion of data, degrading resolution by up to 2×	Coverage and spacecraft performance simulations
Point with sufficient accuracy to allow mosaicking with <10% image overlap	<0.15° pointing accuracy for spacecraft to maintain <10% NAC image overlap		0.02° pointing accuracy for spacecraft; 0.03° including 1-σ uncertainty	Simulation based on uncertainties from component tests
		<0.15° step for MDIS pivot mechanism	0.01° step for MDIS pivot mechanism	By design

Underlined items incur additional data processing or revisions to the data acquisition strategy to meet requirements, as indicated

Table 4b Derived MDIS requirements and as-built performance for spacecraft slewing, stability, memory, and downlink

Measurement objective	Measurement requirement	Instrument / spacecraft requirement	As-built performance	Method of verification
Near-nadir global monochrome map at 250 m/pixel	Roll spacecraft sufficiently rapidly to track nadir at the minimum 200-km orbital altitude	1.35 mrad/s	1.7 mrad/s	Spacecraft functional testing
	Ability to track nadir from any orbit	Pivot and spacecraft roll coordinate to point MDIS boresight to local nadir	Spacecraft roll to keep nadir in pivot plane, spacecraft supplies MDIS with pivot attitude	Spacecraft functional testing
	Image smear by spacecraft jitter small compared with image smear due to downtrack motion	Jitter <25 μrad in 100 ms (<1 NAC pixel, typical exposure)	<1 μrad in 100 ms	Analytical modeling
	Hold orbital data in recorder	Hold volume of DPU-compressed images	Baseline mission requires storing <2.3 Gb; usable recorder vol. 6.2 Gb	Data coverage simulation
		Hold number of MP-compressed images	Baseline mission requires storing < 2500 compressed images; >8000 available	
Flyby near global monochrome map at 500 m/pixel	Hold flyby data in recorder	Hold volume of DPU-compressed images	Nominal flyby scenario 5.4 Gb; usable recorder volume of 6.2 Gb	
		Hold number of MP-compressed images	Nominal flyby scenario 913 images; uncompressed image directory holds 2046	
Multispectral map at 2 km/pixel	Downlink compressed flyby data to ground	>2.3 Gb downlink allocation to MDIS following each Mercury flyby (core data)	Current downlink >6 Gb after each flyby	
Targeted high-resolution imaging	Transfer data to SSR at rate greater than image acquisition	Highest image acquisition rate is 1 Hz (3.2 Mb/s for image binned 2 × 2 on-chip)	3.2 Mb/s link speed	Instrument and spacecraft functional testing

Table 4b (*Continued*)

Measurement objective	Measurement requirement	Instrument / spacecraft requirement	As-built performance	Method of verification
Near-nadir global monochrome map at 250 m/pixel	Downlink compressed orbital data to ground	5.6 Gb/yr minimum allocation to MDIS during orbital mission as per Concept Study	~25.9 Gb/yr allows improvement in average base map sampling from 250 to 140 m/pixel, color to 1 km/pixel	Data coverage simulation
Global multispectral map at 2 km/pixel		Pixels 2 × 2 or 4 × 4 without overflow at 7 ms exposure	2 × 2 binning on-chip sums signal, does not overflow at min. solar distance and phase angle; 2 × 2, 4 × 4 binning in MP averages signal	Radiometric calibration; instrument and spacecraft functional testing
		Lossy compression, >6 : 1 with artifacts near noise	Wavelet compression in MP; artifacts near noise at 8 : 1	Simulation using NEAR 16-bit images
Provide optical navigation support for Mercury flybys	Promptly downlink star-planet-star triplets	Return jailbars from Mercury images	Jailbars at regular period in image	Instrument and spacecraft functional testing
		Return ≥ 3 subframes of stars per image (to 140 × 140 pixels for NA, allowing for 0.1° pointing control)	Up to 5 subframes per image, sized up to full image	
	Locate Mercury against star background	Detect ≥3 stars in FOV at max exposures	Met for WAC at longest exposure; marginal in NAC	Radiometric calibration and analytical modeling
	Take unsmeared star frames	Jitter <25 μrad in 10 s (<1 NAC pixel)	<25 μrad in 10 s >99% of time	Analytical modeling

Table 4c MDIS requirements and as-built performance for multispectral imaging

Measurement objective	Measurement requirement	Instrument / spacecraft requirement	As-built performance	Method of verification
Multispectral map at 2 km/pixel	Move filter wheel to allow 11-color imaging strip from lowest altitude over day side	Worst-case FOV motion by 1 footprint in 15.5 s requires 14 s per cycle (allowing 10% overlap), 1 Hz imaging in 11 filters + 3 s for reposition	1 Hz imaging supported for exposures <500 ms; 2 s for reposition; 13 s total	Instrument functional testing
	<2 km/pixel spatial sampling	<2 km/pixel during flyby, from orbit to fill gaps in flyby coverage	2 km/pixel resolution at 4.5 planet radii, or within 10,000 km during orbit	Geometric calibration, trajectory analysis
	Spectral filters for mapping of olivine, pyroxene, glass, opaques	7 WAC spectral filters, violet to 1050 nm	11 WAC spectral filters to measure key features, plus clear filter	Radiometric calibration
	Map abundance variations in opaque and mafic minerals: 750/415 nm, 750/650 nm, and 750/950 nm ratios measured to 1% precision	MTF >0.62 at 1 cycle/8 pixels to preserve variations above noise level	MTF ~0.75 1 cycle/8 pixels for typical filter	Analysis and radiometric calibration
		Model dark current to ≪system noise (≪1 DN)	Dark current model residuals at read-noise level at <5°C, consistent with model accuracy ≪noise	Radiometric calibration
		Response linearity to 1%	<u>Departures of ≤2% at low DN levels correctable during ground processing</u>	Radiometric calibration
		Characterize responsivity to 5% absolute, 2% relative between filters	<u>On-ground calibration at −34, −30, +24°C insufficient for interpolation to higher (−10°C) CCD operating temperatures; need flight measurement of Mercury-illuminated calibration target</u>	Radiometric calibration
		Model flat field to 0.1% precision (0.4 of noise at full well)	<u>Composite of 100 images provides 0.04% precision; flight measurements needed due to mobility of dust donuts</u>	Radiometric calibration
	Protect optics from contamination that increases scattered light	Stow MDIS in position with optics protected from contaminants during burns, thermal spikes on sunshade	Front optic stowable in instrument base	Instrument functional test

Underlined items incur additional data processing or revisions to the data acquisition strategy to meet requirements, as indicated

Table 4d MDIS requirements and as-built performance for high-resolution and stereo imaging

Measurement objective	Measurement requirement	Instrument / spacecraft requirement	As-built performance	Method of verification
Targeted high-resolution imaging	Acquire continuous strip of images with NAC from minimum orbital altitude	At minimum altitude of 200 km, NA footprint moves 1 FOV in 1.4 s. Requires 1 Hz imaging.	1 Hz imaging supported using 2 × 2 pixel binning or quarter frames	Instrument functional testing
	Acquire <20 m/pixel NAC frames from lowest altitude expected over day side (280 km) with <20 m smear due to spacecraft motion	NAC IFOV <71 μrad	NAC IFOV 20 μrad	Geometric and radiometric calibration
		Minimize time for CCD frame transfer (minimum useful exposure time ~2× frame transfer time)	3.7 ms frame transfer yields ~7 ms exposure. At 3.3 km/s, 18 m linear smear. Pixel footprint 12 m/pixel after 2 × 2 binning required for 1 Hz imaging	
	No saturation at minimum exposure time	No saturation in 7 ms NAC image at 33° phase, minimum solar distance, 2 × 2 pixel binning	Worst-case saturation time 16 ms	Radiometric calibration and photometric model
Off-nadir imaging to complement nadir geometry for stereo	Image areas both at nadir and off-nadir with similar lighting	Consistent observation strategy meeting other spacecraft constraints	N hemisphere nadir first solar day, off-nadir second solar day; S hemisphere nadir and off-nadir on adjacent orbits first solar day. Meets spacecraft constraints as given in Table 4b.	Coverage simulation
	Ability to take off-nadir images an arbitrary orbit	Pivot and spacecraft roll usable together to point MDIS boresight offset along-track from local nadir	Roll spacecraft to keep nadir offset from pivot plane, supply MDIS with pivot attitude	Spacecraft functional testing
	Stereo vertical accuracy goal is ±2 km from 6000-km altitude (root sum squared pointing knowledge 240 μrad)	180 μrad boresight knowledge with in-flight calibrations (1.4× worse than NEAR with in-flight pointing cals. using star images; allows for scan plane vs. fixed pointing)	Ability to extract multiple subframes from starfield images for pointing calibrations within downlink; 200 μrad expected pointing knowledge	Instrument and spacecraft functional testing; flight calibration required for pointing knowledge

Table 4d (*Continued*)

Measurement objective	Measurement requirement	Instrument / spacecraft requirement	As-built performance	Method of verification
		150 μrad knowledge of pivot position	85 μrad	Pivot position calibration
		Knowledge of center of MDIS exposure to ±10 ms	<1 ms uncertainty	Analysis of image acquisition timing using external strobe and Universal Time clock
		Acquire images from orbits with minimal thermal disturbances to instrument deck	Nadir and off-nadir coverage planned from near-terminator orbit with lesser thermal variation	By design

Fig. 1 Photograph of the Mercury Dual Imaging System (MDIS) instrument just prior to integration with the spacecraft (S/C). Redundant Data Processing Units (DPUs, not shown) connect to MDIS through the DPU Interface Switching Electronics (DISE). Red-tag covers were used to protect apertures during handling and were removed before flight. Some thermal blankets are not shown to reveal structure
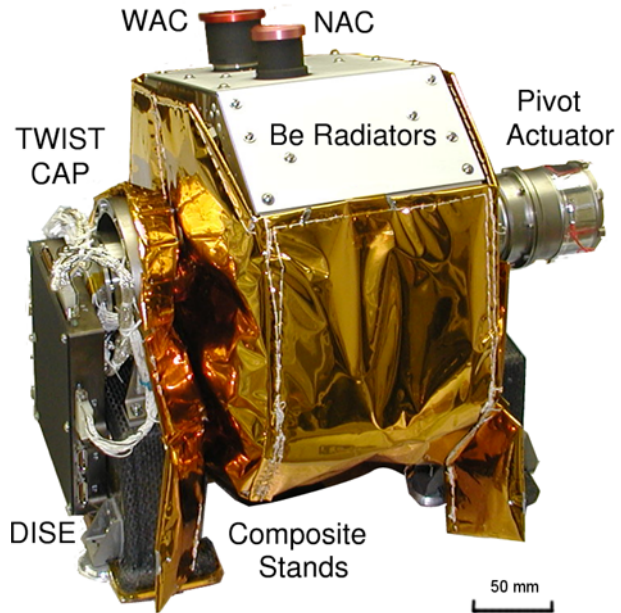
the dual cameras of MDIS are able to pivot about a common axis (Fig. 1). The nominal operational scan range of the platform is 40° in the sunward direction and 50° anti-sunward. With spacecraft slewing, phase angle coverage of 26°–142° is possible in both cameras at the center of each field of view (FOV). Imaging is available in the WAC 5.3° farther in each direction because of the wide FOV; in the NAC imaging is possible 0.75° farther. During launch and key orbital maneuvers, the camera can be placed in a stowed position, providing contamination protection for the optics (Fig. 2).

The thermal environment poses challenges for MDIS performance, because the cameras must view the hot surface (>400°C) on some orbits for ∼120 minutes. Although this thermal environment presents issues for all parts of the instrument, the most stressing case is maintaining nominal temperature of the charge-coupled device (CCD). Wide swings in detector temperature potentially degrade signal-to-noise ratio (SNR), calibration accuracy, and the value of the acquired images.

The thermal environment also poses a challenge for stereo imaging. Stereo provides measurement of both relief (the elevation difference between stereo resolution cells, about 5×5 to 7×7 pixels in size) and elevation relative to mean planetary radius. In the southern hemisphere, beyond the range of the MLA, the primary knowledge of elevation to mean planetary radius will be from photogrammetric analysis of MDIS images (plus occultations of radio signals from the spacecraft to Earth). Accuracy in an elevation determination from stereo is proportional to $h\sigma/\tan(e)$, where h is the orbital altitude, σ is the uncertainty in pointing knowledge between image pairs, and e is the emission angle of the off-nadir image. The goal for elevation accuracy is ± 2 km. Assuming that accuracy can be improved by a factor of two using photogrammetric techniques at the corners of four stereo pairs, the required accuracy is ± 4 km. For a 6,000-km orbital altitude, which is appropriate to southern high latitudes, and a 25° emission angle of the off-nadir images, the required pointing knowledge is ± 240 µrad. This requirement is budgeted between uncertainty in the knowledge of image acquisition time (which translates into downtrack position error), uncertainty in pivot
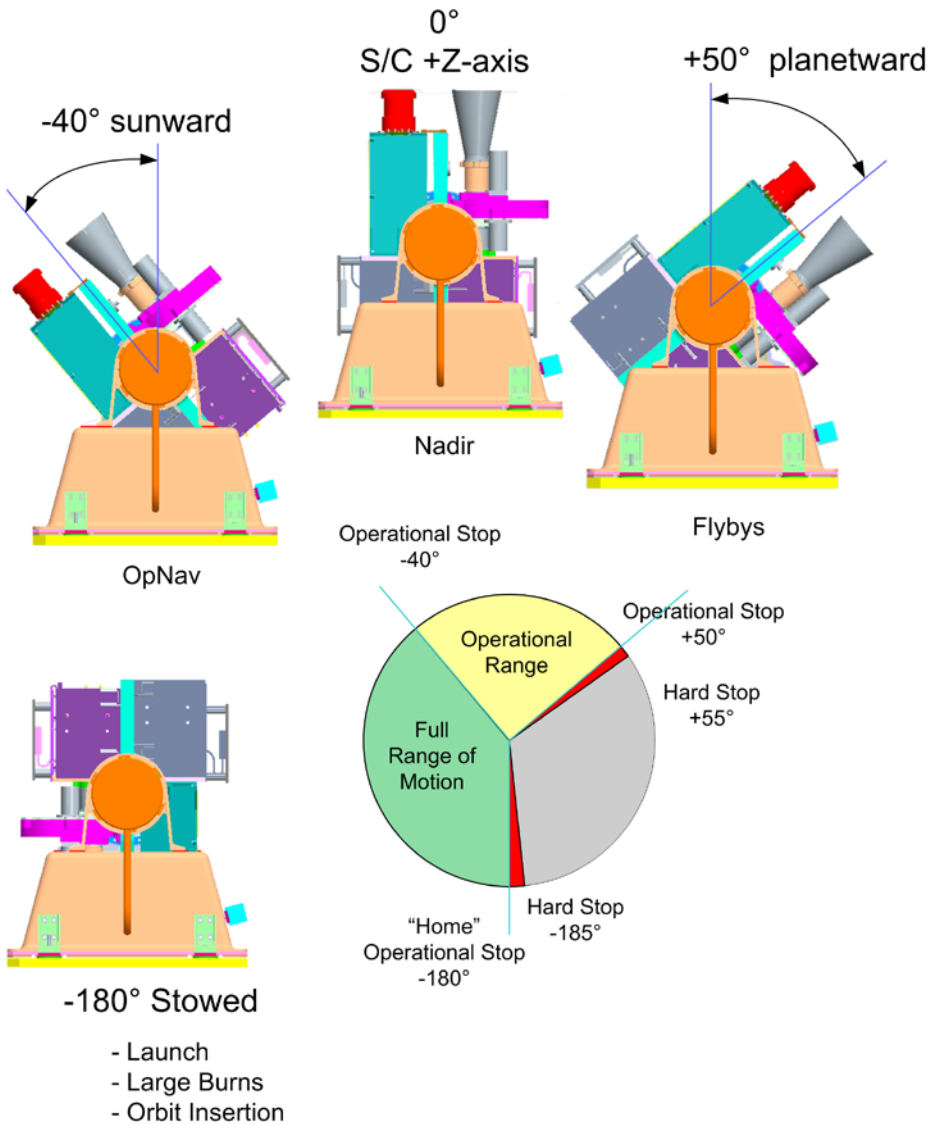
Fig. 2 Range of motion of the MDIS pivot platform. Operational range is −40° sunward to +50° antisunward (planetward). When stowed, the sensitive first optic of each telescope is protected

position within its plane of motion, and variation in orientation of the pivot plane relative to thermal distortion of the spacecraft. The largest term is due to variation in pivot plane orientation relative to the star camera (Table 4d). On the Near Earth Asteroid Rendezvous (NEAR) mission, orientation of its fixed-pointed camera was modeled to ±130 µrad as a function of temperature of the spacecraft structure, using star-field images to calibrate pointing. Allowing for the fact that MDIS moves in a plane, and that the plane may shift in orientation with temperature, the budget is increased by $\sqrt{2}$ to 180 µrad, leaving 140 µrad for uncertainty in position within the pivot plane and along-track errors. To facilitate pointing

calibrations with MESSENGER's limited downlink, the spacecraft main processor provides a subframing capability that allows up to five subframes per image encompassing stars.

The eccentric orbit results in challenges associated with strongly variable spacecraft range and velocity. Spacecraft altitude above the surface ranges between 300 and 15,000 km on the dayside. This variation, combined with the requirement for imaging at near-nadir geometries, drove the selection of camera optics. The WAC's 10.5° FOV is sufficient that overlap occurs between nadir-pointed image strips taken on adjacent orbits, even at northern mid-latitudes where low altitudes occur. The NAC's 1.5° FOV is sufficiently narrow that 375 m/pixel sampling is attained at 15,000 km altitude. Low emission-angle geometries are available each solar day for all parts of the planet from altitudes of less than 10,000 km, providing 250 m/pixel sampling or better. The low altitude at periapsis also drives the speed of image acquisition. For multispectral imaging, acquisition of 11-color data from the minimum dayside altitude (∼300 km) requires the WAC to take images at 1-Hz cadence. Along-track continuity of high-resolution imaging also requires 1-Hz imaging. In neither case is full resolution of either the WAC or NAC required; 2×2 pixel binning on-chip meets the spatial sampling requirements both for WAC color and for NAC high-resolution imaging from low altitude. Meeting low-altitude imaging requirements thus drives the speed of the WAC filter wheel (1-Hz imaging in adjacent filters) and link speed from either camera to the recorder (12-bit, 512×512 frames at 1 Hz) as described in Tables 4c and 4d.

The MESSENGER mission requires compression to meet its science objectives within the available downlink. Figure 3 summarizes the compression options available to MDIS at the instrument level using the spacecraft main processor (MP). At the focal plane, 2×2 binning is available on-chip to reduce the $1,024 \times 1,024$ images to 512×512 format, 12-bit data number (DN) levels can be converted to 8 bits, and data can be compressed losslessly. The strategy for image compression is to acquire all monochrome data in 8-bit mode, and color data in 12-bit mode, and to compress all data losslessly to conserve recorder space. After data are written to the recorder, they can be uncompressed and recompressed by the MP more aggressively using any of several options: additional pixel-binning, subframing, and lossy compression using an integer wavelet transform. The strategy for MP compression is that all data except flyby color imaging will be wavelet compressed, typically 8:1 for monochrome data and to a lower ratio ($\leq 4 : 1$) for orbital color data. Color imaging but not monochrome imaging may be further pixel-binned. For the special case of optical navigation images, there is a "jailbar" option that saves selected lines of an image at a fixed interval for optical navigation images of Mercury during flyby approaches.

Compression performance was extensively modeled prior to launch. The 12-to-8 bit lookup tables have been designed to retain preferentially information at low, medium, or high 12-bit DN values, for a nominal detector bias or for one that has decreased with time (Fig. 4). Compression ratios to be used for flight have been based on a study of the magnitude and spatial coherence of compression artifacts using NEAR images (Fig. 5). For expected loading of the main processor, simulations have shown that the MP can compress the equivalent of 82 full $1,024 \times 1,024$ images per day (or 330 512×512 images per day). The actual number of images has also been simulated, based on orbital trajectory simulations and the imaging plan described in the following. The MP image compression capabilities are consistent with the mission-average number of images per day. However, on days when lighting is favorable for global mapping, a peak of ∼260 images per day may be expected, requiring on-chip binning of most of the data on peak days. The full implications for average imaging resolution are still being assessed.

The final set of requirements involves the responsivity required for mapping Mercury and for optical navigation. For WAC spectral filters, passband widths were selected to provide
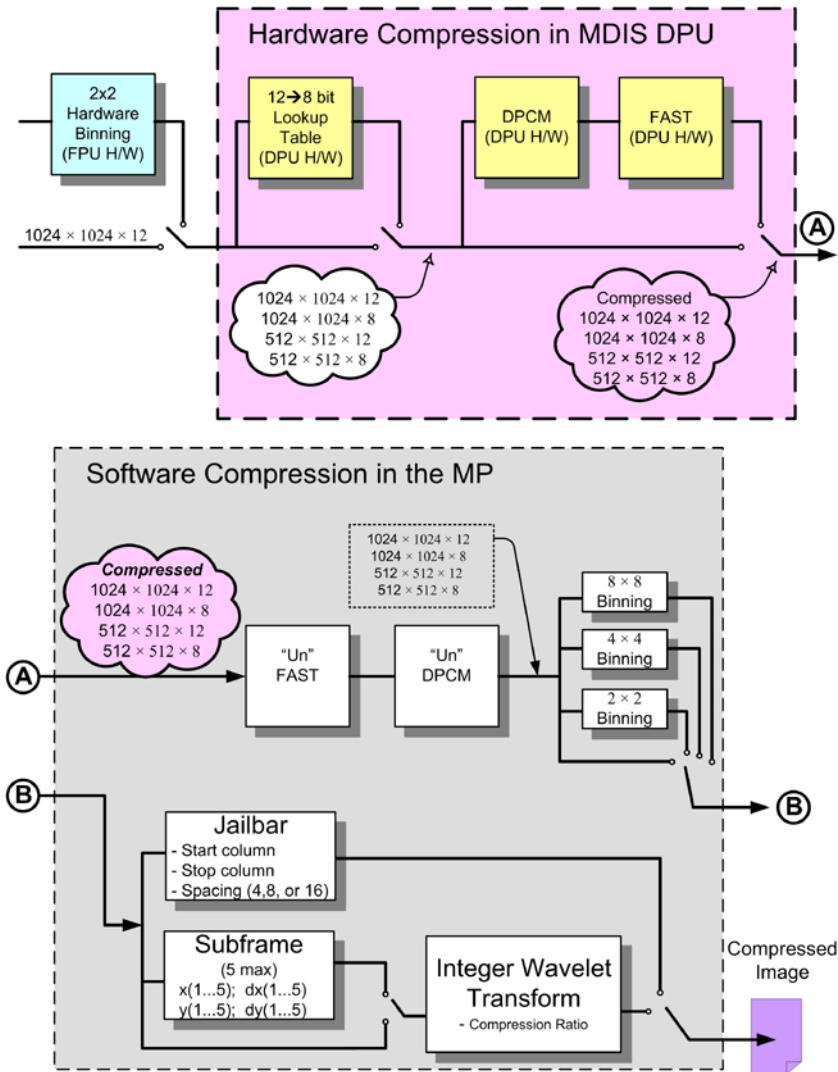
Fig. 3 Hardware (H/W) compression options available for MDIS images in the instrument DPU and software compression options available in the spacecraft main processor (MP). Note: (1) If 2×2 binned mode is selected as the camera mode, further binning options are not available in the MP. (2) A compression ratio of 0 results in a losslessly transformed image (the resulting image size actually grows due to transforming from 12- to 16-bit representations of each pixel)

required SNR in exposure times sufficiently short to prevent linear smear by along-track motion, yet sufficiently long (>7 ms) to avoid excessive artifacts from removal of frame transfer smear during ground processing. SNR is not an issue, as sufficient light is available for SNRs >200, but saturation is a concern at low phase angles. At the same time, both cameras must be sufficiently sensitive to provide star images for optical navigation and display adequate rejection of stray light. A sequence of long and short exposures will be used for optical navigation. A short exposure in which the planet is not saturated will permit determi-
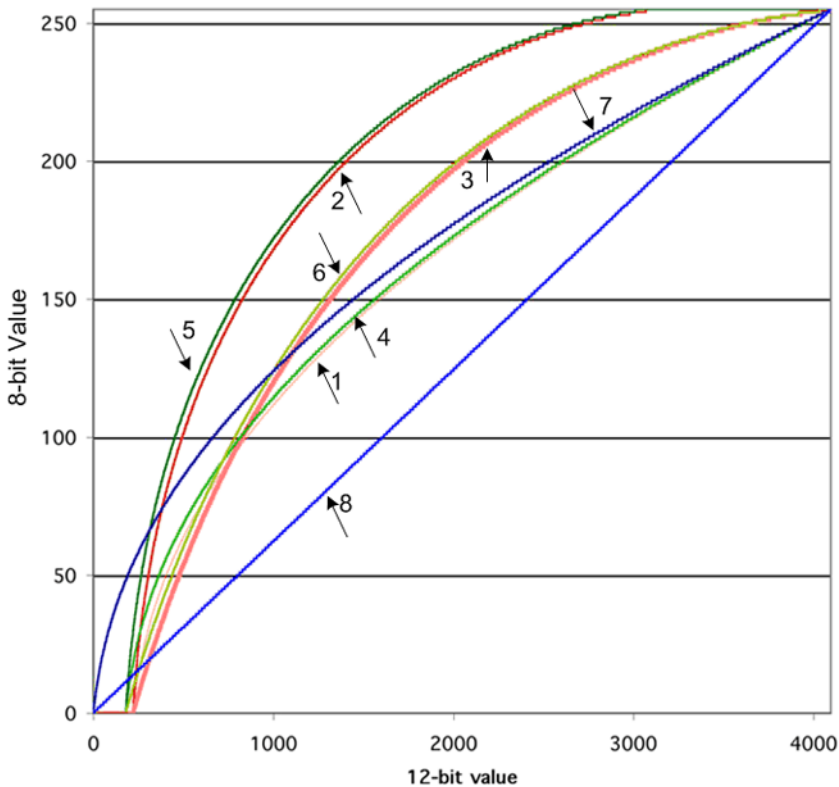
Fig. 4 Mapping of 12 bits to 8 bits will be accomplished using onboard look-up tables. The tables are designed to preserve preferentially information at different DN ranges, and they can accommodate a nominal detector dark level as well as one that has changed with time. (*1*) Low noise, high bias, SNR proportional. Usage: Typical imaging with varied brightness. (*2*) Low noise, high bias, DN-weighted, SNR proportional. Usage: Faint-object imaging. (*3*) High noise, high bias, DN-weighted, SNR proportional. Usage: Black and White (B/W), low brightnesses. (*4*) Low noise, medium bias, SNR proportional. (*5*) Low noise, medium bias, DN-weighted, SNR proportional. Usage: Faint objects. (*6*) High noise, medium bias, DN-weighted, SNR proportional. Usage: B/W, mostly low brightness. (*7*) Zero-bias, SNR proportional. Usage: Typical imaging, varied brightness. (*8*) Linear. Usage: High-brightness mapping, preserves high-DN information

nation of Mercury's location within the image using centroiding techniques. When imaging a saturated Mercury against a star background (as will be the case for long exposures), at least three stars must be visible per image at $\geq 7\times$ noise. For the WAC this requirement was easily met (Table 5a) using a clear filter. For the NAC, its single filter was designed with a first priority of not saturating on bright crater ejecta while imaging Mercury at low phase angles using pixel binning. As a consequence, sensitivity to stars is limited. Detection of three stars per frame for a typical patch of sky is only marginal (Table 5b).

2.2 Common Payload Design

In order to satisfy the science requirements and the design constraints of the MESSENGER mission, many aspects of the science payload were implemented in common. The need to share resources among the instruments played a significant part in the design implementation. The complexity of the MDIS instrument required a separate electronics box, shown in
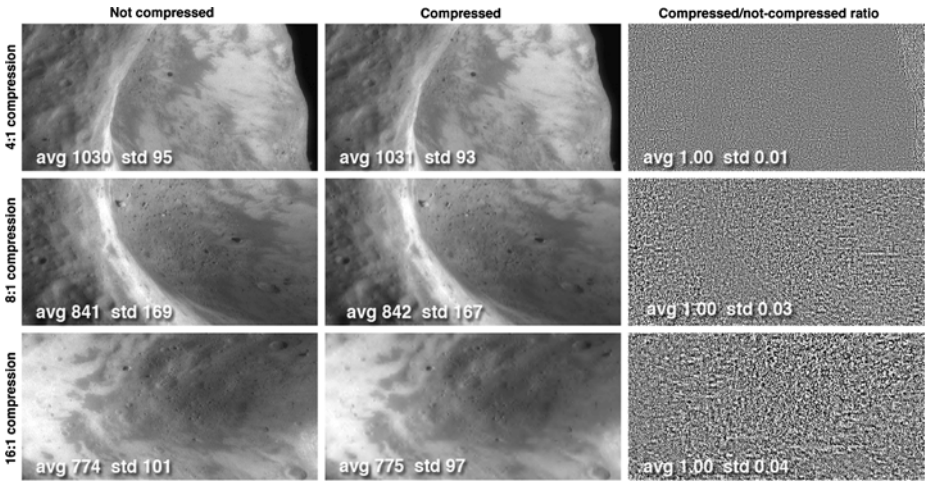
Fig. 5 Effects of compression to different ratios using the MESSENGER integer wavelet transform. Well-exposed 12-bit (DN peaks near 3,000 out of 4,095) NEAR MSI images simulate well the properties of MDIS raw data. The *left column* shows the image prior to compression, and the *middle column* after compression and decompression. The *right column* shows the ratio of the decompressed image to the original; the standard deviation of the ratio is a measure of the artifacts for typical illumination

Table 5a WAC sensitivity to stars

M_v	10 s exposure, no pixel sum, ensquared energy = 70% DN	10 s exposure, 2 × 2 pixel sum, ensquared energy = 90% DN	10 s exposure, no pixel sum, ensquared energy = 22% DN	# stars of ≥ mag in WA FOV
0	21,000	27,000	6,500	0.06
1	8,200	11,000	2,600	0.16
2	3,300	4,200	1,000	0.37
3	1,300	1,700	410	0.9
4	520	670	160	2.2
5	210	270	65	5.2
6	82	110	26	12
7	33	42	10	30
8	13	17	4.1	71
9	5.2	6.7	1.6	180
10	2.1	2.7	0.66	420
11	0.84	1.1	0.26	1,000

Light gray boxes represent visual magnitude (M_v) values with <3 stars in FOV; dark gray boxes represent DN levels below 7× read noise or 7 DN for the WAC. White boxes show the range of M_v values meeting optical navigation requirements (≥3 stars per FOV at 7× read noise)

Fig. 6, a Data Processing Unit (DPU) for image processing, motor control, and commanding. By adding some additional boards to the DPU to support the other payload science instruments, a significant savings was achieved in spacecraft resources, design effort, and testing.

Table 5b NAC sensitivity to stars

M_v	10 s exposure, no pixel sum, ensquared energy = 43% DN	10 s exposure, 2 × 2 pixel sum, ensquared energy = 70% DN	10 s exposure, no pixel sum, ensquared energy = 30% DN	# stars of ≥ mag in WA FOV
0	19,700	32,000	14,000	0
1	8,000	13,000	5,600	0
2	3,100	5,100	2,200	0.01
3	1,300	2,000	890	0.01
4	500	820	350	0.03
5	200	320	140	0.08
6	80	130	56	0.2
7	31.33	51	22	0.48
8	12.29	20	8.8	1.2
9	5.04	8.2	3.5	2.8
10	2.03	3.3	1.4	6.7

Light gray boxes represent visual magnitude (M_v) values with <3 stars in FOV; dark gray boxes represent DN levels below 7× read noise or 14 DN for the NAC. White boxes show the range of M_v values meeting optical navigation requirements (≥3 stars per FOV at 7× read noise)
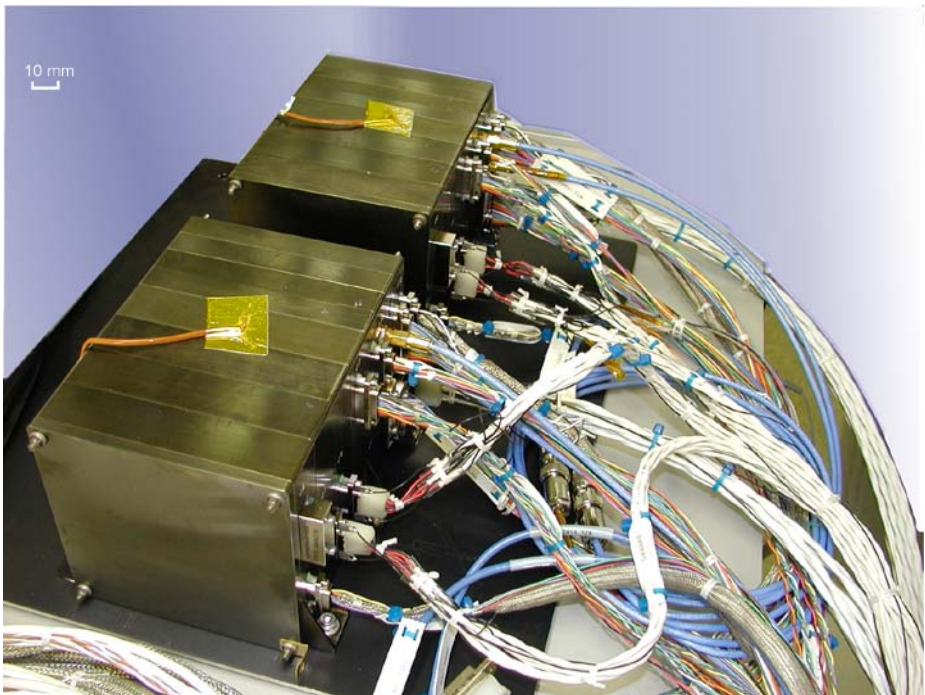
Fig. 6 Redundant Data Processing Units (DPUs) support the entire science payload. Photograph shows DPU-A and DPU-B with their flight harnesses configured for thermal-vacuum qualification tests
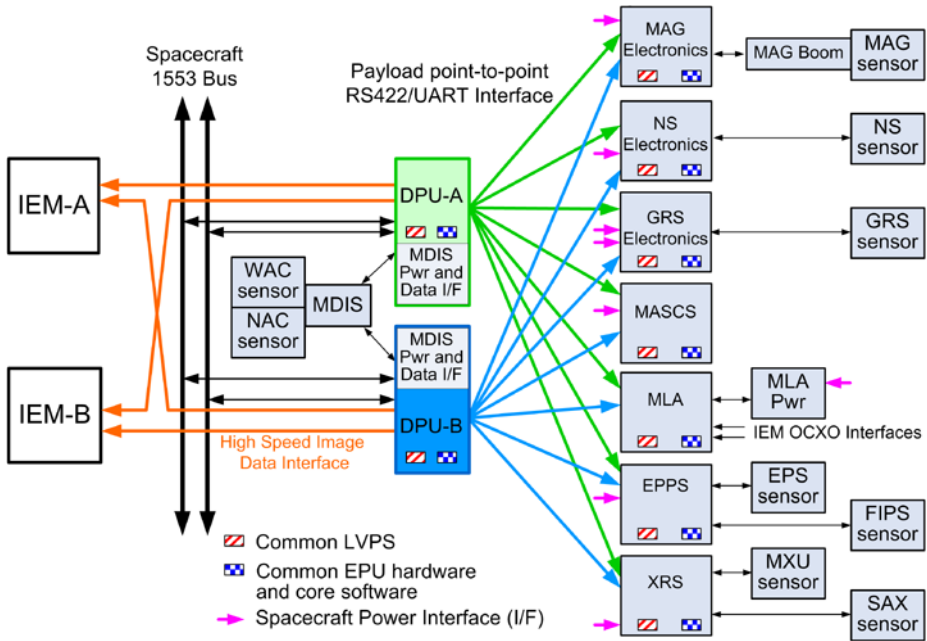
Fig. 7 High-level flow diagram showing relationship between the MDIS DPUs, spacecraft IEMs, and other science payload instruments (see Leary et al. 2007, and references therein). The redundant DPUs provide all processing and power (pwr) interfaces for MDIS, as well as the spacecraft interface for the other instruments. Note: SAX = Solar Assembly for X-rays; MXU = Mercury X-ray Unit; FIPS = Fast Imaging Plasma Spectrometer; EPS = Energetic Particle Spectrometer; GRS = Gamma-Ray Spectrometer; NS = Neutron Spectrometer

To increase the reliability of the payload, redundant DPUs were created to buffer all data interfaces between the payload elements and the spacecraft; one DPU is powered whenever a payload element is active, while the other DPU is maintained unpowered as a cold spare. The DPUs communicate with the spacecraft processors via the spacecraft MIL-STD-1553 busses (Leary et al. 2007), but they communicate with the instruments via separate dedicated RS-422 Universal Asynchronous Receiver Transmitter (UART) interfaces. The DPUs greatly simplified the spacecraft-to-payload interface issues, allowing payload development and testing separate from the rest of the spacecraft. Figure 7 provides a high-level flow diagram showing the relationship between the MDIS DPUs, the spacecraft Integrated Electronics Modules or IEMs (Leary et al. 2007), and the other science payload instruments.

Payload power and mass limitations impacted the design and operational constraints of the science instruments. The most limited power period for MESSENGER occurred during early cruise, when the solar arrays generated their lowest power, restricting the size of instrument heaters that could be used. In contrast, during the orbital phase of the mission, the solar arrays generate ample power, but during eclipse the battery power is still very limited. The instrument designs were limited by their ability to dissipate heat to the spacecraft deck or to the space environment.

The payload employs both distributed power and data processing for each of the instruments. Each instrument (other than MDIS) has its own power supply and microprocessor, thereby greatly reducing the risk of noise or software problems that could have impacted the

spacecraft integration schedule. This distributed interface architecture provided a balanced tradeoff between payload reliability, power, mass, and cost constraints.

Although each instrument has individual power supplies and processors, all but one of the instruments use a common power supply board and processor board. This commonality facilitated the use of identical power and data interfaces for the science payload. It also allowed common software modules that would handle a number of common tasks, including command and telemetry processing, timing, macro tools, data compression, and inter-integrated circuit (I^2C) bus mastering. This common software set greatly reduced the amount of code development required for each instrument and reduced risks for payload integration. Having these common power and data interfaces also allowed development of a common set of ground support equipment (GSE) hardware and software that emulated the DPU and power bus interfaces and provided a graphical environment for command menus and telemetry displays. The detailed description of the common low-voltage power supply (LVPS) and event processing unit (EPU) electronics is given in Sect. 3.4.3; the common software description is provided in Sect. 3.5.1.

3 Instrument Design

The full MDIS instrument includes the pivoting dual camera system as well as the two redundant external DPUs. The dual camera assembly without the DPUs is usually simply referred to as "MDIS." The overall design and look of the MDIS, shown in Fig. 1, was driven by mass limitations, the severe thermal environment, and the requirement for a large field-of-regard needed for optical navigation and off-nadir pointing. A functional block diagram of MDIS is shown in Fig. 8.
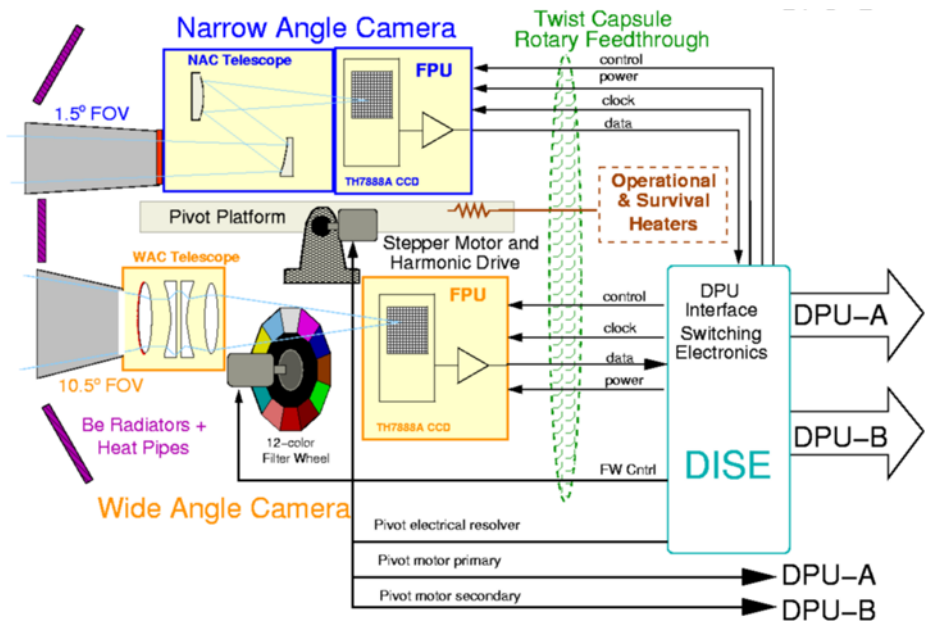

Fig. 8 MDIS does not communicate directly with the spacecraft, other than for spacecraft temperature sensors and heaters. All power, control signals, and data are cross-strapped through the redundant DPUs, as indicated in this functional block diagram for MDIS
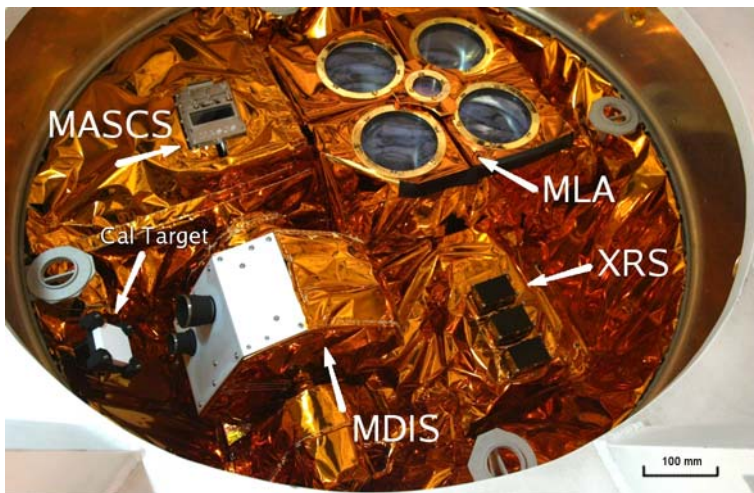
Fig. 9 Science instruments located within the payload adapter ring. The white calibration target was used during in-flight radiometric calibrations

On the pivot platform are the multispectral WAC and the monochrome NAC. A passive thermal design maintains the CCD detectors in the WAC and NAC within their operating temperature range of −45°C to −10°C. Only one DPU may be active at a time, and due to thermal constraints only one camera will operate at a time; however, observations with the two cameras can be interleaved at 5-s intervals. A separate electronics assembly accommodates switching between the various modes of operating with the redundant DPUs. The pivot platform has a large range of motion (∼240°) to allow the cameras to be "tucked away" to protect the optics from contamination. The pivot motor drive-train provides precision rotation over the 90° operational range of motion (Fig. 2) about the spacecraft +Z axis.

A spectral calibration target was mounted on the inside of the payload adapter ring. Early in the MESSENGER mission it was possible to tilt the spacecraft in order to provide solar illumination on the calibration target. The large range of motion of the pivot assembly enables either camera to point at the target, permitting an absolute in-flight radiometric calibration and flat-field measurement. Figure 9 shows the calibration target, along with the four instruments mounted inside the adapter ring. This picture, taken shortly before integration with the launch vehicle, shows the final blanket configuration of the instruments with MDIS pivoted for NAC observations of the target.

3.1 Optical Design

The WAC consists of a four-element refractive telescope having a focal length of 78 mm and a collecting area of 48 mm^2. The detector located at the focal plane is an Atmel (Thomson) TH7888A frame-transfer CCD with a $1,024 \times 1,024$ format and 14-µm pitch detector elements that provide a 179-µrad pixel (instantaneous) field-of-view (IFOV). A 12-position filter wheel (FW) provides color imaging over the spectral range of the CCD detector. Eleven spectral filters spanning the range 395–1,040 nm are defined to cover wavelengths diagnostic of different potential surface materials. The twelfth position is a broadband filter for optical navigation. The filters are arranged on the filter wheel in such a way as to provide complementary passbands (e.g., for three-color imaging, four-color imaging) in adjacent positions.

The NAC is an off-axis reflective telescope with a 550-mm focal length and a collecting area of 462 mm^2. The NAC focal plane is identical to the WAC's, providing a 25-μrad IFOV. The NAC has a single medium-band filter (100 nm wide), centered at 750 nm to match to the corresponding WAC filter for monochrome imaging.

One of several impacts of the thermal environment on calibration accuracy is the relative response of the CCDs at wavelengths longer than about 700 nm (Sect. 4.6.2). Response at longer wavelengths increases strongly with temperature (Janesick 2001). If data are acquired over a large temperature range, inaccuracies in correction for temperature-dependent response will introduce systematic errors in spectral properties at 850–1,000 nm that ultimately could lead to false mineralogic interpretations. To protect the MDIS CCDs from wide temperature swings, incoming thermal infrared (IR) radiation is rejected in the optics by heat-rejection filters on the first optic of each camera. In the WAC, this rejection is accomplished using a short-pass filter as the outer optic; for the NAC the bandpass filter has a specially designed heat-rejection coating on its first surface.

3.1.1 Wide-Angle Camera

Lens Design. The wide-angle camera (WAC) consists of a refractive telescope, dictated by the required wide FOV and short focal length. The design approach was to select the simplest lens design that gives acceptable image quality over the field; however, an important constraint on the design is the limited selection of glasses because of the radiation environment. The MESSENGER mission is expected to be subjected to a total dose of <15 krad (Si) (R. H. Maurer, personal communication, 2002). The design requirements were achieved by starting from a simple Cooke triplet and splitting the central negative element. The resulting design, a Dogmar (Fig. 10), gave good image quality although not over the full 395–1,040 nm spectral range. The uncorrected axial chromatic aberration was reduced by varying the thickness of each filter, a technique used in the NEAR Multi-Spectral Imager (MSI) (Hawkins et al. 1997).

The WAC is focused at infinity with a 78-mm focal length to spread the 10.5° FOV across the 14.3-mm detector. The 14-μm square pixels of the CCD provide an IFOV of 179 μrad. The selected aperture of $f/10$ means that the lenses, manufactured by Optimax, are quite small. Radiation-resistant glass was required, but only about 16 types were available. Fewer than half of these have adequate transmission below 400 nm. Of these, a combination of K5G20 and LF5G15 gave the best design solution. The optical transmissions of the coated samples of the two glasses used are given in Fig. 11.

Because of the mapping requirement for the WAC, the optical system must have very low distortion. The field curvature of the WAC produces a small focus variation across the field, but it has a negligible effect on the final modulation transfer function (MTF). The distortion has a maximum value of 0.06% at the corner of the field, which is less than a pixel. Figure 12 shows a representative MTF for the WAC. The two curves labeled "On-axis+diffraction" and "7°+diffraction" combine diffraction and the optical aberrations at these two field locations. Here, the wavelength used for diffraction is 700 nm. Because the design is diffraction limited
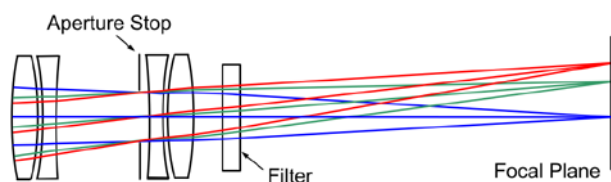
Fig. 10 Optical schematic of the WAC

Fig. 11 Nominal passbands and lens transmissivities for the WAC along with the quantum efficiency (QE) of the CCD
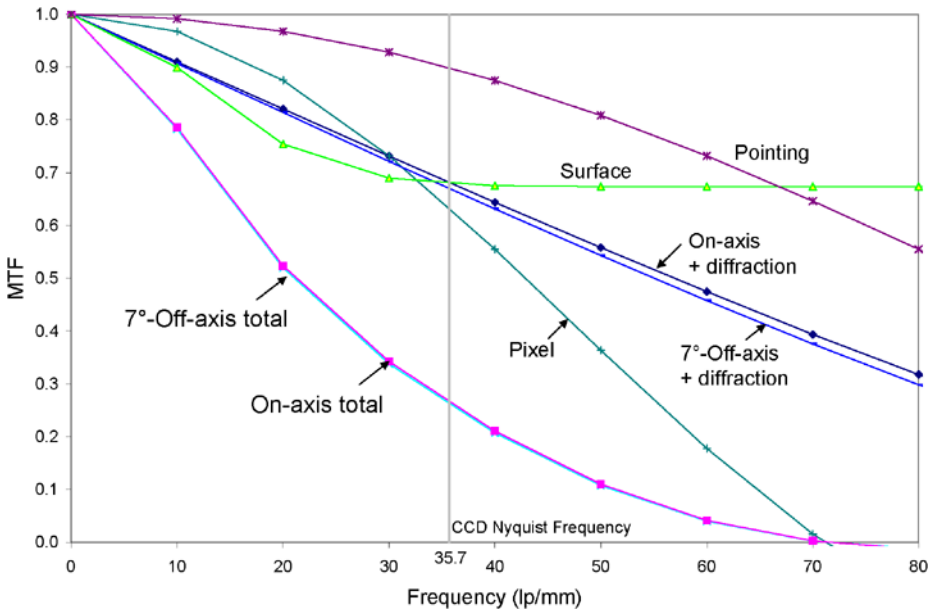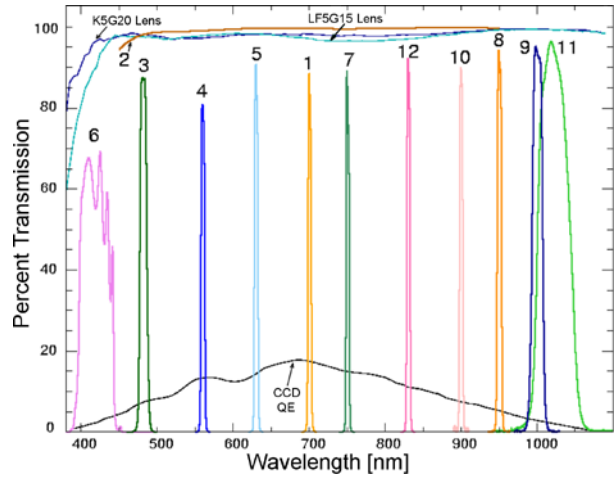

Fig. 12 Theoretical modulation transfer function (MTF) of the WAC. The various modeled contributors to the MTF are shown, with the product of these labeled "Total" for an on-axis ray and 7°-off-axis ray

over the entire field there is very little difference between the two lines. The figure shows that the MTF degradation is dominated by the pixel size at high frequencies (note the Nyquist sampling frequency of the detector). The surface degradation is dominant at low frequencies. The actual surface wavefront degradation here assumes a root mean square (rms) wavefront error of 0.1 waves through the system, including refractive index variations of the filter and lenses. Pointing has a small effect if the movement is limited to less than one-half pixel during an exposure.

The on-axis MTF value of 0.1 occurs at 50 line pairs per mm (lp/mm), or 3.9 lp/mrad, and is comparable to the Rayleigh criterion at which two features can just be distinguished. The resolution defined in this manner changes across the FOV from 0.26 mrad on-axis to 0.30 mrad in the corner.

Spectral Filter Design. A 12-position multispectral filter wheel provides color imaging over the spectral range of the CCD detector (395–1,040 nm). Eleven spectral filters are defined to cover wavelengths diagnostic of common crustal silicate materials and have full-width half maximum (FWHM) bandwidths of 5–40 nm (Table 6). A broadband clear filter was included for optical navigation imaging of stars. Because the optical signal at Mercury will be too high through the clear filter, the quality of the image through this filter was a secondary requirement.

Each filter consists of two or three pieces of glass using a radiation-resistant substrate of BK7G18 glass in combination with a long-pass filter glass. These colored glasses transmit efficiently over a specified wavelength and have a sharp cutoff at shorter wavelengths. The long-pass filter glasses are needed to block short wavelengths in the narrow bandpass filters of the WAC. Two filters required an additional layer of S8612 to achieve the desired passband. The designation G** added to the glass type identifies it as being radiation resistant. The number after the G gives the percent cerium times 10 used as the dopant. Standard glasses typically darken when exposed to radiation. Because of the uncertainty of the transmission degradation by radiation effects on the long-pass filter glasses used in the WAC filters, it was necessary to test the radiation effects on sample colored glasses provided by the filter manufacturer, Andover Corporation. The samples were made of high-quality Schott Glass that matched those used in the flight filters. The experimental setup and the results of the radiation tests are provided in Appendix 1.

The variation in filter thickness used to remove residual chromatic aberration results in a small variation in the focal length of the camera between filters. The extreme filters give a focal length of about 78 mm at 480 nm and about 78.5 mm at 1020 nm, respectively. Table 6

Table 6 Detailed specifications for the WAC filters and effective focal lengths

Filter number	System wavelength (measured at −26°C) (nm)	System bandwidth (measured at −26°C) (nm)	Peak transmission	Total thickness (mm)	Focal length (mm)	Scale change (%)
6	430	18	0.694	6.00	78.075	−0.216
3	480.4	8.9	0.875	6.30	77.987	−0.329
4	559.2	4.6	0.810	6.30	78.023	−0.283
5	628.7	4.4	0.898	6.20	78.109	0.173
1	698.8	4.4	0.892	6.00	78.218	−0.104
2	700	600	–	6.00	78.163	−0.104
7	749.0	4.5	0.896	5.90	78.218	−0.033
12	828.6	4.1	0.921	5.60	78.308	0.082
10	898.1	4.3	0.898	5.35	78.390	0.186
8	948.0	4.9	0.942	5.20	78.449	0.262
9	996.8	12.0	0.952	5.00	78.510	0.340
11	1010	20	0.964	4.93	78.535	0.372

lists the filters in order of increasing wavelength and identifies the number assigned to each filter, and the effective focal lengths for each one. This difference results in a variation in the image scale of 0.7%.

By positioning the filter in front of the detector (Fig. 10), the size of the filters is minimized. However, the incident angle θ of the beam on the filter varies with the FOV from 0° at the center to 14.9° at the corners of the 10.5°-square FOV. This angle will cause a shift in the spectral passband wavelength of the interference filters across the field according to the theoretical expression

$$\lambda = \lambda_o \sqrt{1 - \left(\frac{n_o}{n^*} \sin\theta\right)^2},$$ (1)

where n_o is the refractive index of the external medium ($n_o = 1$ in vacuum), and n^* is the refractive index of the filter substrate. The effect of the incident angle is much more serious than the spatial variations across the surface of the filter. With a maximum angle of 7.6° at the corner of the field, spectral shifts of ~3 nm are expected. The problem with this shift is that it is a variation across the FOV and not a constant offset; these small variations in passband, however, are not expected to limit mineralogic identification or the mapping of surface abundance variations.

Thermal Effects on Optical Design. The change of refractive index with temperature of glass K5G20 varies between -0.9 and $+1.0 \times 10^{-6}$/K, depending on the temperature and the wavelength. For LF5G15 the range is -0.9 to 2.0×10^{-6}/K. Thus, for a temperature change of 40 K the refractive index will change by a maximum of 8×10^{-5}. This is a negligible change, as the index changes by this amount with a wavelength change of only a few nanometers.

The performance of the WAC lens is almost constant with field angle over the design range, so it is not necessary to show the variation with field angle. It does, however, vary with wavelength, so compensation is added by varying the thickness of the filter between 1.7 and 2.9 mm. The results shown in Fig. 13 are for the spectral range 0.45–0.6 μm, over which there is very little change in the image quality with a single filter thickness. The lowest curve is for a nominal temperature of 20°C and vacuum operation. At atmospheric pressure the refractive index of air has a small effect as shown by the highest curve. The effect of temperature is negligible as the curves show the change in the spot sizes at temperatures of -20°C and $+20$°C. The rms spot radii in this figure are only 0 to 4 μm, which is very small compared with the radius of the diffraction disk, 8.5 μm at a wavelength of 0.7 μm. These results indicate that the WAC optical performance is insensitive to the operational temperatures of the instrument.

Stray Light Analysis. The optical design of the WAC took into account various sources of stray light including scatter from the optical surfaces, intrascene scatter, spurious reflections between optical surfaces, and scatter from the CCD detector. Scatter from external surfaces such as the optical housings, WAC light-shade, and surface contamination were also considered. However, at Mercury, MDIS will be exposed to a radiance source of large angular extent. On orbit, the planet itself will be the dominant source of stray light.

The light-shade of the WAC was constrained in size and complexity because of mass limitations. In addition, because the pivot platform was required to rotate 180° to stow the cameras for launch and other possible contamination events (e.g., large thruster firings and orbital insertion), the overall length of the shade was constrained. A two-piece shade was constructed in order to minimize the size of the hole in the beryllium radiator needed for
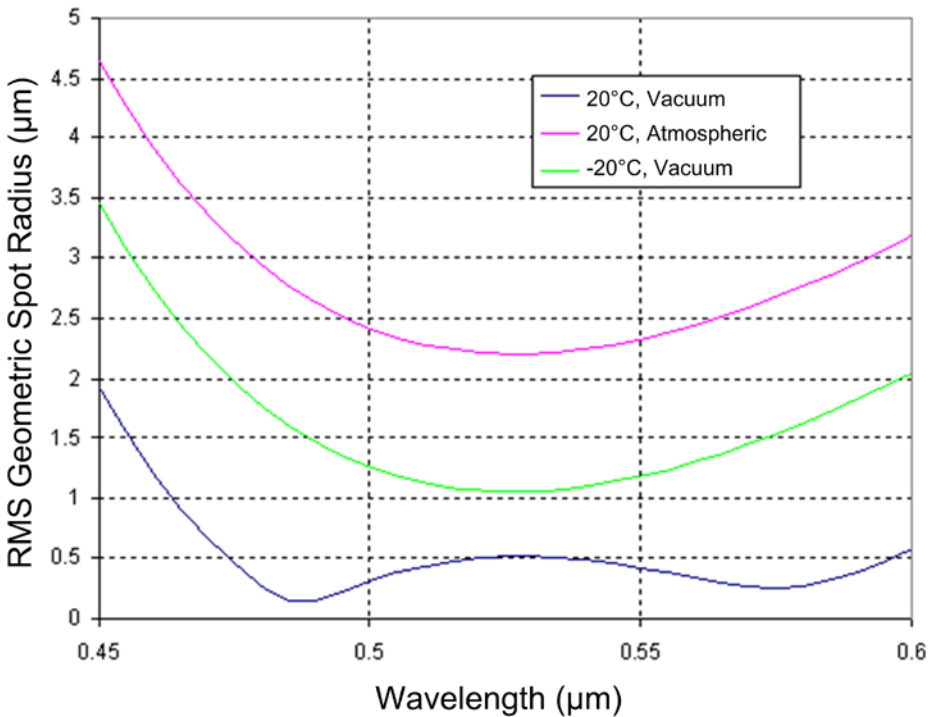
Fig. 13 Variation of WAC geometric spot radius with temperature as a function of wavelength. Residual chromatic aberration over wavelength has been compensated by varying the filter thickness from 1.7 to 2.9 mm. The variations shown are much less than a pixel (14 μm square)

the light-shade to pass through, yet be large enough not to constrain the FOV. Concentric grooves were machined into the titanium light-shade to minimize direct scatter into the system from the shade.

Extensive measurements were made during ground calibration of the WAC to characterize the effect of stray light in the camera. However, limitations of the experimental setup made separating chamber-induced stray light from internal scatter in the optical system of the WAC difficult. In either case, all of the ground-based observations to characterize stray light in the WAC showed the contribution to be small, on the order of 0.1% of the response of the small extended source (lamp filament ∼7 pixels) viewed on axis. In-flight calibrations will be made to characterize the stray light performance of the WAC further.

3.1.2 Narrow Angle Camera

The primary purpose of the NAC is for high-resolution imaging of Mercury. Because of the very bright optical signal from the planet, a large collecting area is not required for sensitivity; the need to reduce blurring from diffraction, however, dictated a large (24 mm) aperture. The reflective design has a long focal length that required folding the optical path in order to fit in the available volume. The all-aluminum mirrors and telescope housing were assembled and tested by SSG Precision Optronics, Inc. The monochromatic design has a single medium-band filter centered at 750 nm with a FWHM of 100 nm. The center wavelength was chosen to match filter 1 of the WAC (cf. Table 6).

Fig. 14 Optical schematic of the NAC
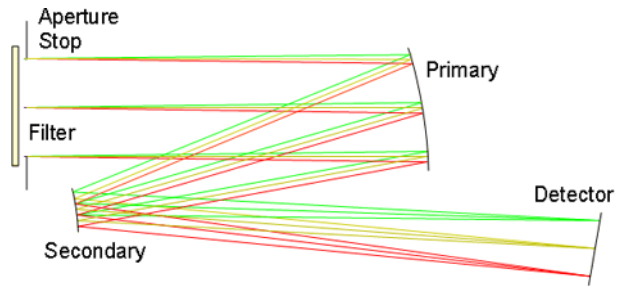
Telescope Design. The NAC has a 1.5° FOV that is spread across the 14.3-mm detector, requiring a focal length of 550 mm. To limit the diffraction blur, the NAC has a 24-mm aperture, resulting in an $f/22$ system. An off-axis Ritchey-Chretien design was selected over a simple Cassegrain in order to avoid the central obscuration of the secondary mirror. The optical ray trace is shown in Fig. 14. The ellipsoidal primary mirror and hyperboloidal secondary mirrors are gold-coated aluminum with a surface roughness of 0.1 nm and 0.2 nm, respectively. In this design, the image plane is tilted at an angle of approximately 9° for optimal image quality.

A bandpass filter is the first optical component of the assembly and defines the spectral range of the instrument. A specially designed interference coating serves as a heat-rejection filter. Mercury absorbs solar radiation and reradiates this energy back into space. Because of its slow rotation, the dayside of the planet can be modeled as a 400°C blackbody (Hansen 1974). The radiation from this blackbody results in a significant amount of IR radiation that would pass through the NAC interference filter and heat the CCD. Figure 15 shows the transmission of the interference filter for the NAC, with the response of the CCD superposed on it. In addition, the reflectance spectrum of the heat-rejection coating is plotted with a normalized 400°C blackbody spectrum.

Figure 16 shows the spot diagrams corresponding to selected field angles for the NAC. The location of the focal plane was selected to balance the image quality across the field. The circle shows the Airy disk. Low distortion of the image was an important design specification for the NAC. At the higher orbital altitudes, the NAC will be used to complete the nadir and off-nadir mosaics at high resolution. The theoretical distortion of the NAC is 0.25% at the corner of the field. At the edge of the FOV this amounts to 1.28 pixels. The all-aluminum assembly of the NAC makes it insensitive to thermal distortions over the operational temperature range of the instrument. Figure 17 shows a representative MTF for the NAC in the same format described earlier for the WAC.

The aperture stop is located in front of the primary mirror. Figure 18 shows the geometrical spot radius out to an angle of 0.75°, the edge of the FOV. Note that the corners of the field are 1.06° off axis. The geometrical performance is excellent, and the upper line shows the limit imposed by diffraction.

Stray Light Analysis. The narrow FOV makes the NAC less sensitive than the WAC to off-axis sources, making the need for a long light-shade less critical. Mass and size limitations further constrained the light-shade design to be simple, without any internal baffling of the light-shade. The effects of this approach for the NAC light-shade were analyzed by considering a full hemispherical illumination of the NAC, representative of imaging at Mercury. This calculation shows that the scattered radiance as a fraction of the surface radiance of the out-of-field stray light is negligible for this system, even with no light-shade at all. The two
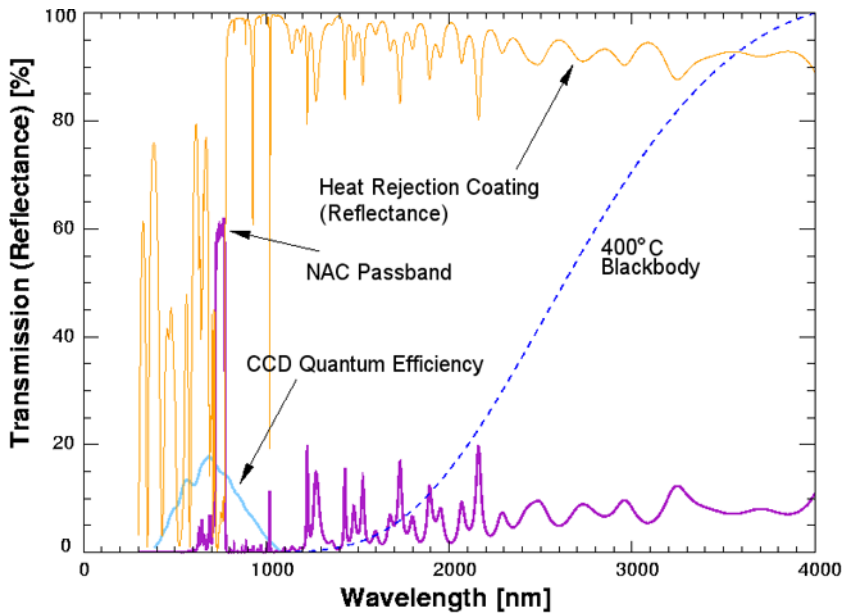
Fig. 15 The monochromatic NAC spectral passband (700–800 nm) is shown overlaid on the quantum efficiency response of the TH7888A CCD. Also shown is the heat-rejection coating specifically designed to reflect the longer IR wavelengths radiated from the hot planet, assumed to be a 400°C blackbody (shown in the figure in dimensionless units)

Fig. 16 Spot diagrams for selected field angles (azimuth, elevation, both in degrees) for the NAC. The diffraction-limited performance of the telescope is apparent when compared with an Airy diameter of about 38 μm or 2.7 pixels (*solid circle* in each diagram)
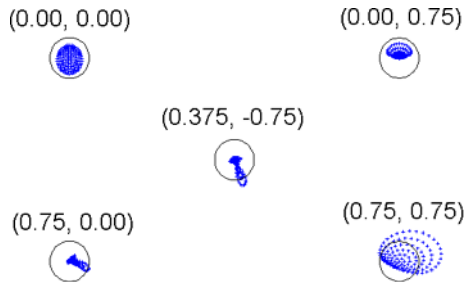
main reasons for including the light-shade were to provide a surface to project through the thermal system and to provide protection from stray light for optical navigation.

The NAC filter is mounted in the NAC light-shade and is tilted at 1° from boresight to prevent direct scatter back onto the detector. With the final light-shade design and filter in place, the calculated bidirectional transmittance distribution function (BTDF) has a value of 0.01 at 1° with a slope of −2; this value is typical for an optical surface. A combination of analytical and empirical methods was employed to identify and minimize scattered light in the NAC telescope. Off-axis light entering the imagers will hit the internal walls or baffles and be mostly absorbed by the black paint. As the absorption is not perfect some residual scattering will result. No direct path exists to the detector, and most scatter requires striking a minimum of two surfaces.

Off-axis rejection in the NAC was modeled extensively using the software package TracePro® and the detailed computer-aided design model of the optics. The calculated level
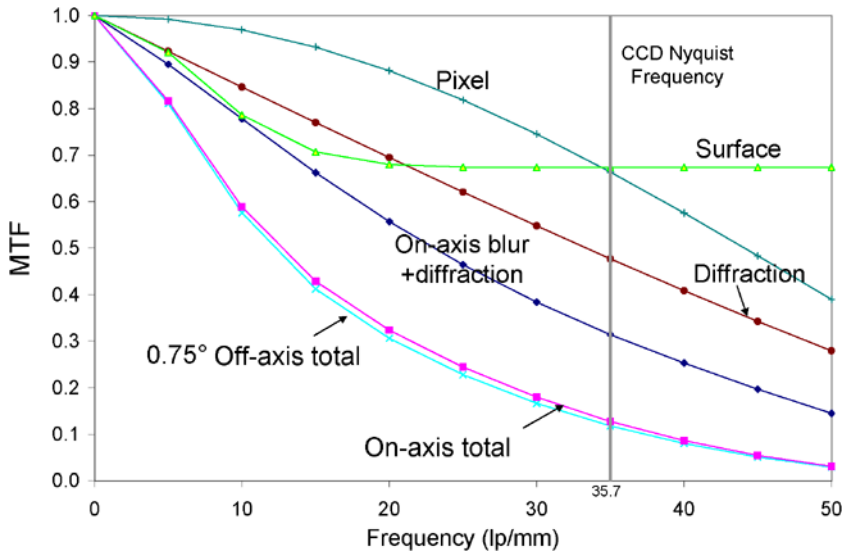
Fig. 17 Theoretical modulation transfer function (MTF) of the NAC. The various modeled contributors to the MTF are shown, with products of these labeled total for an on-axis ray and a 0.75°-off-axis ray
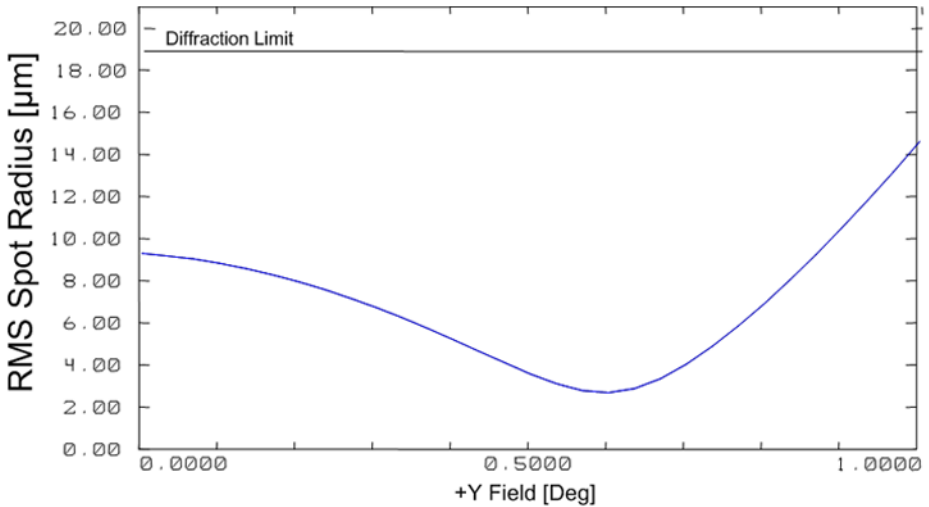

Fig. 18 Geometrical spot radius as a function of field angle for the NAC

of rejection in the NAC is below 0.01%. Measurements to characterize stray light in the NAC were acquired during ground calibration. However, as with the WAC, difficulties in separating out internal camera scatter from scatter induced by the test chamber made measuring the scattered light performance difficult. The measured results still show scattered light rejection below 0.1% of the response of the small extended source (lamp filament ∼60 pixels) viewed on axis in the NAC.

Thermal Effects on Optics. The all-aluminum structure of the NAC telescope and gold-coated aluminum mirrors was selected to minimize any thermal distortions to the optical system. The telescope mechanical interface to the Focal Plane Unit (FPU) is a highly polished surface, and the input end of the telescope is supported by a titanium flexure mount. To minimize heat entering the system, a heat-rejection coating was applied to the NAC filter as discussed earlier. The filter housing is also the light-shade and is made of titanium to reduce heat flow into the telescope. The light-shade is painted black, as are the internal surfaces of the telescope and FPU. The optical performance was verified over temperature by measuring the wavefront distortion of the NAC telescope.

3.2 Electronics

The electronics systems of MDIS are fundamental to all aspects of the MESSENGER payload. Not only do the fully redundant Data Processing Units (DPUs) provide the interface between MDIS and the spacecraft, but each DPU also provides the interface for all the other payload instruments as well. Because of all the redundant systems built into the spacecraft, cross-strapping of these systems proved to be a significant task. The main electronics systems of MDIS include the DPUs, the DPU Switching Interface Electronics (DISE) box, and the FPU camera electronics.

3.2.1 Focal Plane Electronics

The detector electronics for both the WAC and NAC are identical. The top-level block diagram of the FPU is shown in Fig. 19. However, each CCD is bonded to a camera-specific mounting bracket (heat-sink) prior to assembly into the FPU electronics. The NAC heat-sink is tilted 9° to match the optimal orientation of the NAC focal plane, whereas the WAC heat-sink has no tilt. Because of this unique mounting configuration for each camera, once the CCD-heat-sink assembly is integrated into a set of FPU electronics, the electronics are no longer mechanically identical and are uniquely defined as a NAC or WAC FPU.
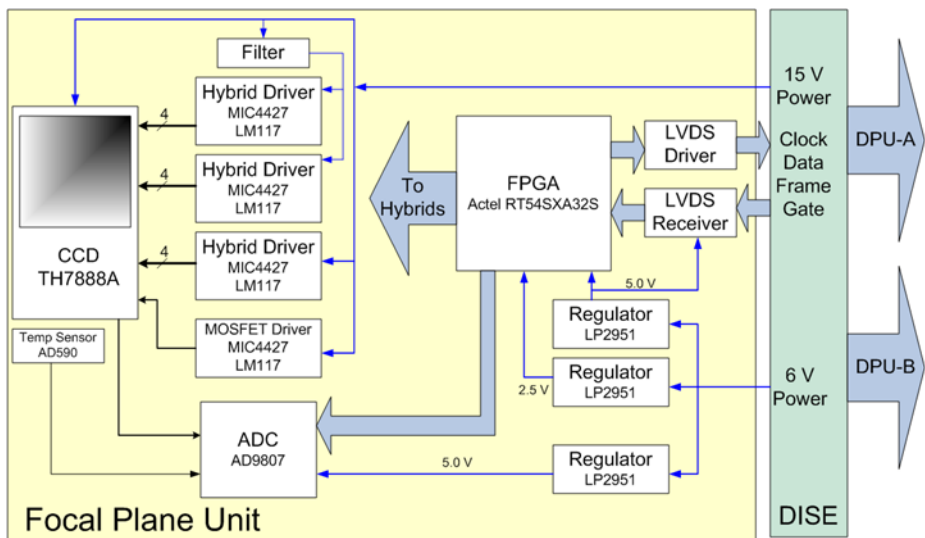

Fig. 19 Block diagram of the MDIS Focal Plane Units and the DPU Interface Switching Electronics (DISE) box. The NAC and WAC FPU electronics are identical in design

Performance Flowdown.   Each modular FPU contains a 1-megapixel CCD that has 14-μm square pixels and antiblooming control. Due to thermal, power, and operational constraints, only one camera operates at a time. The frame rate of each FPU is fixed at 1 Hz; however, the frame rate to the spacecraft is not fixed but cannot exceed 1 Hz. Manual and autoexposure control from 1 ms to ∼10 s permits imaging over a broad range of intensities.

The requirement for a $1{,}024 \times 1{,}024$ format imager with electronic shutter and antiblooming dictates the general design of CCD that must be used. On-chip binning is required in order to achieve the 1-Hz data throughput to the spacecraft solid-state recorder (SSR) and for data compression. The sensitivity required is not very difficult to achieve, although the relatively short exposures, typically >7 ms, require a commercial rather than scientific type of CCD. The frame transfer time is 3.84 ms, limiting the minimum useful exposure to about 8 ms, and this limit requires post processing to recover a clean image (Murchie et al. 2002).

General Design Considerations.   A CCD from Atmel (formerly Thomson-CSF), the TH7888A, was chosen because it was a good match for the requirements and also enabled design experience gained with the Comet Nucleus Tour (CONTOUR) Remote Imager/Spectrograph (CRISP) instruments (Darlington and Grey 2001) to be used. The nominally $1{,}024 \times 2{,}048$ pixel array of the TH7888A has two on-chip output amplifiers (only one amplifier is used in the MDIS design) and uses frame transfer to obtain electronic exposure control. The active image forms an array of $1{,}024 \times 1{,}024$ in which optical energy is accumulated. At the end of the exposure period, the accumulated charge in each pixel is quickly transferred to the masked-off $1{,}024 \times 1{,}024$ memory zone. A tantalum radiation shield not only protects the CCD from ionizing radiation but also blocks illumination to the memory zone as shown in Fig. 20.

The CCD is operated in two modes: binned and full-frame. In the full-frame mode for either the WAC or NAC, the first four columns of each image are taken from a region of the CCD that is never exposed to light and, thus, represents a dark level that is purely a function of bias and dark current. The dark columns are separated from the image section by five isolation columns to avoid diffusion of signal from the active area. When the image is read out, these four columns are mapped into the first four imaging columns, so the resulting image is a square $1{,}024 \times 1{,}024$ pixels, with the first four columns replaced with the sampled dark columns.

Fig. 20 The Atmel (Thomson) TH7888A CCD with its tantalum radiation shield in place protecting the memory storage zone of the frame-transfer-type device
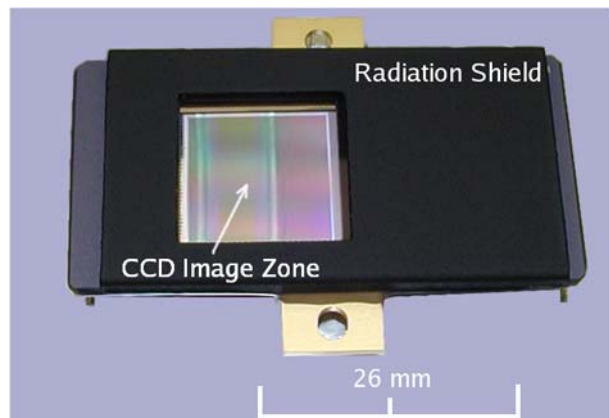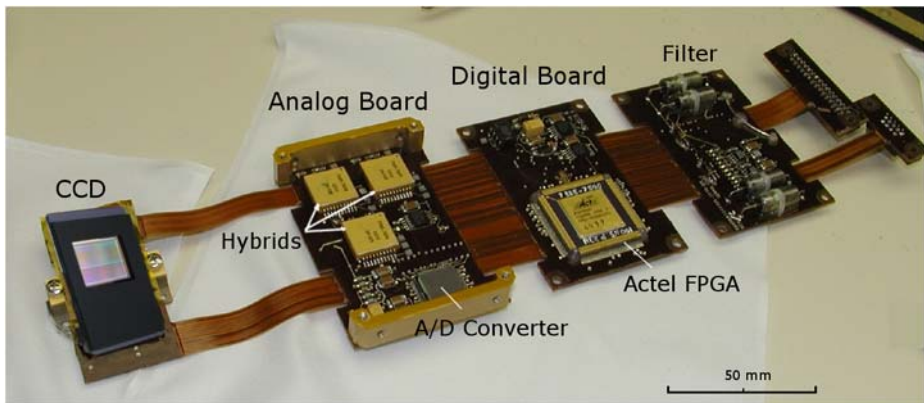
Fig. 21 Focal Plane Unit electronics, comprised of multiple rigid flex boards that fold into a compact design

Because of the severe mass limitations imposed on all aspects of the MESSENGER mission, the camera electronics were required to be smaller than the CONTOUR/CRISP FPU electronics on which the design was based (Darlington and Grey 2001). A hybrid incorporating considerable parts of the clock driver circuits was developed by The Johns Hopkins University Applied Physics Laboratory (APL). A type of construction of the printed circuit boards known as rigid-flex enabled the electronics to be folded into a small space (Fig. 21). The clock drivers use an integrated circuit (IC) designed to drive the gates of power metal oxide semiconductor field effect transistors (MOSFETs) and are almost ideal to drive the capacitive gates of a CCD. The Atmel CCD requires drive levels, speeds, and currents that are compatible with the drivers. The TH7888A has a relatively high internal gain of 6 μV/e. This value is large enough to drive the correlated double sampler analog-to-digital converter (ADC) integrated circuit, made by Analog Devices, directly while meeting the system noise requirements. The output is a 12-bit digital word for each CCD pixel value. A field-programmable gate array (FPGA) is used to provide clocks for the CCD and ADC derived from an input clock from the DPU. The DPU also provides a coded exposure time signal for the camera, as the autoexposure algorithm is in the DPU. Figure 22 shows the detailed timing for short exposures (<1 s) in the top panel and long exposures ($1 <$ exposure < 10 s) in the bottom panel. The FPGA also formats the data for transfer back to the DPU. The interface between cameras and DPU uses low-voltage differential signaling for low noise and to tolerate differences in grounding between the units.

During normal operation the CCD is read out once per second whether or not images are being saved. This action sweeps out accumulated dark current in the detector. The only time this sequence is interrupted is when exposures of longer than one second are being made. The CCD also has an antiblooming gate which removes accumulated dark current from the image area before the start of an integration by effectively setting the full well size to zero.

Hybrid and Power Conditioning. The hybrid incorporates two driver ICs and a linear regulator with various decoupling and bias components into a package a little larger than a single-driver IC. Figure 23 shows the MDIS hybrid with its lid removed and the two driver ICs and linear regulator magnified. One hybrid can provide four CCD clocks, and a total of three hybrids is needed by each camera. The frame transfer process, which takes place in 3.84 ms, repeatedly drives high capacitance lines to transfer an exposed image from the image area to the storage area of the CCD. The result is a large current requirement every
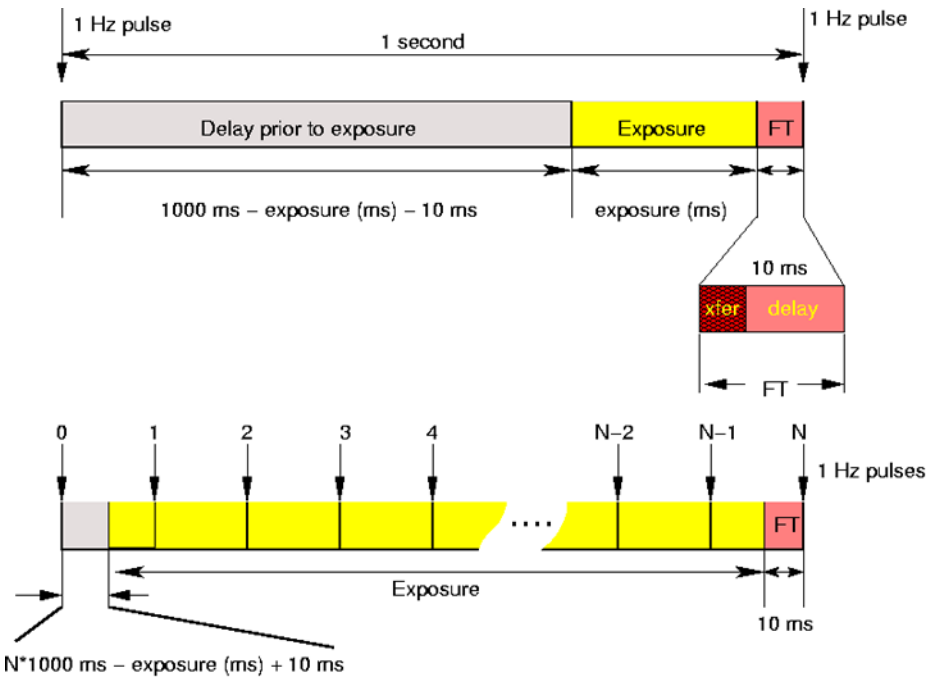
Fig. 22 Detailed frame timing for the FPUs. All clocking, control, and readout of the CCDs is generated within the FPGA in the FPU. The actual frame transfer (FT) time (xfer) is 3.84 ms

Fig. 23 The development of a hybrid driver component significantly reduced the overall size of the MDIS FPU electronics over earlier designs. (**A**) Custom hybrid component with lid removed showing external leads and relative size.
(**B**) Enlargement of the two MOSFET-driver integrated circuits and linear regulator.
(**C**) Detailed view of one MOSFET driver.
(**D**) Enlargement of the LM117 linear regulator
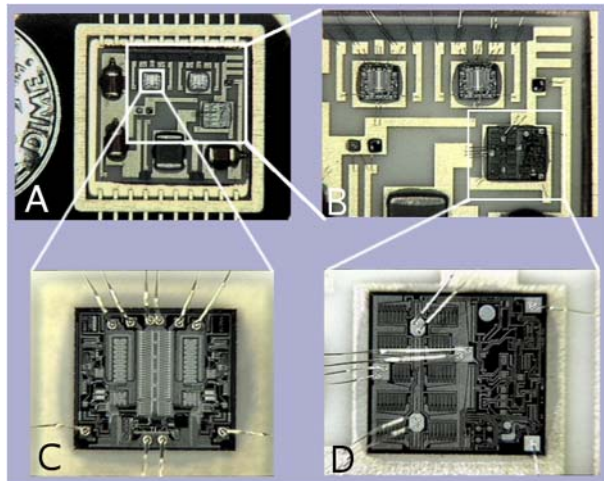
frame, occurring for a few milliseconds each second. This current would be enough to overload the converter driving the camera if it appeared at the power input. To avoid overload, simple passive filtering is incorporated in the camera (see Fig. 19) to reduce the current surge to an acceptable level.

Table 7 Requirement flowdown for the MDIS camera detector electronics

Description	Requirement
Size of image plane	1,024 × 1,024 pixels, 14 × 14 μm
Other formats	2 × 2 binned (512 × 512)
Spectral coverage	400–1,100 nm
Electrical dynamic range	Up to 4,000 : 1
Noise level	50 electrons
Exposure range	1 ms to 10 s
Linearity	<1 %
Operating temperature, CCD	−40°C to −10°
Operating temperature, housing	−40°C to +30°C
Power consumption	<2 W

Test and Performance. The completed camera boards underwent a variety of electrical tests before the CCDs were installed to ensure that they had the expected electrical performance. After CCD installation, the camera design was tested with optical input to verify the performance requirements.

In general the cameras met the requirements shown in Table 7 without difficulty. The dark current for long exposures causes a small shift in dark level. The CCD provides specially shielded columns to provide an accurate measure of the dark level. Four of these dark pixels are sampled per line and substituted during readout, for four of the 1,024 active pixels in a full-resolution image (1,024 × 1,024). The four reference columns provide a measure of the dark background. In the case of 2 × 2 binning, no valid dark reference pixels are available.

The antiblooming feature of the CCD causes a scene-dependent nonlinearity. This nonlinearity is an artifact of the earlier design on which this one was based. The extent of the nonlinearity was measured to be below the required upper bound. When large areas of the focal plane array are illuminated, there is no measurable nonlinearity. However, there is some evidence that when small regions of the array are brightly illuminated, the linear response could be outside the specification.

3.2.2 DISE

The MDIS instrument contains six major electrical subsystems: two FPUs, a filter wheel motor, a filter wheel motor resolver, a platform pivot motor, and a platform pivot motor resolver. The pivot motor contains redundant windings with one set going to each DPU. The remaining systems must be controllable by either of the two redundant DPUs. Selection between these units is provided by a DISE box. The DISE box is identified in Fig. 1, and the overall signal flow is shown in Fig. 24.

The DISE box switches between the DPU and MDIS electronics while minimizing the connections through the rotary twist-capsule feedthrough. There are two switching functions: one selects which DPU is master and the other selects which camera will be active. For the DPU selection, latching relays are used. When a DPU powers up, it asserts itself as master by pulsing primary voltage on a control line to the DISE board. This pulse switches relays that control the power and signal interfaces to the cameras. This pulse also switches relays that pass DPU commands to the filter wheel, filter wheel resolver, and pivot motor resolver. There is one relay for each control line needed for these interfaces. After the DPU asserts itself as master, it then applies power to the camera of interest. Each DPU provides separate power lines for each camera. The DISE board uses these power connections to
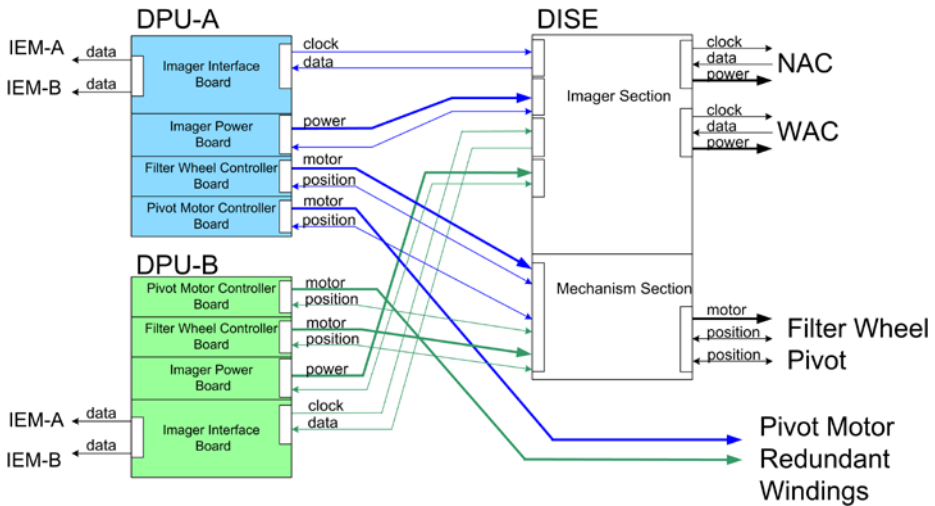
Fig. 24 Detailed interface showing power and signals from redundant DPUs through the DISE box. Mechanical relays in the DISE box are switched depending on which DPU provides power to the DISE box. The DISE box also selects which camera communicates with the DPU. The LVDS protocol used for all control signals and data largely eliminated any length constraints for the harness. However, cable runs between the DPUs and DISE were kept to a minimum for mass considerations

power its internal circuitry that selects the correct camera as well as powering the camera of interest. This selection is done in a master/slave configuration with the NAC having priority. If power is supplied to both cameras at the same time, signals from the NAC will be transmitted. This arrangement ensures that the master DPU communicates with the intended camera.

In addition to delivering each camera with the 15 V provided by the master DPU, the DISE box linearly regulates a 6-V supply. This regulation is done in the DISE box to limit power dissipation and reduce mass in the cameras. An FPU draws significant current at 6 V; the linear regulators therefore dissipate the majority of the 1.7 W of the DISE box. To ensure good thermal conduction of these components so that they can safely dissipate their heat, they are mounted directly to the lower corners of the DISE box frame. Since the DISE box physically mounts onto a thermally nonconducting composite stand of the MDIS bracket assembly, a copper thermal strap conductively ties the DISE box to the spacecraft deck. A Nusil thermal gasket was used to ensure excellent thermal contact between the copper heat-sink and the deck of the spacecraft.

The DISE box switches control lines using the low-voltage differential signaling (LVDS) protocol to and from each camera. Each camera has a single LVDS interface, and each DPU has a single LVDS interface. Switching between them is done with cold-sparing LVDS receivers and cold-sparing complementary metal oxide semiconductor (CMOS) multiplexers. The power and enable signals for the LVDS and multiplexer chips, shown schematically in Fig. 25, are derived from the active 15-V DPU camera supply power.

3.2.3 Data Processing Unit

The DPU electronics provide two distinct services: they act as a communications router and interface between all the instruments and the spacecraft, and they provide complete support
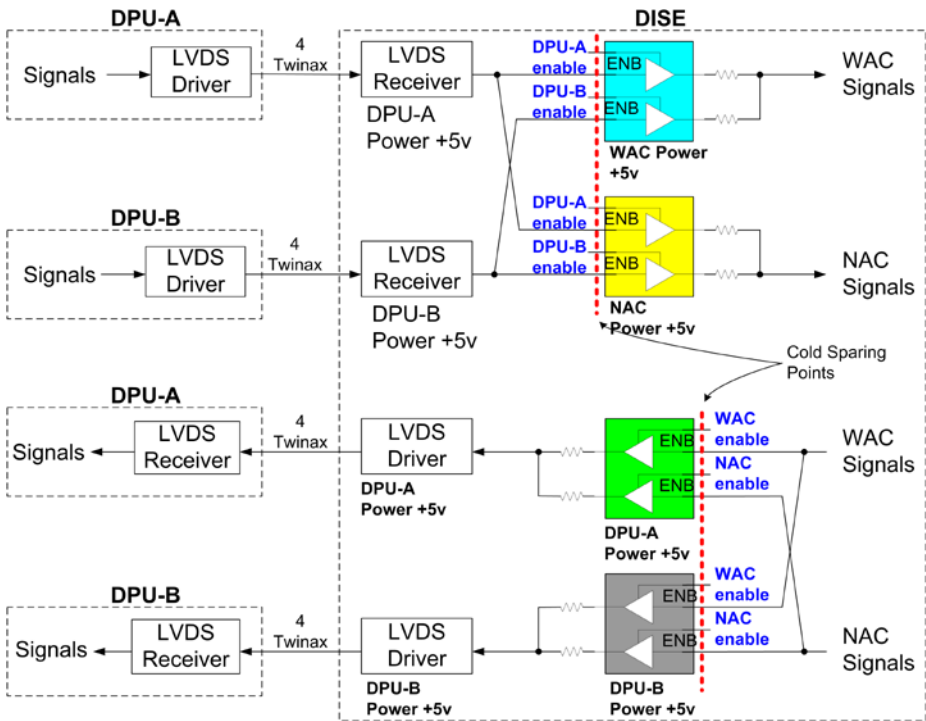
Fig. 25 Low-voltage differential signaling (LVDS) interface between the redundant DPUs and MDIS. Cross-strapping takes place in the DISE box, which selects either a WAC or a NAC through the enable (ENB) of a tri-state bus transceiver when commanded from the active DPU

for the MDIS camera electronics. Two separate sets of electronics boards are physically stacked and packaged together. Figure 26 shows a block diagram of the DPU. The first set of boards, comprised of the LVPS, EPU, and UART hub board, provides basic power conditioning, data processing, and communications functions. The second set supports only MDIS and is comprised of two motor controllers, WAC and NAC power supply boards, and a single imager interface board. The EPU and LVPS boards are common designs that are used in all instruments (except MLA).

Event Processing Unit (EPU) Board. The EPU board, one of the two boards of the common payload design, provides data processing capability and creates the telemetry data packets passed (through the DPU) to the spacecraft. The design was based heavily on versions that were flown on earlier instruments built at APL, including the Imager for Magnetopause-to-Aurora Global Exploration (IMAGE) High Energy Neutral Atom (HENA) and CONTOUR CRISP and Contour Forward Imager (CFI) instruments. All these designs are based on the Intersil (formerly Harris) RTX2010 16-bit processor. This processor, used in many APL instruments and spacecraft subsystems for the past 15 years, directly executes Forth language instructions. On MESSENGER the processor is operated at 6 MHz and can provide approximately 6 million instructions per second of processing power.

In addition to the RTX2010, the EPU board contains 64 KiB of fuse-link programmable read-only memory (PROM) for boot code, 256 KiB of electrically erasable PROM (EEPROM), and 256 KiB of SRAM. An Actel RT54SX32S FPGA provides all the logic
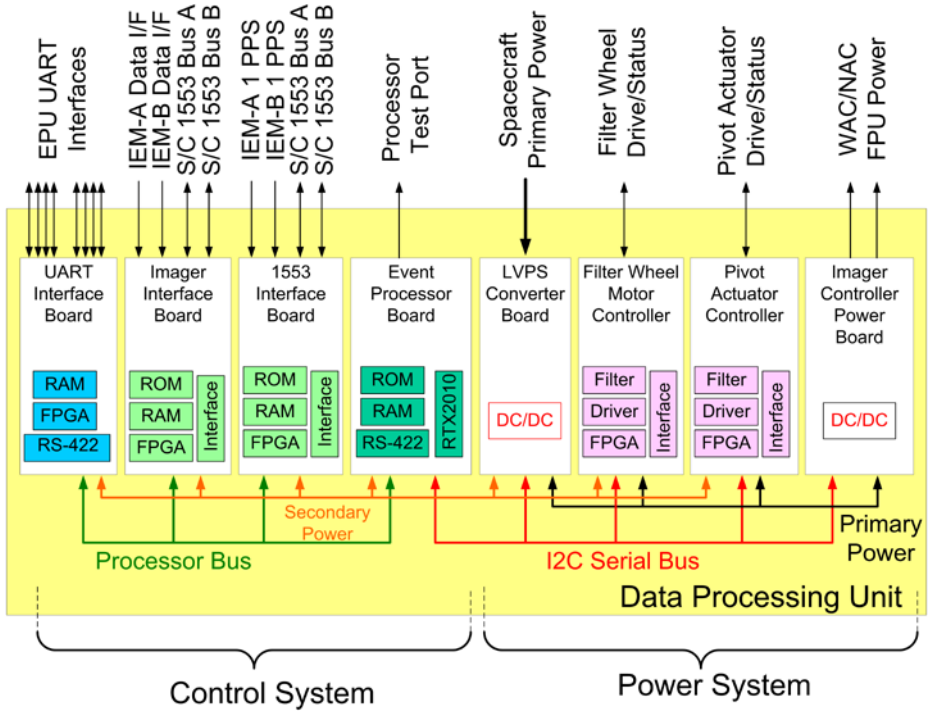
Fig. 26 Block diagram of the MESSENGER DPU

necessary to interconnect the processor with the stacking connector data bus, as well as implement the interface UART (running at 38.4 kbaud) to the DPU, the test port UART (running at 19.2 kbaud), and an I²C bus to control off-board serial peripherals. The EPU also receives (via the DPU) a once per second timing pulse from the spacecraft. This timing "SYNC" signal originates at the spacecraft IEM oven-controlled crystal-oscillator (OCXO or coarse clock) and is used as an interrupt to the processor to maintain timing synchronization throughout the payload. This synchronization pulse is a key part of the overall time-keeping design to maintain <1 ms end-to-end timing error between the mission operations center and the payload.

Low-Voltage Power Supply. The LVPS board converts spacecraft primary power, ranging from 20 to 36 V, to isolated secondary power. The common payload LVPS design was based heavily on versions that were flown on the CONTOUR CRISP and CFI instruments.

Most of the instruments operate from only four output voltages: ±5 V and ±12 V. The EPPS instrument (Andrews et al. 2007) uses ±15 V instead of ±12 V. In addition to providing four secondary outputs, the converters also provide power switches for auxiliary primary power loads and some analog housekeeping capability.

A design tradeoff was made between the use of a customized converter design and one based on commercially available hybrid converters. Although a customized approach would have provided better overall power efficiency, the cost and schedule limitations had a significant impact on the decision to use the VPT, Inc., family of converters, based primarily on their small size and low noise output.
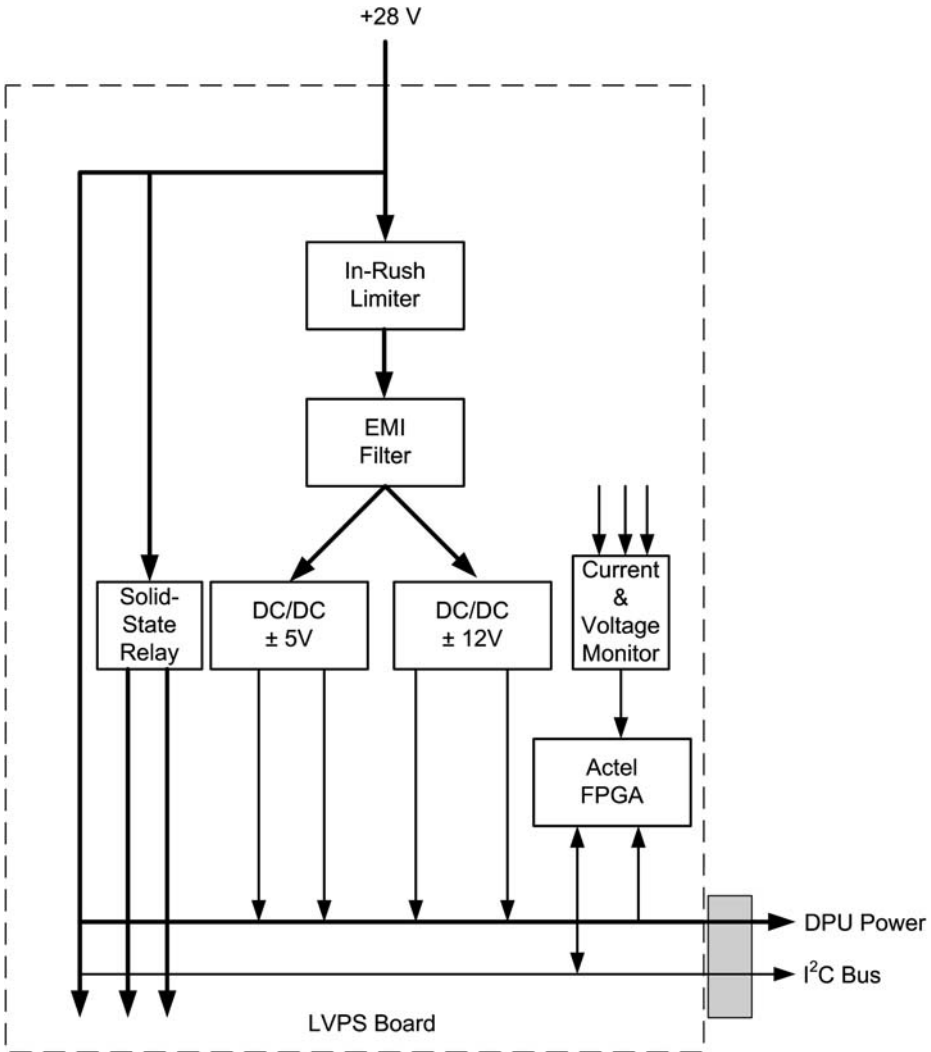
Fig. 27 Block diagram of the low-voltage power supply board, one of the two boards common to all the instruments (except MLA)

The functional block diagram for the LVPS board is shown in Fig. 27. The LVPS board uses an in-rush limiter, a VPT electromagnetic interference (EMI) MIL-STD-461 filter, and two VPT hybrid dual-output converters (one for ±5 V and the other for ±12 V). These converters provide better than 1% load and line regulation for nominal operation and good step response. Two radiation-hardened opto-field effect transistor (FET) relays were used to switch up to 1 A of primary power to off-board loads. An analog monitoring circuit, comprised of a 14-bit ADC, instrumentation amplifiers, a 16-1 multiplexer, and an Actel FPGA, provided 16 input analog channels, which were used to monitor four voltages and six currents on the board and five user-provided analog voltages from off the board; the remaining channel measured board temperature.

Table 8 MESSENGER payload requirements on the common low-voltage power supply board design

Instrument	Load on ±5 V	Load on ±12 V	Total power out (mW)	Estimated efficiency on ±5 V	Total efficiency
XRS	2,550	480	3,030	65%	55%
GRNS	3,250	1,440	4,690	67%	65%
EPPS	2,950	1,440	4,390	67%	65%
MAG	1,250	720	1,970	55%	48%
MDIS	1,000	480	1,480	50%	41%
DPU	3,250	0	3,250	67%	67%
MASCS	0	480	480	67%	30%

A major challenge in using a single-power-supply design for multiple instruments was the ability to handle varying load requirements. Table 8 shows the range of output loads between the payload elements that used the common LVPS board. A drawback of these dual-output hybrid converters is the need to provide a minimum load on each output to ensure that both outputs remained in regulation; however, this constraint did not result in any significant power losses.

UART Hub Board. Communication between each DPU and the instruments (other than MDIS) takes place through a Universal Asynchronous Receiver/Transmitter hub. This board uses an Actel RT54SX32S FPGA, 1 MiB of static read-only memory (SRAM), and a number of RS-422 receiver and transmitter circuits to implement eight 38.4-kbaud, RS-422, full duplex UART channels. Each channel has a separate first circuit interface for maximum fault tolerance. Independent SRAM-based receive buffers indexed by FPGA-based registers are used to offload byte-by-byte operations from the DPU software. Data may be received simultaneously from all eight channels. A single memory-mapped transmitter is steered to any of the eight output channels, such that only one channel is actively being commanded at a time. However, all output channels can be selected simultaneously for broadcast messages, such as time distribution.

The local EPU board for each instrument (other than MLA) formats the instrument telemetry packets. The telemetry is copied, byte by byte, into the SRAM buffers in the DPU as the data are received from the payload. Data may be transmitted continuously or in bursts and are instrument specific. The SRAM buffer is operated in a ping-pong fashion, where one set of buffers is receiving data, while the other is made available to the DPU expansion bus for processing by the DPU. Once per second, the DPU switches receive buffers, thus introducing a 1-s latency between when instruments send data and when the DPU forwards them to the spacecraft. The instruments are not allowed to send telemetry during a 300-μs period once per second to accommodate this buffer swap operation. The DPU also sends each instrument a differential one pulse per second (PPS) SYNC signal (also RS-422) to help define this telemetry "quiet time," as well as provide a very good time reference for the instruments to synchronize with the spacecraft 1-PPS clock.

1553 Interface Board. Communication between each DPU and the spacecraft is accomplished through MIL-STD-1553 busses. The 1553 Interface Board is an exact copy of a design used on the CONTOUR CRISP and CFI instruments. The design is based on the UTMC SUMMIT UT69151DXE protocol/transceiver chip and also includes an Actel RT14100A

FPGA and 64 KiB of SRAM. Each DPU is a remote terminal on the spacecraft 1553 bus. All payload commands and telemetry, except MDIS image data, are communicated via the 1553 bus.

The DPU receives a 1553 bus message from the spacecraft once per second containing the time corresponding to the next hardware 1-PPS signal used to synchronize systems on the spacecraft. This message is received at a fixed time before the 1-PPS signal. The DPU transmits this time message to all instruments prior to the arrival of the 1-PPS signal via the UART data links. This approach eliminates the software latency and jitter of processor interrupt response and avoids the latency of UART transmission.

Imager Interface Board. All image acquisition control and hardware image processing occur in the Imager Interface Board. The detailed signal interfaces for this board are shown in Fig. 28. This DPU slice is a modified version of a design used on the CONTOUR CRISP/CFI instruments. It uses two Actel RT54SX72S FPGAs, 2 MiB of SRAM, and a number of LVDS receiver and transmitter circuits to communicate both with the FPUs and the spacecraft high-speed IEM interface card. The Imager Interface Board can control only a single FPU at a time. Camera selection and signal multiplexing occur in the DISE box (see Sect. 3.4.2).

The Imager Interface Board contains two FPGA designs: an imager-interface FPGA and an RTX-bus FPGA. Image data are continuously received from the active FPU and buffered
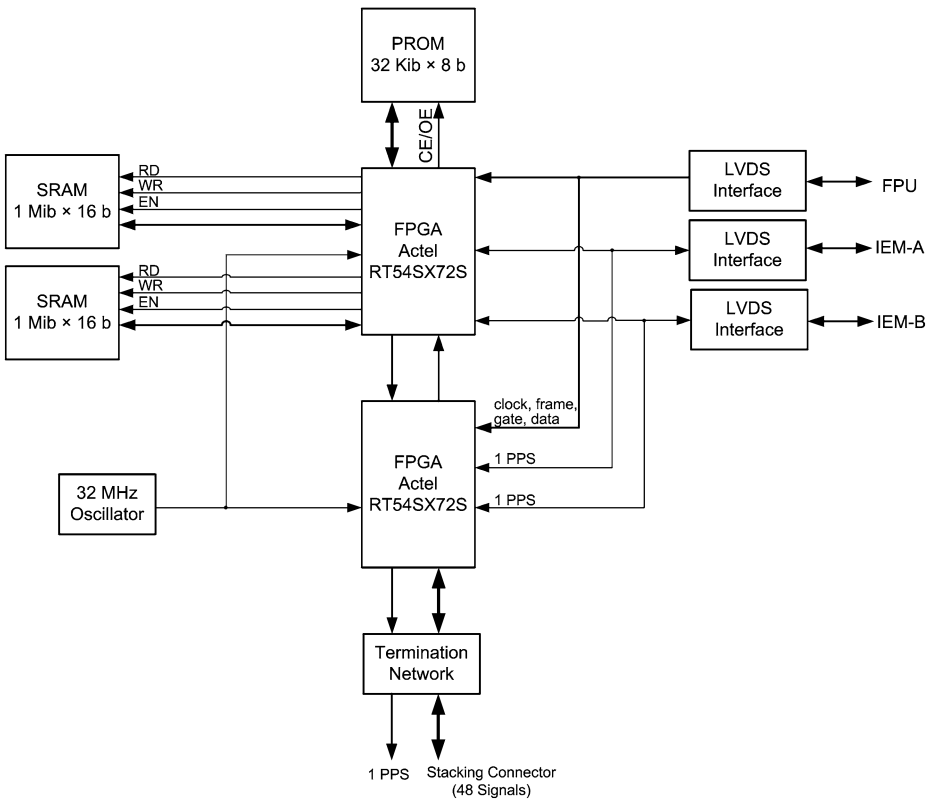

Fig. 28 Block diagram showing detailed signal interfaces for the imager interface board

in SRAM. If the DPU receives a command to record an image, the image data are transferred to either of the two redundant IEMs. The main function of the imager-interface FPGA is to read images from the FPU and send them to the IEM. There are two possible image sizes transmitted from the FPU: 512×512 (CCD on-chip) binned images and $1,024 \times 1,024$ full-frame images. Both formats use 12-bit pixels. A lossy compression method available through eight selectable look-up-tables (Fig. 4) reduces the 12-bit image data to 8 bits. A lossless algorithm, referred to as "Fast" compression, is a second hardware compression mode selectable by the imager-interface FPGA. With the two hardware compression options, a total of eight possible image formats may be sent to the IEM.

The image data read from the focal plane are received from a serial LVDS interface at 16 MHz. A full $1,024 \times 1,024$ image requires approximately 850 ms to be received in the DPU. The data are sent at 4 MHz to the IEM, limiting the image frame rate. Binned images may be sent to the IEM at 1 Hz; however, full-frame images can be sent only at 0.25 Hz. This interface limitation to the IEM requires the imager-interface FPGA to buffer the images in SRAM. The design consists of two main processes: one reads from the FPU and one writes to the IEM. The FPU read and IEM write processes are completely separate, and each has a handshaking signal to indicate that the respective process has completed. A third SRAM control process determines which SRAM is being accessed by which process by monitoring the 1-PPS and handshaking signals from the other processes.

Fast compression takes advantage of the fact that it is not usually necessary to represent a pixel value by the full 12 bits. This technique can be further optimized by recognizing that adjacent pixels often tend to be correlated. By differencing adjacent pixels, with a technique known as differential pulse code modulation (DPCM), fewer bits are required to represent the original pixel value. This technique, implemented in the imager-interface FPGA, permits the maximum number of images to be stored on the SSR without paying the time penalty for a more rigorous compression method. Each Fast-compressed image will be of variable length, and its overall size will be scene dependent. Typically, a higher scene entropy will result in a lower compression ratio.

The main functions of the RTX-bus FPGA are to store a 1,024-bit image header and the FPU command words generated by software running on the RTX processor in the DPU. This FPGA is also capable of generating a 32-bin histogram created from the pixel values produced by the FPU. This histogram is made available to the RTX processor and is integral to the MDIS autoexposure algorithm. The FPGA allows the RTX processor to control the flow of the 1-PPS signal, and it makes the FPU status data available to the RTX processor.

A dedicated memory address on the RTX-bus backplane provides the RTX processor access to the RTX-bus FPGA. Through this interface, the RTX processor can write the 1,024-bit header and FPU control words, read the histogram data, and write the 1-PPS source and output registers. There are three valid sources of the 1-PPS signal. The first two are from each of the IEMs through the LVDS channels. The third is a register in the RTX-bus FPGA to which the RTX processor can write. Another register to which the RTX processor writes determines which 1-PPS source is sent to the FPU and down the DPU backplane.

Imager Power Board.   The MDIS Imager Power Board provides switched +15 V to the NAC and WAC electronics. The board is a modified version of the common LVPS board already described and shares the same in-rush current limiter, EMI and secondary filter, FPGA, and telemetry monitoring design. The supply has only one VPT DVSA2815S DC/DC converter model, which produces a regulated 15-V output. A separate MOSFET-switched output is used for each set of NAC and WAC FPU electronics.

Table 9 Characteristics of the actuators used on MDIS

Characteristic	Pivot actuator	Filter wheel actuator
Manufacturer	Starsys	CDA InterCorp
Primary drive	24 to 35 V	24 to 35 V
Two-phase stepper	yes	yes
Reference frequency	400 Hz	2.5 kHz
Maximum step rate	1.1°/s	75°/s
Electrical resolver	8 speed	1 speed
Motor input step size	5°	30°
Gear system	Hybrid	In-line planetary
Gear reduction	580 : 1	50:1
Output step size	<0.01°	0.6°
Backlash	<0.01°	<0.6°
Mass (actuator + resolver)	916 g	139 g
Redundant windings	yes	no
Range of motion	240°	360°

Motor Controller Board. Each actuator in the MDIS design has a dedicated motor controller board. Although the characteristics of the pivot and filter wheel actuators are different (see Table 9), the board designs are effectively identical. Because most of the low-level motor stepping functions are directly controlled by the DPU processor, the boards are fairly simple. Each board uses an EMI filter, an Actel A1020 FPGA, and a bipolar UDS2998 motor driver to generate the appropriately phased motor drive waveforms. The angular position of each actuator is measured via an AD2S80A motor resolver readout hybrid. The DPU processor generates the motor phase drive timing signals and monitors the shaft position via the DPU I^{2}C bus. Opto-isolators are used to keep the primary power motor drive and control signal grounds separate.

3.3 Software

3.3.1 Common Software

The APL-developed MESSENGER instruments share common software, an instrument domain library. The library was created in 1994 to serve the NEAR instruments. It is currently used in MESSENGER as well as the Compact Reconnaissance Imaging Spectrometers for Mars (CRISM) instrument on the Mars Reconnaissance Orbiter and the LOng Range Reconnaissance Imager (LORRI) and Pluto Energetic Particle Spectrometer Science Investigation (PEPSSI) instruments on New Horizons.

The common software runs as a layer below the application-specific software. The first layer provides standard services, for example, command handling and telemetry packet queuing. Another layer below the service layer is a host abstraction layer. This layer abstracts the input/output (I/O) interfaces used by the instrument to communicate with the spacecraft. The host layer must be customized for each mission given that spacecraft interfaces are not standardized. For the MESSENGER instruments, two different host layers were needed. The MDIS instrument is connected directly to the spacecraft via a 1553 bus. The other instruments use RS422 serial lines to the UART hub board in the MDIS DPU. Software in the DPU acts as an intermediary between the spacecraft and the instrument.

The common software includes a boot program. Its most frequent use is to boot application code by copying it from EEPROM to RAM and then starting the application. However, the boot program also has commands for loading memory from the ground, dumping memory back to the ground, and copying memory to and from EEPROM. These features can be used to upload new instrument programs. The boot program is stored in nonvolatile ROM. In the event that an instrument's program in EEPROM gets corrupted, the boot program will allow the instrument software to be reloaded.

The common software provides command handling and telemetry queuing services. Application-specific software registers command handlers with the common software. Registration provides the command's operation code (opcode), the expected number of arguments, and some code to handle the command. When the common software receives a command from the spacecraft that is properly formatted and has the correct opcode and sufficient arguments, the provided handler code is executed. The common command software can store and run sequences of commands, called macros. Macros can loop and call other macros. Up to 64 macros can be executing at any time. The common software's telemetry service provides formatting and queuing of telemetry packets. The software gathers the packet's data and constructs a Consultative Committee for Space Data Systems (CCSDS) header with the appropriate flags, sequence number, and other information. The packet is queued for transmission to the spacecraft. A 64-KiB buffer allows instrument software to queue large bursts of telemetry that the common software then trickles out to the spacecraft. The common software also includes status/housekeeping packet generation, time management, voltage and current monitoring, and I^2C bus management services.

3.3.2 MDIS-Specific Software

The MDIS-specific software controls the imager hardware, exposure time, and mechanisms. It also serves as a communications hub for the other MESSENGER instruments. Time messages and timing pulses are broadcast to the other instruments. Commands are accepted from the spacecraft and forwarded to the appropriate instrument. Telemetry is collected from each instrument and forwarded to the spacecraft.

Imager Control.   Only one of the MDIS cameras, either the NAC or WAC, can be used at any given time. The MDIS software selects the camera to use based on user command. Images are collected in three stages: expose the image in the FPU, read the image from the FPU to the DPU, and finally transmit it from the DPU to the spacecraft. Different processing steps are applied to the image during each of these stages. The steps include exposure, 2×2 binning, lossy 12 : 8-bit compression, and lossless Fast compression. All of these steps are done in hardware; in fact, the software cannot access the image at all. The software does control the processing, for example, by enabling or disabling the image compression at the correct time based on user commands. The software also manages the three stages of exposure, read, and transmit as a pipeline. In the simplest pipeline, each stage takes 1 s and therefore one image can be taken every second. More complex pipelines result when image binning is disabled (unbinned images take 4 s to be transferred to the spacecraft) or when multisecond exposures are commanded.

Exposure Control.   The exposure time of images can be set manually by command or automatically by the software. In manual mode, the range of available exposure times is nearly 10 s. In automatic mode, the exposure time of the next image is computed by the software. This computation has two distinct steps. The first step computes a new exposure time based
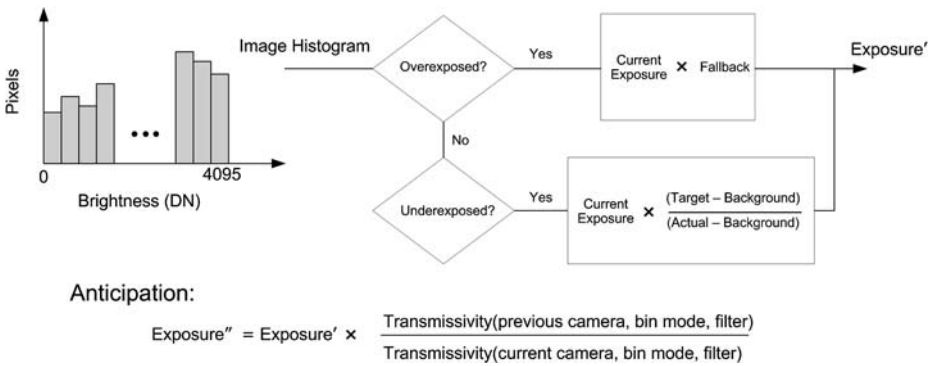
Fig. 29 Autoexposure algorithm decision tree. A 64-bin histogram is computed in hardware for each image. If an image is determined to be underexposed, the actual exposure is computed as Actual = minimum brightness such that the sum of the pixels above this brightness < saturation threshold

on the brightness of a previous image. The second step anticipates filter wheel motions and adjusts the computed exposure time accordingly.

During the read stage of the image pipeline, the hardware generates a histogram of the image. The histogram is analyzed by the software to determine if the image is overexposed or underexposed. First, the histogram is scaled by a factor of four if it comes from a 2×2 binned image. If the brightest histogram value exceeds a specified saturation threshold, the image is considered overexposed and the exposure time is scaled back by a specified fallback factor. Otherwise the image is considered underexposed. Histogram values are accumulated starting from the brightest bin down towards the dimmest bin, until the specified saturation threshold is exceeded. The brightness value that causes the sum to exceed the threshold is defined to be the actual image brightness. The exposure time is scaled by the ratio of the commanded target brightness, to the actual brightness, after a background brightness is removed. The algorithm is characterized by uploadable parameters for the commanded target brightness saturation threshold (the number of allowed saturated pixels), overexposure fallback, and background brightness. The algorithm is depicted in Fig. 29.

The algorithm described so far compensates for changes in scene brightness and filter wheel changes. The next step adjusts the exposure time further if the imager, binning mode, or filter selected for the next exposure does not match what was used in the test exposure. The exposure time is scaled by the ratio of the transmissivity of the old setup to the transmissivity of the new setup. An uploadable table of transmissivities for the WAC filters and for the NAC in either binning mode are used. Finally, the computed exposure time is forced to fall within an uploadable range but is always less than 1 s.

Mechanism Control. The MDIS pivot platform and filter wheel are controlled by stepper motors. The motor controller boards are on an I²C bus, and each motor step must be commanded over this bus. There are also power supply boards on the I²C bus; power switches must be commanded and analog housekeeping read from these boards. The common software provides a mechanism for building and executing an I²C bus schedule. The MDIS software uses this code to construct a four-slot schedule that repeats every 8 ms, i.e., 2 ms per slot. One slot is used to step the pivot platform, another slot is used to step the filter wheel, and the other slots are used to control the power supply boards.

Given the pivot motor gear ratio and the step rate above, the platform can move about 1.1°/s. Similarly, the filter wheel can move 75°/s. Given 12 filters, an adjacent filter can be

reached in 0.4 s and any filter within 2.4 s. Note that the I^2C scheduling method allows the pivot platform and filter wheel to move simultaneously.

3.3.3 Software Metrics

The MDIS software, excluding the boot program, has about 8,000 lines of source code (5,000 lines if only noncommand and nonblank lines are counted). Approximately 60% of this total is shared/reused code in the common software. The compiled application is about 63 KiB.

3.4 Electro-Mechanical Design

The mechanical assembly of MDIS consists of two main components, a bracket assembly that interfaces to the spacecraft and a pivoting platform on which both cameras and the thermal control system are located. One leg of the bracket assembly supports the DISE box and a rotary interface through which all electrical connections to the pivot platform pass. The opposite leg of the bracket supports the precision pivot motor.

3.4.1 Bracket Assembly

The bracket assembly, made of the same advanced composite material (graphite/cyanate ester fabric prepreg) as the MESSENGER spacecraft structure (Leary et al. 2007), was chosen to minimize mechanical stresses due to mismatches in coefficients of thermal expansion. The composite bracket assembly, being a very poor thermal conductor, isolates the pivot platform and thereby the cameras from the payload instrument deck. Eight titanium feet form the mechanical interface to the spacecraft. Four feet were bonded to each stand using a precision fixture, then bolted to the stand. A trim-cut machined from a top layer of epoxy on each composite stand ensured that the pivot axis of rotation was parallel to the spacecraft deck.

Pivot Actuator.   The pivot motor assembly is located on one of the composite stands and is comprised of a stepper motor with a hybrid gear-train and electrical resolver. The stepper motor contains redundant windings so that the two fully redundant DPUs can independently control the motion of the pivot, enhancing the overall reliability of the pivot mechanism.

The total range of motion of MDIS is about 240°, limited by hard mechanical stops in the pivot motor. Pointing knowledge is determined by first "homing" the instrument, which is accomplished by driving the actuator into one of the mechanical hard stops for a period of time sufficient to ensure the orientation of the instrument if it had been previously stopped at the opposite extreme of travel. The rotational speed of the pivot platform is ~1.1°/s, so homing requires about four minutes. Once the location of the pivot actuator is known, the flight software retains this knowledge, and subsequent pointing commands are achieved by counting pulses (steps) to the motor.

The MDIS pivot actuator (Fig. 30) is capable of accurately stepping in intervals of 0.01° (~150 µrad) per step, achieved through a hybrid gear train within the actuator. The 5° stepper motor is coupled to a 5 : 1 in-line planetary gear train, used to drive the wave generator of a harmonic drive. Harmonic drives permit very precise pointing and high torque ratios and weigh less than comparable conventional gear systems. These devices use a radial motion to engage the teeth of a flex spine and a circular-toothed spline, rather than the rotating motion of other gear systems. The harmonic drive in the pivot actuator provides an additional factor
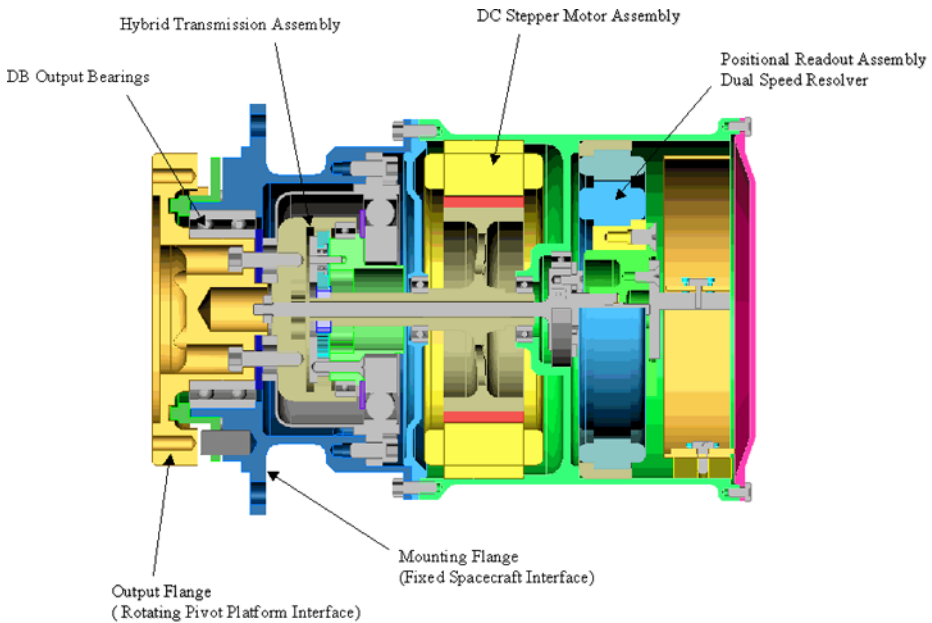
Fig. 30 Schematic view of the pivot actuator, with callouts identifying the hybrid transmission system and duplex pair radial bearings with outer races back-to-back (DB). An in-line planetary gear system drives a harmonic drive, achieving the accurate small-step pointing of MDIS. Individual motor windings are routed to each DPU, making the pivot actuator fully redundant

of 120 : 1 mechanical advantage, resulting in a total gear ratio of about 580 : 1. The hybrid stepper provides for very high gear ratios and near zero-backlash performance resulting in pointing knowledge <75 µrad. The pivot actuator assembly also includes an angular position sensor (electrical resolver). However, because of mechanical distortions in the drive shaft and electrical noise in the device itself, the output resolution of the electrical resolver is worse than a step size.

Protective covers for optical components are very desirable during ground-based testing, launch, and trajectory maneuvers requiring large thruster burns. However, due to mass limitations, conventional protective covers for MDIS were not practical. Instead, the critical first optic of each telescope is protected by rotating the platform 180° from the spacecraft's +Z-body axis such that both cameras look downward into the deck. This innovative approach acts like a reclosable cover and ensures a circuitous path for any particulate or molecular contamination.

Drive Train and Pointing. A challenging requirement on the mechanical design was to limit rotation-plane errors of the pivot platform to <100 µrad. The pivot actuator mounts on a titanium bracket, designed to isolate the platform assembly thermally from the composite bracket stands and not introduce any pointing errors due to thermal gradients from the stands to the platform. In order to minimize the error build up of the large number of mating surfaces making up the drive train of the pivot axis, a significant effort was made to hold very tight mechanical tolerances on all components affecting pointing of the platform. These components include a bearing assembly, a hollow shaft, the pivot platform, the motor shaft, and the pivot actuator. The tightest tolerances were placed on the mating surfaces of
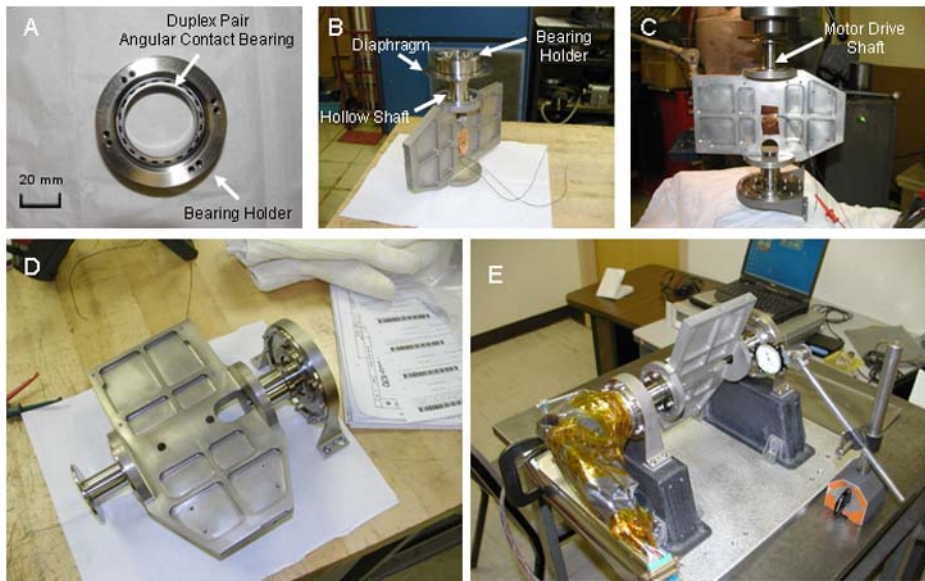
Fig. 31 Sequence of steps resulting in the precision drive train of the MDIS pivot assembly. (**A**) Duplex pair of angular contact bearings pressed into bearing holder. (**B**) Hollow shaft press fitted into the diaphragm and bearing assembly. Shaft then press fitted into platform assembly. (**C**) Motor shaft pressed into platform. (**D**) Completed drive train of platform, prior to integrating onto composite stands. (**E**) Verification of rotational trueness (runout)

these components, and interference fits were chosen to minimize error propagation in the drive train. Once assembled, all mechanical interfaces were drilled and pinned to minimize the chance of a change in the alignment due to thermal variations or vibration during launch.

The titanium bracket opposite the pivot actuator supports a bearing mount, flexible diaphragm, hollow shaft, and electrical feed-through. A duplex pair of angular contact bearings (Fig. 31A) was chosen to support the hollow shaft of the pivot platform. The stainless steel races and ceramic balls of these bearings ensure minimal molecular diffusion between the two surfaces and reduce the risk of "cold welds" that over time could decrease the torque margin of the motor. The angular contact bearings use a dry lubricant, MoS_2, and underwent a run-in period prior to installation. After preliminary cleaning, the bearings were vacuum soaked for 24 hours to eliminate moisture in the MoS_2. The bearings were exercised in a dry-N_2 environment for 10,000 cycles (revolutions) clockwise, followed by 10,000 cycles in the counterclockwise direction.

Installation of the angular contact bearings was accomplished by establishing a clearance of $\sim$12 μm between the outer race of the bearings and the inner diameter of the bearing holder. The bearings were pressed into the titanium bearing holder by heating the holder while keeping the bearings at room temperature (Fig. 31A). The hollow shaft was fabricated to have a line-to-line fit, i.e., zero clearance to within limits of mechanical measurement. Assembly of the hollow shaft required cooling the shaft, then pressing it into the room-temperature bearing and holder. A flexible titanium diaphragm is used to maintain the position of the hollow shaft in the radial direction; the diaphragm is secured to a bracket that mounts to the composite stand. The diaphragm was designed to be sufficiently stiff to support the pivot assembly while remaining flexible in the axial direction, permitting limited

motion resulting from differences in thermal expansion coefficients between the composite spacecraft deck and the magnesium/titanium platform drive train.

Perpendicularity of the mating surfaces on the hollow shaft, motor shaft, and pivot platform were maintained to within machining limits (<25 μm). The interference fits of the shafts with the platform were achieved by heating the magnesium pivot platform before the hollow shaft was pressed into place (Fig. 31B). The rotational orientation of the motor shaft established the final alignment of the pivot platform relative to the spacecraft. Special keying tools ensured proper orientation of the motor shaft prior to it being pressed into the platform (Fig. 31C).

Once the rotating portion of the MDIS instrument was determined to satisfy the pointing requirement in terms of trueness of rotation to within the allowed tolerance, it was necessary to maintain the perpendicularity of the rotation axis to the mounting feet. A high-precision fixture was fabricated to emulate the spacecraft instrument deck. Each composite stand was mounted to the fixture, and the pivot platform assembly was loosely attached to the stands. Using a Coordinate Measurement Machine (CMM), two parallel planes were established relative to the mounting feet. The hardware attaching the motor drive train (bracket/pivot assembly) to the composite stands was slowly tightened. An iterative process of measuring the relative parallelism of each bracket to the mounting feet was performed. The diaphragm bracket measured parallel to the motor stand feet to within 13 μm. The assembly was bagged, and the motor/diaphragm brackets were drilled and pinned to the composite stands. Runout measured at the bearing end of the hollow shaft as shown in Fig. 31D was determined to be <20 μm (0.8 mils), corresponding to a rotational deviation of the pivot plane of motion from normal of <85 μrad.

Twist Capsule.   A stainless steel rotary feed-through (twist capsule) mounts to the bearing holder and passes through the hollow shaft. Set screws position the rotating shaft of the twist capsule inside the hollow shaft. All electrical connections to the platform pass through the 110 conductors of the twist capsule. The angular extent of the twist capsule is $+90°$ to $-220°$ and exceeds that of the pivot motor. The combination of rigid-flex circuitry inside the twist capsule and stainless steel bearings requires extremely low torque to rotate. The connectors for each FPU were assembled after the twist capsule was installed. Most signal connections through the twist capsule are redundant and spliced just before each potted connector. The harness at the fixed end of the twist capsule largely connects to the DISE box with the few exceptions used for spacecraft thermal control and monitoring.

3.4.2 Platform Assembly

Because of mass constraints, mechanical housings were fabricated from magnesium instead of aluminum wherever possible. The pivot platform, the two FPUs, and the filter wheel housing were fabricated from magnesium stock. To minimize the stress on optical components due to thermal contraction, the WAC telescope, filter wheel, and the NAC and WAC light baffles are titanium. The NAC telescope is aluminum with aluminum mirrors. The supporting structure for the radiators and heat pipes is stainless steel, to match the coefficient of thermal expansion (CTE) of the stainless steel heat pipes and to minimize parasitic heat leaks from the radiators to the platform. The radiator panels are made of beryllium, selected for its light weight and high heat capacity. Each beryllium panel is passivated with a thin aluminum layer, which is then clear anodized to optimize its thermal properties.

Fig. 32 Mechanical assembly of WAC filter wheel. Unique design of using an electrical resolver with a spline shaft eliminated the need for an additional bearing or bushing opposite the motor. The unusual shape of the filters reduced the overall size of the assembly
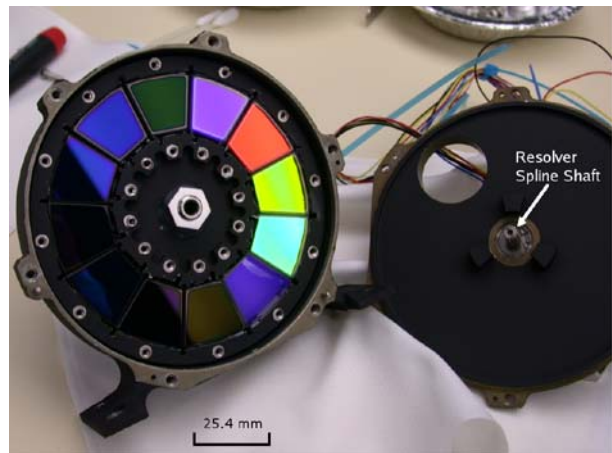
Filter Wheel Assembly. The 12 optical filters were bonded in place using a low-outgassing epoxy. By optimizing the physical shapes of the filters, the overall size and mass of the wheel assembly (Fig. 32) were reduced.

The filter wheel actuator for the WAC consists of a CDA InterCorp DS9-A stepper motor with output step angle of 30°, and an inline gear train with 50 : 1 reduction resulting in an output step size of 0.6°. The step rate is 75°/s, permitting 1-Hz imaging using adjacent filters, provided the exposure is less than 490 ms. The output shaft of the motor has a precision double-D interface to the wheel assembly and an internal spline to accept the shaft of the CDA InterCorp electrical resolver (DT1-A) angular position sensor. The motor mounts to the filter wheel housing, and the resolver mounts to the filter housing cover, eliminating the need for a bearing and providing a simple robust design.

Focal Plane Unit. In addition to mechanically supporting the detector electronics, the mechanical assembly of the FPU was designed to maintain the position of the CCD at the focal plane of the optics over the range of operating temperatures. The complex thermal design (Sect. 3.5) required that the CCDs be thermally isolated from the electronics located in the same housing.

The front panel of the FPU housing is a critical component in each camera, providing the precision mechanical support for the CCD detector and the mechanical interface for each camera's telescope. The NAC front panel was fabricated from aluminum to provide the best match to the physical characteristics of the telescope. The WAC front panel is magnesium. Best focus in each camera was achieved using precision spacers providing a three-point mount of the CCD to the front panel. Each focus spacer is pinned to the front panel to prevent shifting of the CCD during environmental qualification and launch. The focus spacers also thermally isolate the cold detector from the front panel of the FPU. Figures 33A and 33B show the inside surface of the front panel and the three focus spacers supporting the CCD. Epoxy-glass isolators increase the thermal resistance between the CCD heat sink and the front panel. The CCD itself is bonded to an aluminum heat sink with a thermally conductive epoxy. Panel C of Fig. 33 shows the assembled FPU with its electronics folded in place. An internal multilayer insulation (MLI) blanket surrounding the CCD further minimizes radiative coupling between the FPU electronics and the CCD.

Internal surfaces of the optical housing were painted black to minimize scatter. However, because of the small size of the lenses and lens spacers required by the optical prescription
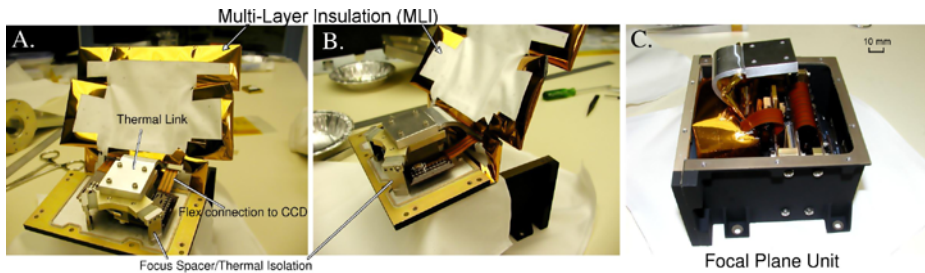
Fig. 33 Detailed integration of the NAC FPU housing. (**A**) Front panel, which supports the CCD on one side and telescope on opposite side. (**B**) Three-point mount provides correct focal position and isolates cold CCD from FPU front panel. Thermal blanket further isolates CCD from FPU electronics. (**C**) Assembled FPU without top panel

in the WAC, painting of these small components was not practical. Instead, the titanium lens spacers used in the WAC were anodized, resulting in a dark dull finish. Because these spacers are not directly in the optical path, the trade between the titanium anodization versus black paint was deemed acceptable.

3.4.3 DPU Assembly

The DPU design was optimized to keep overall mass low, accomplished primarily by using the 102 mm × 102 mm (4″ × 4″) slice architecture first developed on the CONTOUR CRISP and CFI instruments. The slice architecture consists of a simple mechanical frame that supports the printed circuit board. Both sides of the board are accessible for testing, even after assembly into the mechanical frame. The generic slice design provides for multiple configurations of the DPU, which greatly facilitated the common payload elements of MESSENGER.

3.5 Thermo-Mechanical Design

The MESSENGER spacecraft is protected from direct solar illumination by the spacecraft sunshade. Strict rules govern the allowable attitude of the spacecraft in order to ensure that Sun-keep-in limits are not violated. As a result, the thermal environment of the instruments is largely benign with the exception of short intervals during the 12-hour orbital period when Mercury's illuminated surface subtends a large solid angle. The passive thermal design of MDIS uses radiators to cool the instrument, but this radiative cooling system must be disconnected during the short heat impulse that occurs near periapses at Mercury to prevent the instrument from exceeding the CCD's operational high-temperature limit ($-10°C$). This thermal switching is accomplished by means of diode heat pipes. Survival heaters ensure that cold operational limits are not violated.

The DPU is directly coupled to the spacecraft deck and blanketed with MLI. The $-40°C$ to $+50°C$ operating temperature of the DPU follows the deck temperature. The temperatures of the imager interface board and the LVPS board are measured internal to the DPU and reported in the instrument housekeeping data. A number of external spacecraft temperature sensors report the deck temperature at the location of the DPUs and MDIS.

The MDIS temperature sensors are mounted at key locations on the instrument (Fig. 34) and are reported in image headers. The CCD temperature is the most important temperature for calibration (Sect. 4.2.1). The MDIS platform temperature and pivot actuator temperature
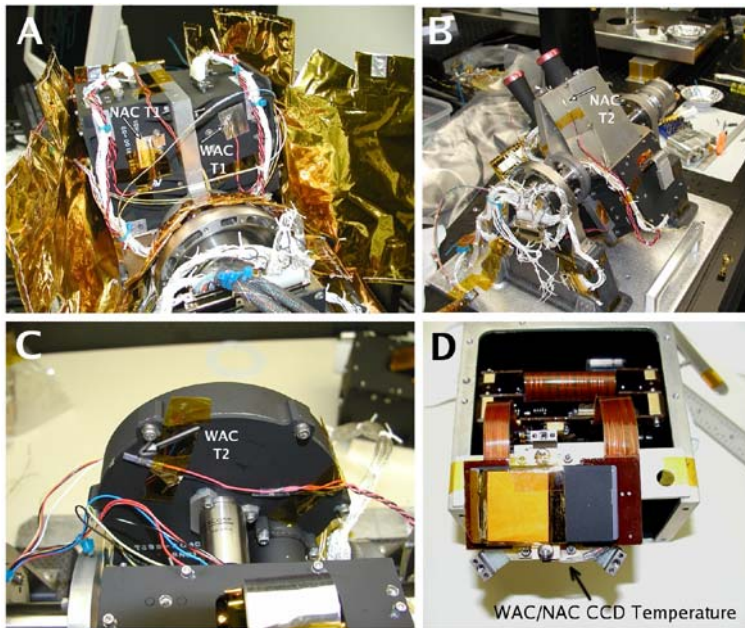
Fig. 34 Location of the MDIS instrument temperature sensors. (**A**) Location of FPU housing temperature, "CAM_T1," for each unit. (**B**) Telescope temperature, "CAM_T2," for the NAC. (**C**) WAC filter wheel housing temperature, "CAM_T2". (**D**) Location of the CCD temperature sensor for each camera

are reported in the spacecraft housekeeping. These measurements are a spacecraft function and are reported independently of the power state of the instrument.

3.5.1 Thermal Design of the MDIS Platform Assembly

Each camera has its own thermal control system, and each CCD is mounted to a heat sink that bolts onto a bracket that is thermally isolated from the FPU. Precision titanium spacers minimize heat conduction from the FPU to the CCD while maintaining focus over the operating temperatures of the instrument. A hole in the front panel of the housing allows light to pass through the assembly and onto the CCD detector, and the surface of the FPU closest to the CCD is unfinished to provide a lower emissivity surface to minimize radiative coupling between the CCD and the front panel (Fig. 34).

The thermal link passes through a hole in the top of the housing and ties the CCD to a phase-change material (PCM or wax pack) mounted to the top of the FPU housing. The wax pack is also thermally isolated from the FPU housing using epoxy-glass standoffs and MLI blankets. A thermal strap, secured to the top of the wax pack using a conductive epoxy, thermally ties the wax pack to the evaporator portion of a stainless steel diode heat pipe. Each camera has its own wax pack and heat pipe assembly. The two heat pipes mount inside the radiator structure, and both pipes connect to each of the three radiator plates (Fig. 35A). Each heat pipe is thermally connected to the inner surface of each of the three beryllium radiator plates with copper saddles. A photograph and schematic of the thermal system are shown in Figs. 35A and 35B, respectively.

Radiator Assembly. The three radiator panels are physically mounted to a stainless steel structure, supported by thin titanium rods to form a spoke-like assembly that minimizes heat
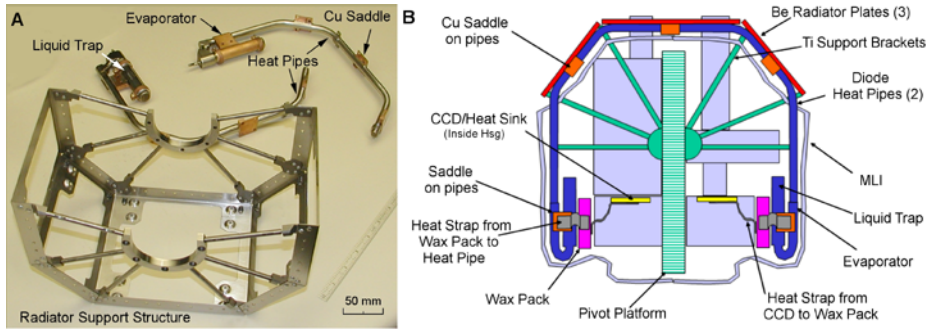
Fig. 35 (**A**) Photograph of the diode heat pipes and radiator support structure. (**B**) Schematic diagram showing key design elements that maintain the MDIS CCDs at nominal operating temperatures. Each CCD (NAC on *left*, WAC on *right*) is thermally coupled to phase-change wax pack that buffers the detector temperature. The wax packs are cooled by the radiator at times when the hot surface of Mercury does not occupy a large part of the radiator FOV. The diode nature of the heat pipes acts as a switch and provides a thermal pathway when the radiator FOV is cold and thermal isolation when it is hot. Hsg denotes housing

conduction from the radiators back to the platform (Fig. 35A). The structure also supports the two diode heat pipes. Copper pads, or saddles, are soldered to the pipe at the location of each radiator panel. The surface flatness of each saddle and radiator panel was controlled to ensure optimum contact area. MLI blankets enclose the entire CCD-to-heat-pipe thermal path, isolating the components from the rest of the instrument.

The three radiator panels are made of beryllium with a total area of about 340 cm^2. Beryllium was chosen for its large specific heat, and the panels were plated with aluminum in order to obtain a finish (clear-anodization) with a low solar absorptivity (α) and high emissivity. The low α was required to protect against overheating of the instrument by direct solar illumination as might occur in the event of a loss of attitude control of the spacecraft, resulting in a tumble.

Diode Heat Pipe Description. The heat pipes, fabricated by Swales Aerospace, are made from 9.5-mm-diameter stainless steel tubing filled with about 5 g of butane. During normal operation, heat flowing from the CCD, and through the wax pack, will be absorbed at the evaporator. Liquid butane is evaporated, and the gaseous butane flows down the center of the tube to be condensed on the cold walls of the condenser. An internal stainless steel wire mesh acts as a wick to transport the liquid from the condenser back to the evaporator, continuing the fluid loop.

A separate pipe, the liquid trap, is attached to the evaporator section that allows the heat pipe to act as a diode, i.e., allowing heat to flow only in one direction. A small tube connects the liquid trap to the evaporator. The diode action occurs when the condenser/radiators become warmer than the evaporator and the butane liquid in the condenser vaporizes. The now gaseous butane flows down the pipe and condenses onto the walls of the relatively cool (−10°C) evaporator and liquid trap. Since there is no wick in the small tube between the liquid trap and the evaporator, the liquid cannot flow out of the trap, back to the evaporator, and up to the condenser for reevaporation. As the radiator plates continue to heat up, more liquid is vaporized and flows down to the liquid trap area. This process, referred to as "burning out the pipe," continues until most of the liquid is located in the liquid trap and no more liquid can flow back up the pipe to the condenser. In this state, the heat pipe is effectively shut off and there is no longer any heat transfer between the evaporator and condenser. Once the

radiators cool back down and the condenser again drops below the evaporator temperature, the heat pipe will start back up and conduct heat like a regular heat pipe.

The heat pipe was made of stainless steel for several reasons. Stainless steel has a very low thermal conductivity and a high melting temperature. When the heat pipes and radiators/condensers are near their predicted maximum temperature (~230°C) due to the heat impulse from the hot surface of the planet, the diode action of the pipe and the poor thermal conductivity of stainless steel permits very little heat to be transferred back down the pipe into the wax pack. Unlike an aluminum heat pipe that could soften at temperatures above 190°C, the mechanical properties of steel ensure that the pipe will retain its integrity above 300°C. Because the heat pipe is a pressure vessel, a leak in the pipe would cause it to cease to function. A final essential element in the selection of materials for the heat pipe was that the thermal interface of the mechanical connections between the beryllium radiator plates and heat pipe condenser had to be maintained up to 230°C. The integrity of this interface was maintained by soldering copper saddles to the stainless steel tube at both the condenser and evaporator ends. The copper saddles bonded in this way were empirically determined to tolerate the thermal stresses and maintain excellent thermal contact over the wide range of temperatures (−77°C to +230°C).

PCM Wax Pack Description. The wax pack is an aluminum enclosure filled with paraffin, which was selected for its melting point of about −10°C. The camera CCDs are required to be maintained between −45°C and −10°C throughout the mission. The bottom of the wax pack has threaded inserts that provide a mounting interface to the CCD thermal link. One side of a thermal strap connects to the top of the wax pack with a thermally conductive epoxy and is overlaid with aluminum tape.

Thermal Strap and Link Description. The thermal link between the CCD and wax pack was designed to carry 1 W of heat with a minimum drop of temperature. The thermal link was made of multiple sheets of thin aluminum foil, to provide the required flexibility and conductivity. Aluminum end blocks were swaged to each end of the foils to allow a mechanical attachment to the CCD interface plate and to the bottom of the wax pack. The mating surfaces on the thermal link end blocks, the CCD interface plate, and the wax pack were polished to provide a good thermal connection.

The thermal strap between the wax pack top and the heat pipe evaporator was created from two copper braids. One end of the braids was bonded into an aluminum end block, and that block was then bonded to the evaporator of the heat pipe. The other end of the braids was left free for permanent attachment to the top of the wax pack with thermally conductive epoxy.

Functional Operation of Thermal Control System. In orbit about Mercury, when the spacecraft is away from the hot planet, the MDIS radiator plates do not see the planet and are exposed only to deep space. In this condition, the radiator plates become very cold (−77°C) and the diode heat pipes operate as normal heat pipes. The gas internal to the pipe moves freely along the length of the pipe, transporting heat from one end to the other and radiating that heat out to space. The heat from the CCD will flow from the CCD through the thermal link, through the wax pack and thermal strap, to the evaporator of the heat pipe. As the liquid in the pipe evaporates, heat flows along the heat pipe to the condensers and finally to the radiator panels. When the paraffin in the wax pack is all frozen, the wax pack, thermal link, and CCD will continue to cool below the freeze point of the paraffin. As the spacecraft starts to approach the planet, the radiator plates begin to absorb heat from the hot planet. When

the temperature of the condenser rises above the temperature of the evaporator, most of the heat-conducting gas in the pipe condenses in the liquid trap. In the burnt-out pipe condition, very few gas molecules are present and the pipe is shut down, effectively disconnecting the condensers and radiator plates from the rest of the thermal path.

With the heat pipe in its diode mode, namely, shut off, the heat that is still flowing from the CCD will now be absorbed into the wax. The paraffin will warm up to its melting point and remain at that temperature until all 240 g of paraffin have melted. The amount of wax was selected so that all the wax would not completely melt during the hours surrounding periapsis. The melting wax clamps the temperature of the CCD at its operating warm-temperature limit ($-10°C$). As the spacecraft moves farther away from the planet, the MDIS radiator and condenser temperatures will fall below the evaporator temperature and allow the heat pipe to operate normally again. With the condenser temperature below the evaporator temperature, heat will flow from wax pack to the radiators and begin refreezing the paraffin. The partially melted wax pack will remain at its melting (freezing) point until all the paraffin solidifies. At that point, the wax pack temperature will continue to drop down to $-45°C$ where heaters and thermostats control the minimum temperature.

Other than the CCD-to-heat-pipe heat path, the majority of the camera components are thermally connected to the main platform. Heaters on the platform prevent the camera optics and FPU electronics from dropping below $-35°C$. There are no radiators associated with the platform. The cameras and platform are isolated from the environment by MLI blankets and will not overheat due to the relatively small amount of heat dissipated in the electronics.

4 Instrument Calibration

Laboratory measurements described in the following sections were used to derive values for the terms of the calibration equation as shown in (2) for both the WAC and NAC. Both instruments measure relative light intensity in engineering units referred to as DNs. The raw engineering units are converted to the physical units of radiance, L (W m^{-2} μm^{-1} sr^{-1}), following the calibration equation:

$$
\begin{aligned}
&L(x, y, f, T, \tau, b) \\
&= \frac{[DN(x, y, f, T, \tau, b, MET) - Dk(x, y, T, \tau, b, MET)]}{Flat(x, y, f, b) * Resp(f, T, b) * \tau} \\
&\quad - \frac{Sm(x, y, \tau, b) - Scat(x, y, f, \tau, b)}{Flat(x, y, f, b) * Resp(f, T, b) * \tau},
\end{aligned}
\tag{2}
$$

where:

$DN(x, y, f, T, \tau, b, MET)$ is the raw DN measured by the pixel in column x, row y, through filter f, at CCD temperature T and exposure time τ, for binning mode b and Mission Elapsed Time MET;

$Dk(x, y, T, \tau, b, MET)$ is the dark level in a given pixel, derived either from the dark strip or estimated from exposure time and CCD temperature;

$Sm(x, y, \tau, b)$ is the scene-dependent frame transfer smear for the pixel;

$Scat(x, y, f, \tau, b)$ is the contribution of scattered light from elsewhere in the scene;

$Flat(x, y, f, b)$ is the nonuniformity or "flat-field" correction at this pixel location;

$Resp(f, T, b)$ is the responsivity relative to the baseline operating temperature; and

τ is the exposure time in milliseconds.

The analysis used to derive each term of the calibration equation is described in the following sections.

4.1 Ground Calibration Facility and Test Results

All calibration tests were performed in the Optical Calibration Facility (OCF) at APL. The OCF consists of large, linked vacuum chambers with a host of support equipment. The largest of these chambers, the instrument chamber, has an internal diameter of 1.3 m and a length of 2 m and permits mounting the instrument on a three-axis motion stage. The motion stage can rotate the instrument in azimuth and elevation through a range limited only by the instrument harness and mounting hardware. Translation is possible over a limited range, but it is sufficient to center the instrument in the collimated beam of the chamber. The interior and ends of the instrument vacuum chamber are surrounded by cold walls, within which an external refrigerator circulates a cooling fluid to reduce the internal temperature to approximately $-40°C$. Most of the calibrations were performed at approximately $-30°C$. However, additional thermal configurations over the range $-34°C$ to $+25°C$ were also performed, to bracket the behavior of the instrument over the range of expected flight conditions. Figure 36 shows a schematic of the OCF test setup. Inside the instrument chamber, there are two sources of calibrated illumination. In one configuration the instrument views a 508-mm diameter integrating sphere through a quartz window. Dark cloth was draped around the window and sphere opening in order to block unwanted external light from entering the instrument optical path. Sphere spectral radiance was calibrated by the manufacturer just prior to the start of instrument calibration, for each configuration of the sphere's four bulbs: two 45-W lamps and two 150-W lamps. One photometer was coupled through a fiber optic to monitor the internal sphere brightness during all calibration runs. Two additional photometers (not shown in Fig. 36) were mounted on the camera and allowed additional monitoring of incident irradiance.

Rotating the azimuthal stage of the OCF 180° enables the instrument to look along a beam tube into an off-axis parabolic collimating mirror, which has a focal length of 1.43 m, operates at $f/7$, and is focused on a grating monochromator. The monochromator may be illuminated by an incandescent lamp with quartz optics. At the input slit, a set of neutral density filters may be used to attenuate the light by known amounts. At the exit slit, a set of long-pass filters is used to remove higher orders (i.e., shorter wavelengths) from the grating. The wavelength can be changed manually or can be set to scan under computer control. The grating may be positioned to zeroeth order, which allows the full incandescent spectrum to be passed.

A MgF_2 window partitions the monochromator from the unit under test, allowing the monochromator to be removed without breaking vacuum so that other sources may be placed at the focus of the collimator. These sources include a point source (pinhole), pinhole array, and test samples illuminated by an incandescent source and viewed off a silver fold mirror.

Four networked computers were used to acquire and monitor the calibration data. Each computer had a specialized set of tasks to perform. The first was dedicated to running most of the OCF instrumentation such as the motion stage, monochromator wavelength adjustment, and filter wheel selection. The second computer served as a frame grabber that communicated directly to the instrument DPU. The operators ran the calibration scripts and monitored the progress of the runs from the third computer. The fourth computer presented real-time images and plots on its screen, allowing monitoring of calibration results during each experiment.
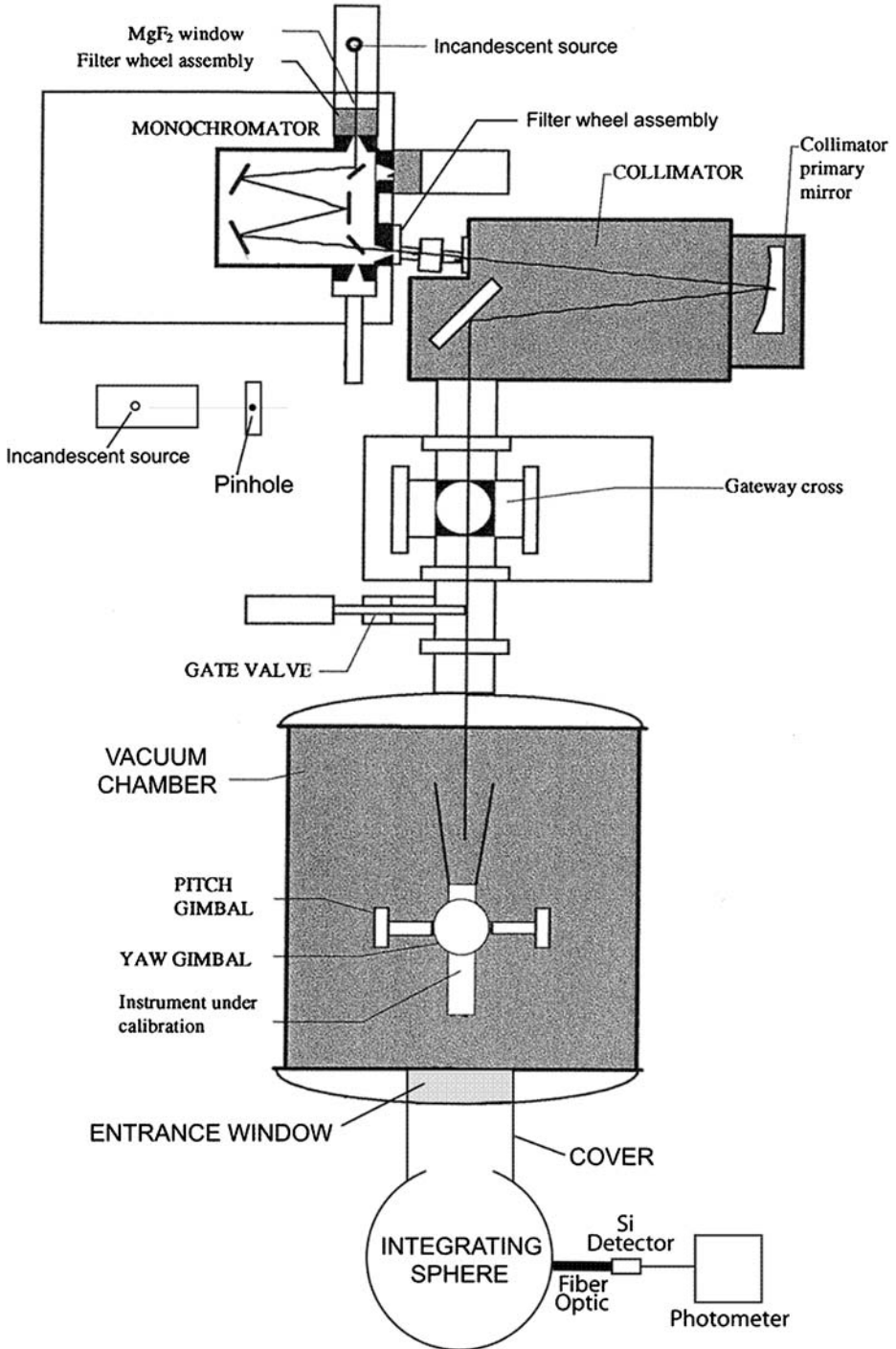
Fig. 36 Optical Calibration Facility hardware configuration used for MDIS calibration

All data were saved locally on disk and were also automatically copied to the remotely located MESSENGER Science Operations Center (SOC) within approximately 30 s of acquisition. The SOC provides a Web interface to the data, organized by test, which includes facilities for searching the database for images in particular configurations. In addition, the SOC processed the image data, performing dark-correction (using the dark strips) and providing a variety of plotting and profiling options. These features were used in near-real time to examine the data for instrumental issues and to validate test results.

4.2 Dark Level

The measured signal from the CCD, in the absence of incident photons, is the sum of three major components: (1) dark current from thermal electrons, (2) an electronic offset, or bias, of ∼240 DN intentionally added to the readout to prevent occurrence of negative values that would appear as zero DN words, and (3) noise picked up by instrument electronics. Throughout calibration there has been no evidence of picked-up noise. In the following discussion, the sum of dark current and bias is treated together as "dark level." The response of pixel-dependent dark level to temperature and exposure time was investigated separately for the NAC and WAC without on-chip binning (full-frame) and with on-chip binning.

4.2.1 Response of the Sensor System to Exposure Time and Temperature

Characterization of the WAC and NAC dark level was conducted over the CCD temperature range 25°C to −40°C, as measured by a temperature sensor (AD590) bonded to the CCD heat-sink mounting plate on each camera (Fig. 34D). This temperature sensor was calibrated during instrument-level thermal-vacuum testing, where it was possible to install multiple thermocouples throughout the MDIS instrument. In particular, a thermocouple located in close proximity to the thermal link on the wax pack of each FPU was used as the best measurement to the actual CCD temperature. A linear regression was used to fit the measured response of the CCD temperature sensor with the calibrated thermocouple response. The other instrument temperature sensors, (also AD590s, see Fig. 34) located on each FPU housing and the WAC filter wheel and NAC telescope, were calibrated in the same way. The final expressions to convert the digital raw output to temperature are

$$T[\deg C] = A \times Raw[DN] + B. \tag{3}$$

The coefficients A and B are listed in Table 10.

Figure 37 shows dark-image means (in DN) for the NAC and WAC full-frame (not binned) and binned images as functions of exposure time and CCD temperature. In the

Table 10 Conversion coefficients from raw DN to °C for internal MDIS temperatures

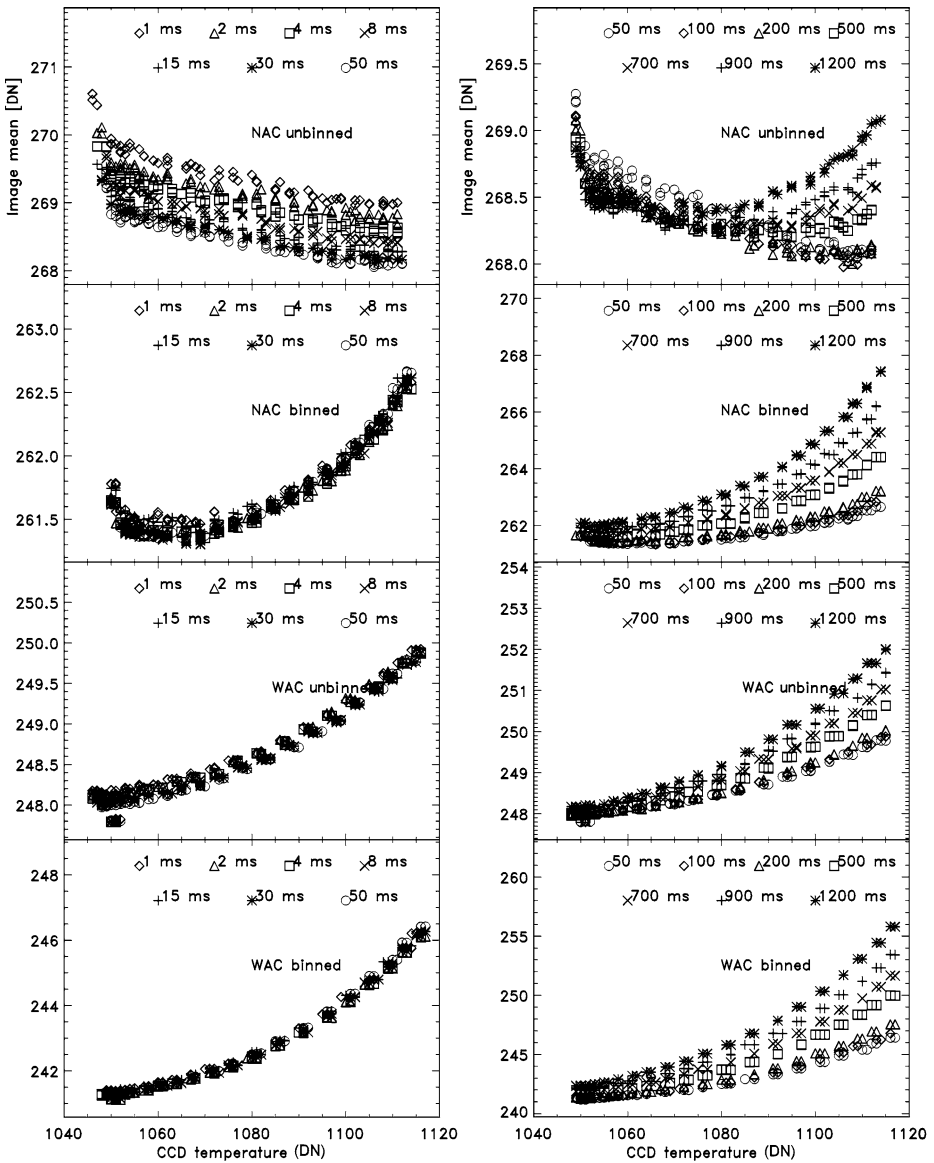| Description	Name	A	B
WAC CCD temperature	ccd_temp	0.2718	−318.455
WAC FPU temperature	cam1_temp	0.5022	−262.258
WAC FW temperature	cam2_temp	0.553	−292.760
NAC CCD temperature	ccd_temp	0.2737	−323.367
NAC FPU temperature	cam1_temp	0.5130	−268.844
NAC FW temperature	cam2_temp	0.4861	−269.718

Fig. 37 Dark image mean as a function of temperature (DN) and exposure time for the WAC and NAC in each binning state

NAC full-frame data, at short exposure times and low temperatures, the dark level is dominated by the electronic bias and the image mean decreases with increasing temperature. This relationship originates in the amplifier in the read-out electronics, which has a temperature-dependent offset (not shown in this figure). After an image has been exposed, large current pulses are sent from the power supply to the clocking signals controlling the movement of charge in the CCD. These high-current clocking pulses increase the overall signal levels for a very short time, as observed in the measured DNs. At longer exposure times (>200 ms) and

higher CCD temperatures ($> -30°C$) the effects of dark current, which increases exponentially with temperature, dominate. The NAC full-frame data show this expected behavior of increasing dark level with increasing temperature and exposure time. Because on-chip binning adds the outputs of four pixels prior to quantization, the impact of the dark current is larger, and the onset of increasing dark level with temperature and exposure time occurs at lower temperature and shorter exposure time. WAC dark levels are dominated by the increase in dark current with higher temperature and longer exposure time.

4.2.2 Dark Models

For the purpose of modeling dark level, the WAC and NAC were treated as four different instruments: NAC full-frame, NAC binned, WAC full-frame, and WAC binned. Two dark models were derived from the OCF calibrations for each of the four modeled sensors: (1) a forward model of the dark level (in DN) as a function of column number, row number, exposure time, and raw CCD temperature; and (2) a backward model that uses the row-dependent dark levels in the dark strips and extrapolates them across the FOV using the same variables as the forward model. For both the forward and backward models, dark level is treated as a linear function of column number, row number, and exposure time. The exponential temperature dependence was approximated with a third-order polynomial for ease of calculation. It is known that the CCD dark level temperature response will change with time due to exposure to radiation in space, and this specific time dependence will be determined in flight over the lifetime of the mission.

Forward Model.   An overview of the forward dark model is illustrated in Fig. 38 depicting the effect of dark level with increasing exposure and temperature. Consider the first of four variables to the dark model: column position x, row position y, exposure time τ, and temperature T. For the column-dependence at a particular row, exposure time, and temperature, dark level is modeled linearly, where an offset $\alpha(y, \tau, T)$ is the value at column $x = 0$ and a slope $\beta(y, \tau, T)$ is the increase per column (per increment of x). Then, to find the dark level at a given column, the model for this row, exposure time, and temperature is:

$$Dk(x, y, \tau, T) = \alpha(y, \tau, T) + \beta(y, \tau, T)x. \tag{4}$$

However, the column-dependence will vary with row, so that in the second level of the model, the offset α and slope β are each functions of row position y. Thus, linear expansions
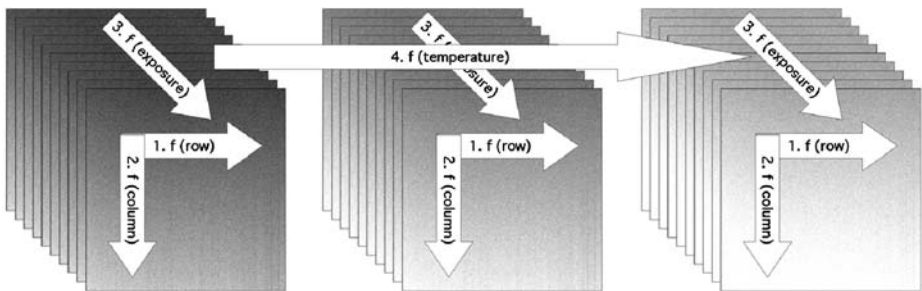

Fig. 38 Schematic representation of dark model calculation decision tree. Each key parameter is identified, and the arrow shows the direction of increase for that parameter. The *gray scale* suggests the effect of dark level in the image as a function of these parameters

of α and β are

$$\alpha(y, \tau, T) = A(\tau, T) + B(\tau, T)y, \tag{5}$$

and

$$\beta(y, \tau, T) = M(\tau, T) + N(\tau, T)y. \tag{6}$$

The offset α to the column-dependent dark level has a value $A(\tau, T)$ in row $y = 0$, and in each subsequent row $y + 1$ that value is incremented by slope $B(\tau, T)$. Similarly, the slope to column-dependent dark level β changes with each row by an offset $M(\tau, T)$ and slope $N(\tau, T)$.

Note that at this level, the row-dependences of column-dependences are themselves dependent on exposure time and temperature. A third level of linear regression can be added to the model, such that $A(\tau, T)$, $B(\tau, T)$, $M(\tau, T)$, and $N(\tau, T)$ can each be expressed as its own linear function of exposure time τ, using a temperature-dependent offset $C(T)$, $O(T)$, $E(T)$, or $Q(T)$, respectively, and a temperature-dependent slope $D(T)$, $P(T)$, $F(T)$, or $S(T)$, respectively:

$$A(\tau, T) = C(T) + D(T)\tau, \tag{7}$$

$$M(\tau, T) = O(T) + P(T)\tau, \tag{8}$$

$$B(\tau, T) = E(T) + F(T)\tau, \tag{9}$$

and

$$N(\tau, T) = Q(T) + S(T)\tau. \tag{10}$$

The expanded dark model at this level becomes

$$Dk(x, y, \tau, T) = C(T) + D(T)\tau + \big[E(T) + F(T)\tau\big]y \\ + \big\{O(T) + P(T)\tau + \big[Q(T) + S(T)\tau\big]y\big\}x. \tag{11}$$

The fourth and final level of the model, $C(T)$, $D(T)$, $E(T)$, $F(T)$, $O(T)$, $P(T)$, $Q(T)$, and $S(T)$, are all third-order functions of temperature, for example,

$$C(T) = H_0 + H_1T + H_2T^2 + H_3T^3. \tag{12}$$

The forward dark level model was derived by first finding a linear fit of dark level as a function of column number for each row in the dark calibration data (2). Second, the bias and dark DN accumulation rate per column increment were fitted linearly as functions of row (3–4). A, B, M, and N were fitted as functions of exposure time, from data binned into 15 CCD temperature bins (each bin 10 DN wide) covering the range 1,000–1150 DN (-40.8°C to -6.8°C) using (5–8). Finally, the linear fit coefficients as functions of exposure time were fitted across the temperature bins with a third-order polynomial (12).

The coefficients of these expansions are given in Table 11a for the four sensor models. After launch these coefficients are serving as the bias for the time dependence of the dark model, with the slopes to be calculated from post-launch observations.

To assess the accuracy of the model, the fitted model was differenced from the data used to create it, and the rms errors between the data and model were measured. Figure 39 shows that, for all four sensor models, over the expected range of temperatures and for exposure times of 1,200 ms or less, the difference between the dark level models and the data used to derive them is comparable to the read noise for each CCD ($\sim$1 DN for the WAC, $\sim$2 DN for the NAC).

Table 11a NAC full-frame dark models

Coefficient	H_0	H_1	H_2	H_3
Forward dark level model				
C	4202.30	-10.7314	0.00974273	-2.94302×10^{-06}
D	-64.4884	0.179181	-0.000165891	5.11765×10^{-08}
E	-2.58253	0.00754599	-7.35219×10^{-06}	2.38873×10^{-09}
F	-0.000464774	1.31009×10^{-06}	-1.23407×10^{-09}	3.88515×10^{-13}
O	0.0143372	-4.21571×10^{-05}	4.12534×10^{-08}	-1.34637×10^{-11}
P	-6.86389×10^{-05}	1.80933×10^{-07}	-1.57409×10^{-10}	4.50925×10^{-14}
Q	-0.000169733	4.92790×10^{-07}	-4.77059×10^{-10}	1.53993×10^{-13}
S	1.35800×10^{-07}	-4.33913×10^{-10}	4.56621×10^{-13}	-1.58643×10^{-16}
Backward dark level model				
C	5451.46	-14.2965	0.0131305	-4.01470×10^{-06}
D	-66.9307	0.185911	-0.000172068	5.30647×10^{-08}
E	-2.42407	0.00705565	-6.84831×10^{-06}	2.21669×10^{-09}
F	0.00526574	-1.44654×10^{-05}	1.32342×10^{-08}	-4.03222×10^{-12}
O	-1.81968	0.00519216	-4.93259×10^{-06}	1.55995×10^{-09}
P	0.00351380	-9.68964×10^{-06}	8.90189×10^{-09}	-2.72453×10^{-12}
Q	-0.000402942	1.21434×10^{-06}	-1.21845×10^{-09}	4.07108×10^{-13}
S	-8.26754×10^{-06}	2.6993×10^{-08}	-2.07595×10^{-11}	6.32380×10^{-15}

Table 11b NAC binned dark models

Coefficient	H_0	H_1	H_2	H_3
Forward dark level model				
C	-5809.80	17.2831	-0.0163855	5.17322×10^{-06}
D	-18.7770	0.0535211	-5.08542×10^{-05}	1.61084×10^{-08}
E	-52.1256	0.148428	-0.00014089	4.45864×10^{-08}
F	-0.00425778	1.22892×10^{-05}	-1.18214×10^{-08}	3.78984×10^{-12}
O	0.676937	-0.00190954	1.79397×10^{-06}	-5.61987×10^{-10}
P	0.00180111	-5.16803×10^{-06}	4.94001×10^{-09}	-1.57305×10^{-12}
Q	-0.00688223	1.94574×10^{-05}	-1.83419×10^{-08}	5.76568×10^{-12}
S	9.00182×10^{-06}	-2.57628×10^{-08}	2.45929×10^{-11}	-7.83098×10^{-15}
Backward dark level model				
C	-8188.55	24.0208	-0.0227352	7.16515×10^{-06}
D	-16.5122	0.0471223	-4.48311×10^{-05}	1.42195×10^{-08}
E	-38.7242	0.110516	-1.05155×10^{-04}	3.33600×10^{-08}
F	-0.0110371	3.13365×10^{-05}	-2.96580×10^{-08}	9.35730×10^{-12}
O	7.69642	-0.0217915	2.05305×10^{-05}	-6.43961×10^{-09}
P	-0.00486634	1.36687×10^{-05}	-1.27902×10^{-08}	3.98703×10^{-12}
Q	-0.0463603	0.000131138	-1.23619×10^{-07}	3.88354×10^{-11}
S	2.89199×10^{-05}	-8.17259×10^{-08}	7.69996×10^{-11}	-2.41893×10^{-14}

Table 11c WAC full-frame dark models

Coefficient	H_0	H_1	H_2	H_3
Forward dark level model				
C	1238.24	-2.76843	0.00256473	-7.86953×10^{-07}
D	-3.48338	0.0101166	-9.79576×10^{-06}	3.16249×10^{-09}
E	-2.42999	0.00714405	-7.00585×10^{-06}	2.29185×10^{-09}
F	-0.00053432	1.49958×10^{-06}	-1.40025×10^{-09}	4.34984×10^{-13}
O	0.0206338	-6.29517×10^{-05}	6.39338×10^{-08}	-2.16318×10^{-11}
P	-0.00033310	9.70986×10^{-07}	-9.43818×10^{-10}	3.05943×10^{-13}
Q	0.000517513	-1.51006×10^{-06}	1.46957×10^{-09}	-4.77044×10^{-13}
S	1.17016×10^{-07}	-3.34717×10^{-10}	3.19031×10^{-13}	-1.01330×10^{-16}
Backward dark level model				
C	-3182.94	9.81730	-0.00936597	2.97916×10^{-06}
D	12.7966	-0.0364940	3.46355×10^{05}	-1.09384×10^{-08}
E	11.4352	-0.0325653	3.08604×10^{-05}	-9.73046×10^{-09}
F	-0.0755373	0.000216107	-2.05838×10^{-07}	6.52700×10^{-11}
O	1.26711	-0.00353596	3.28770×10^{-06}	-1.01873×10^{-09}
P	0.00127217	-3.57421×10^{-06}	3.33658×10^{-09}	-1.03455×10^{-12}
Q	0.000637356	-1.79417×10^{-06}	1.67841×10^{-09}	-5.21619×10^{-13}
S	-2.32720×10^{-06}	6.63236×10^{-09}	-6.28992×10^{-12}	1.98479×10^{-15}

Table 11d WAC binned dark models

| Coefficient	H_0	H_1	H_2	H_3
Forward dark level model				
C	-484.568	2.11771	-0.00206813	6.75547×10^{-07}
D	-10.2411	0.0299233	-2.91567×10^{-05}	9.47476×10^{-09}
E	-27.9169	0.0813578	-7.90653×10^{-05}	2.56248×10^{-08}
F	0.000646762	-1.91510×10^{-06}	1.89122×10^{-09}	-6.22884×10^{-13}
O	-0.550564	0.00152559	-1.40630×10^{-06}	4.30355×10^{-10}
P	-0.00201059	5.92984×10^{-06}	-5.83228×10^{-09}	1.91308×10^{-12}
Q	0.0127947	-3.69327×10^{-05}	3.55415×10^{-08}	-1.14037×10^{-11}
S	-1.54738×10^{-06}	4.29029×10^{-09}	-3.95289×10^{-12}	1.20989×10^{-15}
Backward dark level model				
C	876.088	-1.72949	0.00155692	-4.62411×10^{-07}
D	-8.67913	0.0253792	-2.47483×10^{-05}	8.04835×10^{-09}
E	-24.2259	0.0705204	-6.84466×10^{-05}	2.21526×10^{-08}
F	-0.00286560	8.40352×10^{-06}	-8.21840×10^{-09}	2.68055×10^{-12}
O	-4.55575	0.0128502	-1.20770×10^{-05}	3.78006×10^{-09}
P	-0.00660749	1.93028×10^{-05}	-1.88063×10^{-08}	6.11108×10^{-12}
Q	0.00192523	-5.01882×10^{-06}	4.27240×10^{-09}	-1.17912×10^{-12}
S	8.80210×10^{-06}	-2.61144×10^{-08}	2.58360×10^{-11}	-8.52398×10^{-15}
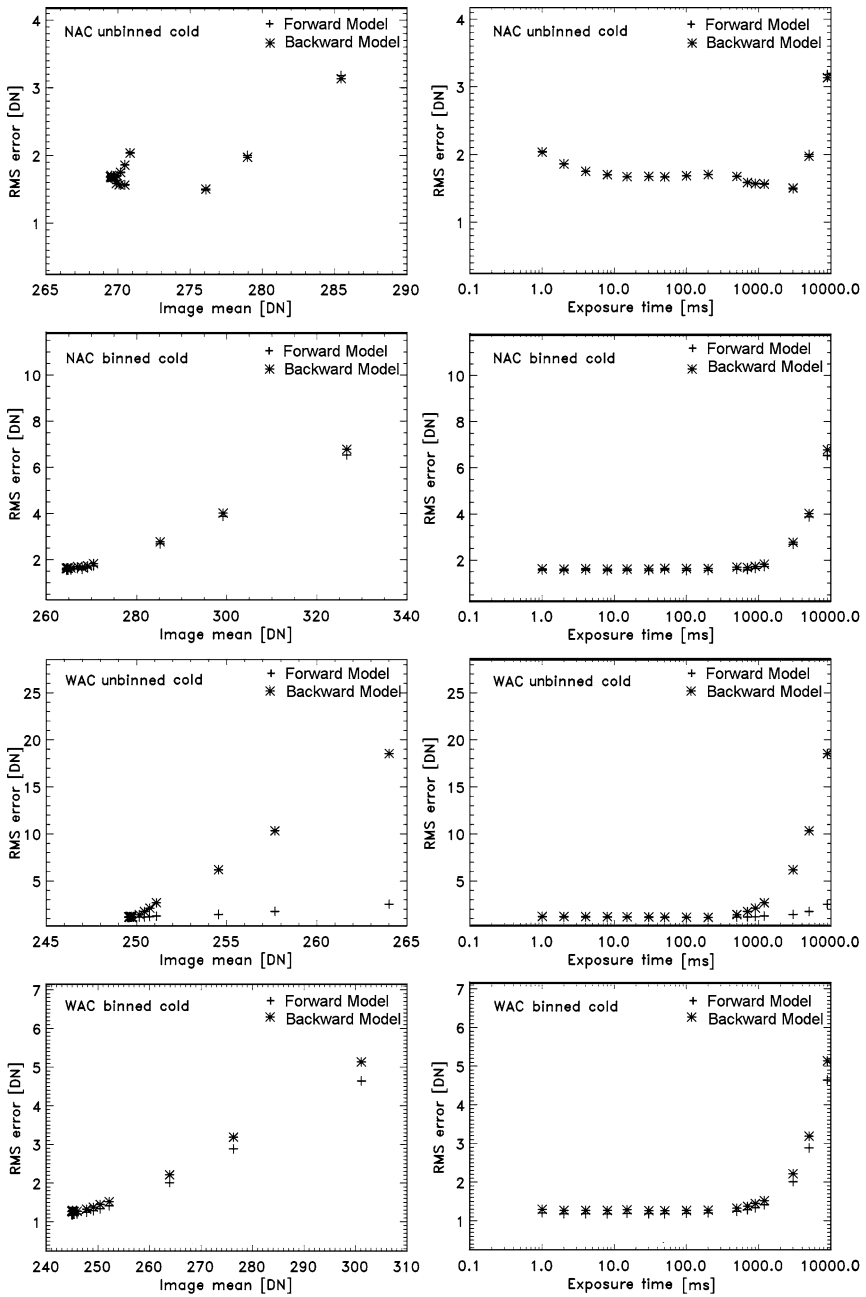
Fig. 39 RMS error of the dark models to image pixels as a function of dark image mean and exposure time for the NAC and WAC, binned and not binned, from OCF calibration data

Backward Model. In the full-frame mode for either the WAC or NAC, the four dark columns behave identically to the scene as a function of row, exposure time, and temperature to within 0.26 DN. A second method to derive the dark level from the image data is referred to as the Backward Model and uses the dark columns and a fitting procedure to determine the dark level similar to that for the dark Forward Model.

In the binned mode for both cameras, true dark columns are unavailable due to an incorrect mapping of these columns in firmware. However, the second column of a binned image provides a lower response than a column in the active image area. This lower-response column does show a temperature- and exposure-time response that can be modeled, making it a functional "dark column." Therefore, the Backward Model simply uses the second column of an image (binned or full-frame) to be representative of the dark strip properties.

The same fitting procedure used to derive the dark level for the Forward Model was used for the Backward Model with the following exception. The bias for the fit to each row as a function of column number was defined to be the value of the fit to the dark column at that row number. Then, the regression error for a range of accumulation rates assuming this fixed bias was calculated. The accumulation rate minimizing the regression error was used as the accumulation rate of each row as a function of column number. From this set of coefficients (Table 11a), the exposure time dependence and the temperature bins were derived and, as above, the rms error of fit regressions calculated. Since the bias derived from the dark columns is not the same as the bias derived directly from the dark frames, it is expected that rms errors will be slightly greater. For exposure times of less than 1,200 ms, the rms error for the dark level derived from dark column Backward Model is, on average, larger than the dark level derived from the Forward Model. Figure 39 compares the rms errors resulting from these two models. The large disparity between the Forward and Backward models at long exposures in the full-frame WAC is a consequence of a poor fit to the Backward Model at long exposures.

Given the initial better fit of the dark level Forward Model to the data, as well as the nature of the binned "dark" columns, it is tempting to rely on the Forward Model exclusively. However, the dark strips, even for binned data, serve as an indicator of the variations of each CCD's response to radiation and, as such, a means to calibrate the changes in the behavior of the CCD with time. Thus, both dark models will be periodically reevaluated en route to Mercury and during the orbital phase of the mission.

4.3 Frame Transfer Smear

Frame transfer smear corrections for MDIS follow the technique described by Murchie et al. (1999) for the NEAR MSI imager. In brief, an image is exposed for a nominal integration time and is then transferred to the memory zone of the CCD, from which the analog signal is digitized line by line. Accumulation of signal continues during the finite duration of frame transfer, inducing a streak or frame-transfer smear in the wake of an illuminated object in the field of view, parallel to the direction of frame transfer, provided pointing remains stable to the end of the frame transfer period. Quantitatively, the smear correction is:

$$Sm(x, y, T, \tau, f, b)$$
$$= \sum_{1}^{y-1} \frac{t_2}{\tau} \frac{[DN(x, y, \tau, b) - Dk(x, y, T, \tau, b, MET)] - Sm(x, y, b, \tau)}{Flat(x, y, b, f)}, \quad (13)$$

where $Sm(x, y, T, \tau, f, b)$ is the smear in column x and row y at exposure time τ and temperature T in binning mode b and filter f. $Dk(x, y, T, \tau, b, MET)$ is the dark level in column

MDIS EW0031478009E Earth Flyby Short Exposure (1 ms)

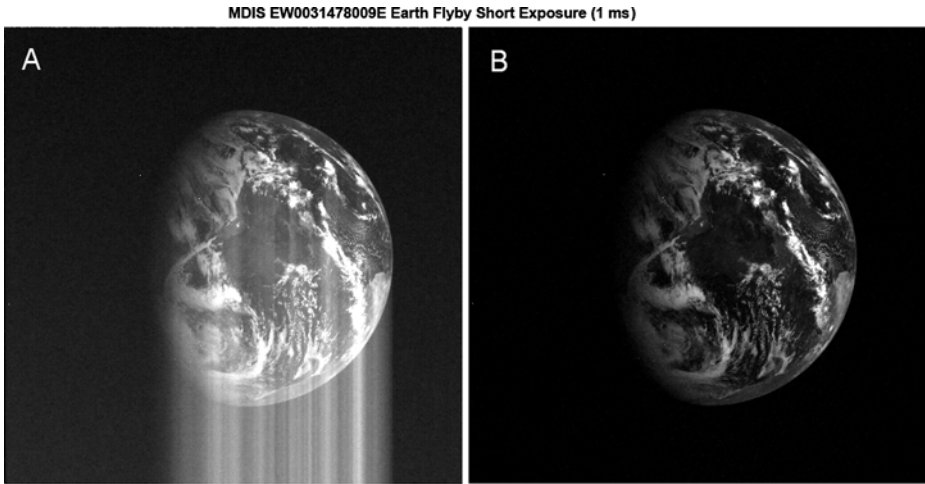**Fig. 40** (**A**) Frame-transfer smear is apparent in this unbinned NAC short-exposure (1-ms) image of Earth during the MESSENGER Earth flyby in August 2005. (**B**) Image after processing with desmear algorithm

x and row y at exposure time τ and temperature T in binning mode b at mission-elapsed time MET. $Flat(x, y, b, f)$ is the flat-field correction in column x and row y in binning mode b and filter f. τ is exposure time, and t_2 is the time for frame transfer (3.84 ms) divided by the number of lines in the image in the direction of frame transfer, i.e., 1,024 for full-frame images or 512 for binned images. Empirically, it was found that this correction removes frame transfer smear to the level of noise in typical, field-filling scenes for which exposure time is >2 times the frame transfer time. For high-contrast scenes such as well-exposed, non-field-filling extended sources imaged against a black background, artifacts are at or below the noise when exposure time is >3 times the frame transfer time.

Figure 40 (left) shows an example of frame transfer smear for a full-frame NAC image acquired during MESSENGER Earth flyby in August 2005. The image was exposed for 1 ms, less than the guideline, but taken to test the effectiveness of the desmear algorithm. In the corrected image (Fig. 40, right), although the smear is slightly overcorrected, the visual appearance of the corrected image is dramatic. The overcorrected artifact disappears in typical scenes for exposure times ≥8 ms. Thus, for analysis of MDIS filter passbands (Sect. 4.5) and radiometry (Sect. 4.6), only images with exposure times ≥8 ms were used.

4.4 Geometric Calibration

4.4.1 NAC and WAC FOV, IFOV, and Offset

To determine the fields-of-view and the relative alignment of the WAC and NAC, the output slit of the OCF monochromator was imaged using white light at different positions of the motion stage. The ends of the slit were measured from dark-corrected, desmeared images, and the pixel positions and stage positions were used to determine the IFOV, FOV, and relative pointing of each camera (Fig. 41). The angular difference per pixel position defines the IFOV, and 1,024 times that value defines the FOV. The WAC FOV is 10.54° ± 0.02°, and the IFOV is 179.6 ± 0.3 μrad. For a 14-μm pixel pitch (specified by the manufacturer), these figures imply a focal length of 77.96 ± 0.15 mm. The NAC FOV is 1.493° ± 0.001°, and the IFOV is 25.44 ± 0.02 μrad, implying a focal length of 550.3 ± 0.5 mm.
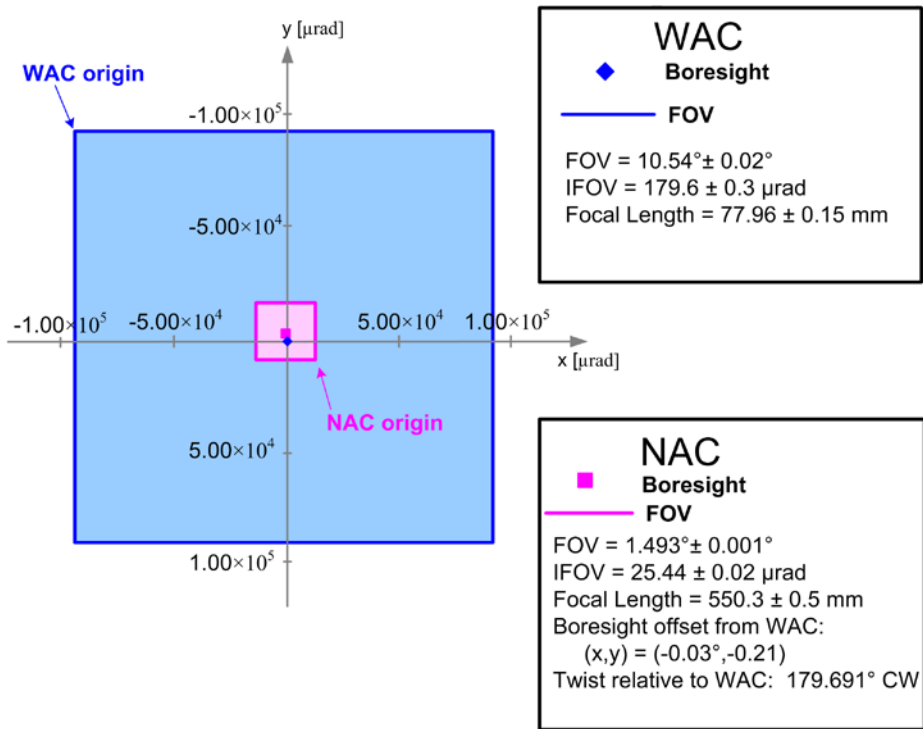
Fig. 41 WAC and NAC fields of view as determined from the ground calibration. Note that the WAC and NAC are rotated about 180° relative to one another. Scale, offset, and relative twist of NAC and WAC images are given in the inset

This measurement also provides information on the relative orientations of the two FOVs. The pixel positions measured at each stage position define a vector for each camera whose angular separation defines the twist between the two FOVs. The NAC FOV is rotated relative to the WAC's by approximately 179.69° clockwise (CW), so that a scene appears "right-side up" in one camera and "upside down" in the other. Allowing for this twist, solving for the center pixel position in each camera in angular coordinates, and differencing the two results yields the offset in boresight positions. The two boresights are offset by 0.21°.

4.4.2 Position within Pivot Plane

Through mechanical tolerances, deviation of the pivot plane from normal due to mechanical error is less than 85 μrad. Sampled measurements over the range of motion of the actuator are consistent with the nominal stepping of 0.01°/step. We attempted to characterize fully the single-step response of the pivot actuator but found systematic effects dominating the measured response.

The flight software does not routinely command the pivot actuator to the operational hard stop, but halts motion at a software stop located at +50°. To establish a second known position within the ~240° range of motion of the pivot, detailed alignment measurements were conducted during spacecraft-level tests. These measurements were repeated at the NASA Goddard Space Flight Center facility after thermal-vacuum testing and just prior to the final close-out of the spacecraft at Astrotech in Florida. The technique employed multiple

Fig. 42 Final ground-based
coalignment measurement
between WAC, NAC, and
spacecraft. (**A**) Configuration of
spacecraft on test fixture,
showing theodolite in
foreground. (**B**) Close-up of
MDIS orientation with WAC on
left and NAC on right. (**C**) WAC
image and correct orientation
relative to geometry shown
in (**A**). Note cruciform projected
into theodolite gives a particular
pixel, mapped into the spacecraft
frame. (**D**) NAC image, acquired
by shining a bright white light on
subject located behind theodolite.
The reticule of the theodolite
provides the vector mapped into
the spacecraft frame
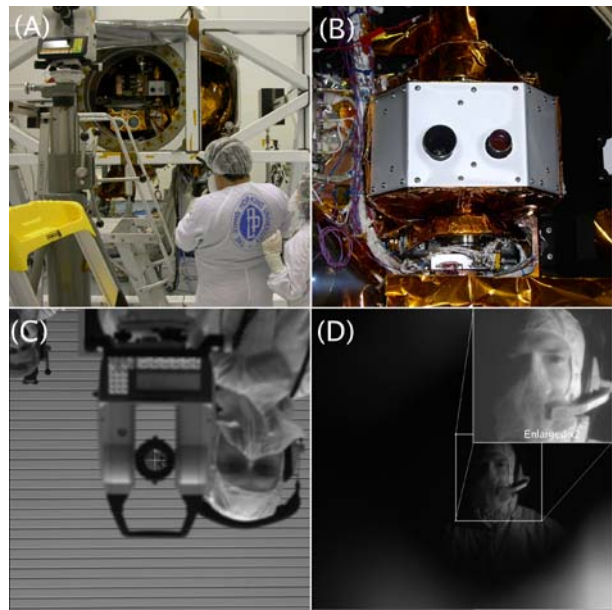
theodolites to reference the spacecraft master alignment cube and map the MDIS alignment
cube and boresights at a given pivot position into the spacecraft system. After commanding
the pivot to the 0 position of the actuator (apertures directed along spacecraft $+Z$-axis),
a reference flat was placed on the nonflight protective cover of the WAC. The theodolite was
autocollimated to this mirror, ensuring that the projected beam from the theodolite would
at least fall in the WAC FOV. The coordinates at this setting were recorded, and without
touching the spacecraft structure the red-tag cover was removed from the WAC. Several im-
ages were snapped by the WAC mapping a known field location in the WAC image into the
spacecraft coordinate system.

A similar procedure was done with the NAC, but because of the bandpass filter on the
NAC the green light of the theodolite could not be passed through the optical system of
the NAC. Instead, after autocollimating from a reference flat on the NAC red-tag cover and
recording the measurements in the spacecraft frame, a bright white light source was placed at
the eye-piece of the theodolite. After passing through the theodolite, the light was collimated
and successfully imaged in the NAC. Further, it was possible to identify the reticule on the
theodolite that was coaligned with the cruciform, which was autocollimated on the reference
mirror on the NAC before removing it. Figure 42 shows these two images. Note the WAC
image is rotated 180° relative to the NAC.

4.5 Wavelength Calibration

The NAC uses a single filter, while the WAC views the scene through a filter wheel outfit-
ted with 12 filters of varying widths. The WAC filters are labeled by their position counter-
clockwise around the wheel as viewed from the CCD. Using the OCF monochromator, NAC
and WAC filter transmissions were measured as functions of wavelength for CCD tempera-
tures ranging from -35°C to ~ 26°C. The source appeared in the data as a bright rectangle
in the center of each image. After subtracting the dark model from the image values and
performing smear corrections, a mask was derived from each image based on bright and

dark pixel distributions. The values in the mask were set to zero for the dark regions and one for the source rectangle. After multiplication, the pixel values for the resulting image were summed to achieve maximum response with varying source wavelength. A Gaussian shape was used to model most of the WAC and NAC filter centers and widths, except for WAC filters 6 (430 nm) and 11 (1,010 nm), which were modeled with a combination of Gaussian and polynomial fits. The center wavelength and FWHM passbands were calculated for filters 6 and 11 through a cumulative distribution technique, which is similar to a weighted average. Specifically, after normalization, the data were summed as

$$C(\lambda_n) = \sum_{i=0}^{n} F(\lambda_i), \qquad (14)$$

where $C(\lambda_n)$ is the cumulative distribution to λ_n, $F(\lambda_i)$ is the filter response at wavelength λ_i, and n varies between 0 and M, the number of monochromator wavelength settings within the filter passband. The 50% point of the cumulative distribution was defined as the center wavelength of those two filters, and the 75% and 25% points were differenced to find the filter width.

Figure 43 shows fits calculated to WAC data acquired in the OCF at a CCD temperature of $-26°C$, which is about the median operating temperature expected in Mercury orbit. These compare well with the manufacturer-measured passbands (Table 6). Filter 2 is a clear fused silica filter spanning the entire passband of the CCD (395–1,040 nm) and is not shown here. The NAC filter was measured to have a center frequency of 751 nm and a passband of 88 nm.

The center wavelengths shift systematically with temperature of the filter. However, with the exception of the longest wavelength WAC filter (#11), in which the passband is affected by a temperature dependence of the response of the CCD itself, they agree with the nominal values to within 2 nm. Figure 44 shows the difference in filter nominal center wavelengths between room temperature and a CCD temperature of $-26°C$. The scatter in the wavelength offsets at the lower temperature ($-35°C$) should be considered as a measure of the precision of determining the center wavelength (±0.5 nm). All filters show the expected shift to longer wavelengths with increasing temperature. Filter 11 has a greater shift than the rest of

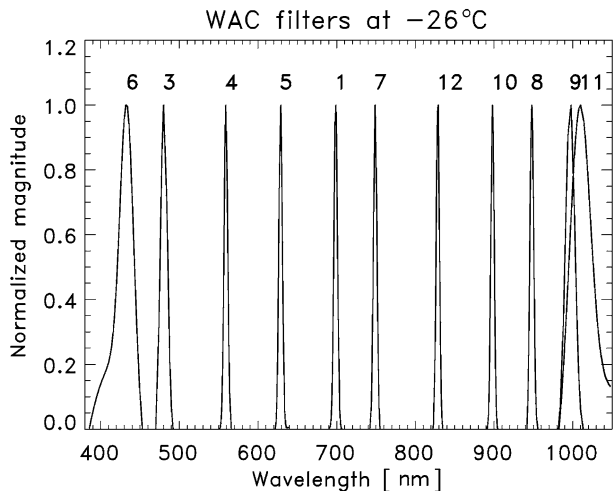**Fig. 43** WAC filter centers and passbands at $-26°C$

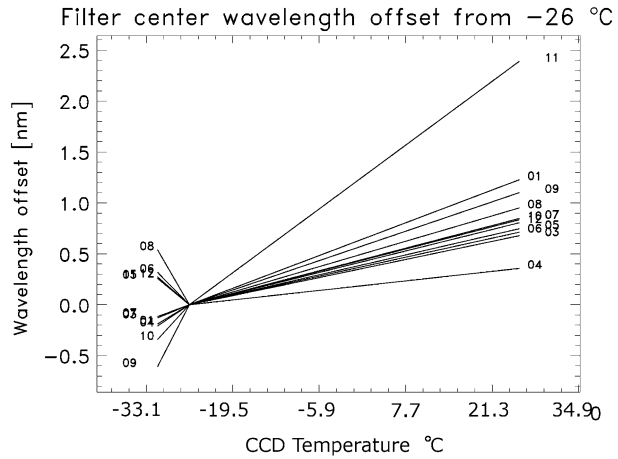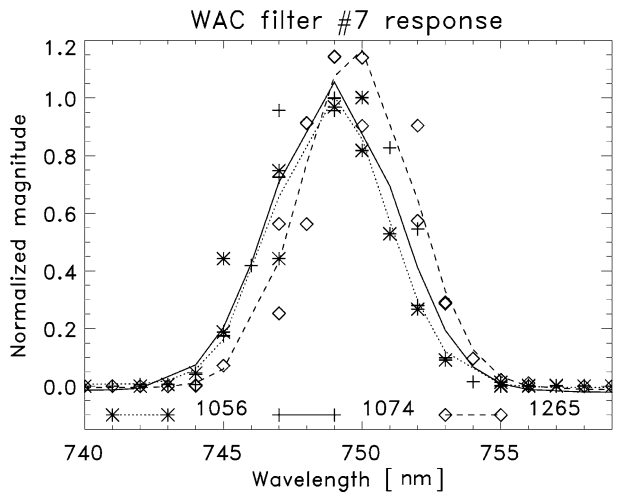**Fig. 44** Offset in WAC filter center relative to position at −26°C, as a function of temperature

Filter center wavelength offset from −26 °C

Fig. 45 Shift in WAC filter 7 (750 nm) passband between −31°C. Symbol labels give temperature in DN and room temperature

WAC filter #7 response

the filters, due to enhanced long-wavelength response of the CCD at higher temperatures. Figure 45 shows fitted measurements for an example passband, the WAC 750-nm filter (#7), and how the passband shifts with temperature.

4.6 Responsivity, Response Linearity, and Response Uniformity

Calibration of the signal accumulation rate per unit time per unit radiance at the sensor was conducted in the OCF for the WAC and the NAC over a broad range of exposure times and source light intensities. The exposure times to saturation were determined empirically in the initial set-up. Using a variety of temperatures (−34°C to 25°C) and source intensities, images were acquired after varying the exposure times until saturation occurred. Source intensities were stepped in a fixed decreasing-light pattern through the eight levels that could be achieved with the integrating sphere's two 150-W and two 45-W bulbs. The bulbs required about 20 minutes of warm-up before asymptotically approaching constant light output. The WAC calibration procedure began with all lamps on then subsequently turned lamps off in

sequence. The exposure sequence was repeated for each filter for the WAC, but only a single exposure sequence was required for the single filter of the NAC.

With MDIS mounted in the OCF vacuum chamber with the integrating sphere set back from the door looking into the window of the door, the sphere did not fill the FOV of the WAC. It was not possible to acquire field-filling sphere measurements in vacuum and at cold temperatures. However, room-temperature, ambient-pressure measurements were acquired with the chamber door open and the sphere moved forward close to the instrument, filling the FOV.

4.6.1 Response Linearity

The relationship between the raw DN output from the camera per unit exposure time and radiance, as a function of variation in exposure time or radiance, is referred to as response linearity. Using dark-corrected, desmeared DN image (DCDSI) values taken from the center quarter of the images, response linearity was measured with both the NAC and WAC binned and full-frame. Linearity was first examined separately at room temperature and cold for (a) linearity with respect to exposure time at individual light levels, and (b) linearity with respect to radiance at individual exposure times. To first order, the results are not significantly different, so all data were merged to examine linearity with respect to measured photons (the product of radiance and exposure time). However, it was found that each detector departs from linearity at low signal levels. Nonlinearity only appears to be correlated with a specific CCD (WAC or NAC), and not correlated with either binning state or detector temperature. For each (WAC and NAC) filter, the responsivity was normalized to unity at a reference dark-corrected, desmeared DN level of 1,500. Responsivity of each detector was found to correlate with the background subtracted DN level in a linear-log relationship, as shown in Figs. 46 and 47 for the WAC and NAC, respectively.

The measurements were taken using a calibrated integrating sphere, and a matrix of exposure times and brightness levels. The clustering of the data in Figs. 46 and 47 shows that there is no difference in system responsivity at a given signal level, whether that signal level is achieved by differences in exposure times or by changes in scene brightness.

Fig. 46 WAC linearity response shows no distinction between short exposure and brightness variation. These data were acquired over all filters and a variety of exposures and brightnesses
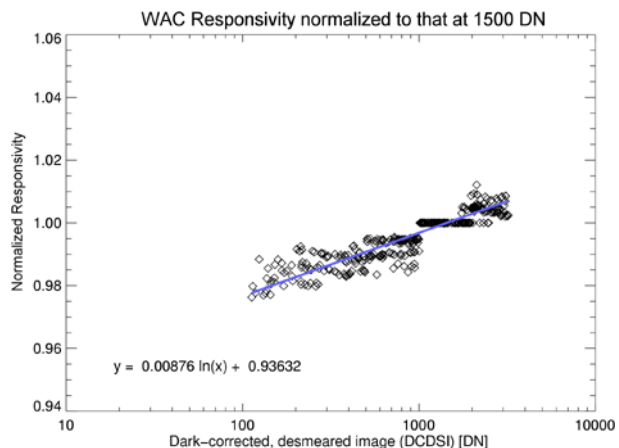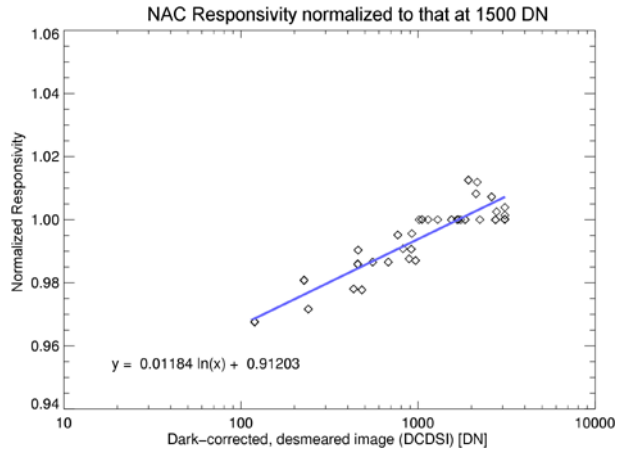
Fig. 47 NAC linearity response, although different from WAC, shows no systematic difference between varying exposure, brightness level, or temperature

4.6.2 Responsivity

Responsivity is the dark-corrected, desmeared DN per unit time per unit radiance at the reference DN. Integrating-sphere radiances were calibrated by Labsphere using each of the four lamps separately, over a wavelength range of 350–1,100 nm in 5-nm steps. To determine radiances through each of the WAC and NAC filters, the band passes described in Sect. 4.5 were convolved with the sphere's spectral radiance. For data taken at room temperatures, the chamber door was open, but for lower-temperature measurements the sphere was viewed through the quartz window in the OCF chamber door. Therefore, for the low-temperature data an additional correction was applied to the sphere radiance for each filter to account for the window. This correction was derived from room-temperature data, as the ratio of corrected DNs per unit time with the door closed to that with the door open, for a single configuration of sphere bulbs.

Figures 48, 49, and 50 show the responsivities measured for each filter for the full-frame WAC at a range of radiances and exposures, for three different temperatures. Data points are represented by crosses, which have widths showing 2-σ errors of the dark model and heights showing 2-σ errors in responsivity. Each line connects the responsivities measured at a single sphere radiance at different exposure times. For each filter, the data overlay to within the errors in the dark model. Table 12 gives the actual responsivities for the NAC and WAC. Figure 51 shows the temperature dependence of the full-frame WAC responsivities for each filter, normalized to the CCD temperature of $-30.25°C$. For these data, differences between $-30°C$ and $-34°C$ at wavelengths <700 nm are assumed to be a measure of systematic errors. No significant temperature dependence of responsivity is expected in these filters in that temperature range. Note that the plot shows the CCD temperature, and not the temperature of the filters. The exact temperature of the filter is uncertain, but a characteristic of these filters is a shift in wavelength toward the red with increasing temperature. Although the temperature coefficients are small (0.015 nm/° at 400 nm and 0.025 nm/° at 1,000 nm), the dispersions in the plots are largest near those filters at the edge of the quantum efficiency curve and so could have a large effect on responsivity. This effect goes in the wrong direction, unless the filter temperature lagged in temperature from the CCD. A second factor that may contribute to the large dispersion is that as the CCD temperature increases, the edges of the band gap widen, which would tend to increase the responsivity, especially at longer wavelengths. Figure 51 shows that around the operating temperature of MDIS, variation in
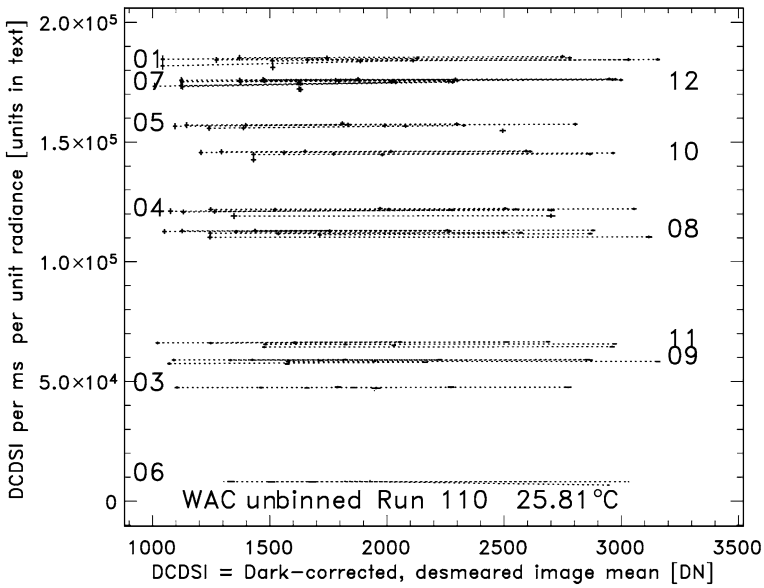
Fig. 48 Full-frame WAC responsivity at CCD temperature 1,267 DN (26°C). Radiance is in units $W\,m^{-2}\,nm^{-1}\,sr^{-1}$. The lines represent different light combinations; groupings of lines correspond to different filters, whose numbers as given in Table 6 are indicated. Note that the broadband filter (02) used for optical navigation was not fully characterized and is not shown
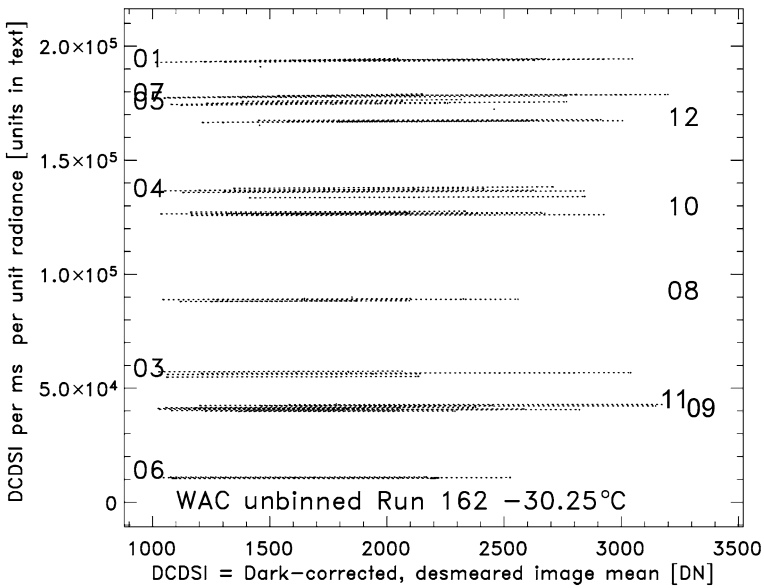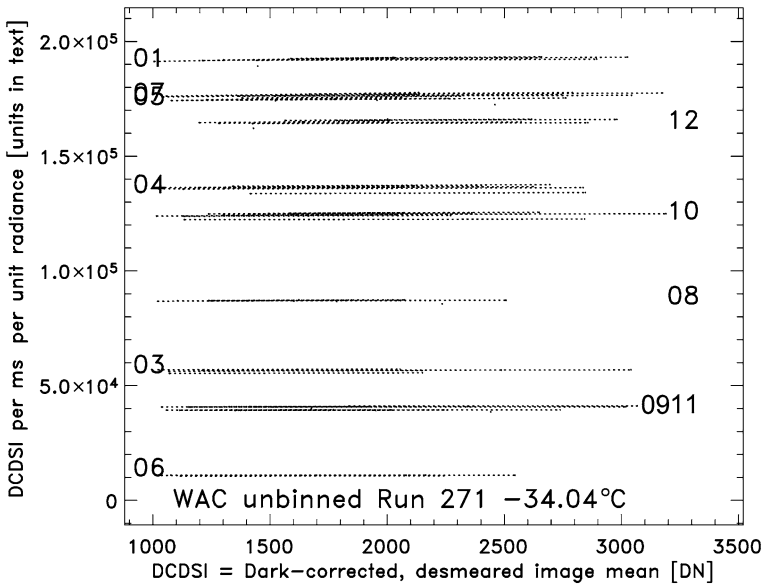

Fig. 49 Full-frame WAC responsivity at CCD temperature 1,060 DN (−30°C). Radiance is in units $W\,m^{-2}\,nm^{-1}\,sr^{-1}$. The lines represent different light combinations; groupings of lines correspond to different filters, whose numbers as given in Table 6 are indicated. Note that the broadband filter (02) used for optical navigation was not fully characterized and is not shown

Fig. 50 Full-frame WAC responsivity at CCD temperature 1,046 DN ($-34°$C). Radiance is in units $W\,m^{-2}\,nm^{-1}\,sr^{-1}$. The lines represent different light combinations; groupings of lines correspond to different filters, whose numbers as given in Table 6 are indicated. Note that the broadband filter (02) used for optical navigation was not fully characterized and is not shown

responsivity is a small effect. For the binned WAC, responsivity is greater than full-frame WAC responsivity by a factor of 4.

Figures 52 and 53 show the responsivities measured for the NAC at cold temperatures. Data points are represented by crosses, which have widths showing 2-σ errors of the dark model and heights showing 2-σ errors in responsivity. Each line connects the responsivities measured at a single sphere radiance through a single filter at different exposure times. Note the highly exaggerated scale; the scatter in the determinations is only about 4%, which is a measure of the absolute accuracy of the radiometric calibration.

Table 12 summarizes the responsivities of the NAC and WAC, both binned and full-frame, at a reference CCD temperature of $-30.3°$C. It is expected that the temperature dependence of responsivity in both cameras over the CCD operating temperature range of $-45°$C to $-10°$C will be approximately quadratic. However, ground-based measurements were acquired only at intermediate temperatures, and therefore the best correction available from these data is linear in form. A second-order correction will be determined from targets of opportunity in flight (e.g., Canopus from Mercury orbit, at which time the CCD temperature will vary over its operational range). The application of the linear correction is

$$R_{f,T,b} = R_{f,-30.3°C,b}\big[correction\_offset_f + T_{CCD}[DN] \times correction\_slope_f\big], \qquad (15)$$

where $R_{f,T,b}$ is responsivity in filter f at CCD temperature T_{CCD} in units of DNs, and b is the binning mode. $R_{f,-30.3°C,b}$ is responsivity in filter f at CCD temperature of 1060 DN ($-30.3°$C) as given in Table 12, and $correction\_offset_f$ and $correction\_slope_f$ are camera- and filter-dependent temperature correction offset and slope, also as given in Table 12. The temperature correction defaults to unity at the reference CCD temperature of $-30.3°$C.

Table 12 WAC and NAC responsivities

Filter number	Responsivity $(DN\,ms^{-1})/(W\,m^{-2}\,nm^{-1}\,sr^{-1})$	Temperature correction offset	Temperature correction slope
WAC full frame			
01	1.9359×10^5	1.249	-2.3460×10^{-4}
02	9.8165×10^4	0.956	4.1897×10^{-5}
03	5.6441×10^4	1.831	-7.8410×10^{-4}
04	1.3643×10^5	1.569	-5.3712×10^{-4}
05	1.7488×10^5	1.533	-5.0237×10^{-4}
06	1.0788×10^4	2.303	-1.2284×10^{-3}
07	1.7803×10^5	1.091	-8.6054×10^{-5}
08	8.8803×10^4	-0.353	1.2761×10^{-3}
09	4.0546×10^4	-1.284	2.1543×10^{-3}
10	1.2662×10^5	0.240	7.1685×10^{-4}
11	4.2273×10^4	-1.855	2.6924×10^{-3}
12	1.6698×10^5	0.746	2.3968×10^{-4}
WAC binned			
01	7.7437×10^5	1.249	-2.3460×10^{-4}
02	3.9266×10^5	0.956	4.1897×10^{-5}
03	2.2576×10^5	1.831	-7.8410×10^{-4}
04	5.4572×10^5	1.569	-5.3712×10^{-4}
05	6.9952×10^5	1.533	-5.0237×10^{-4}
06	4.3152×10^4	2.303	-1.2284×10^{-3}
07	7.1210×10^5	1.091	-8.6054×10^{-5}
08	3.5521×10^5	-0.353	1.2761×10^{-3}
09	1.6219×10^5	-1.284	2.1543×10^{-3}
10	5.0648×10^5	0.240	7.1685×10^{-4}
11	1.6909×10^5	-1.855	2.6924×10^{-3}
12	6.6792×10^5	0.746	2.3968×10^{-4}
NAC full frame			
	3.5504×10^4	1.319	-3.0184×10^{-4}
NAC binned			
	1.3574×10^5	1.133	-1.2592×10^{-4}

Slope and offset are for correction to the average responsivity at a CCD temperature value of $-30.25°C$. Binned responsivity in each filter is four times the full-frame value, but the temperature correction offset and slope are the same

4.6.3 Response Uniformity (Flat Field)

Response uniformity, or flat field, is a measure of pixel-to-pixel variations in responsivity. Measurements of response uniformity of the WAC and NAC were conducted in the OCF, at room temperature and while cold, by imaging the integrating sphere using two 45-W bulbs.

Figure 54 shows a 200-ms-exposure, binned WAC image acquired through the port hole window in the OCF chamber door. As noted earlier, the port hole window is smaller than

Fig. 51 Relative responsivity vs. temperature for unbinned WAC measurements, normalized to the responsivity at −30°C
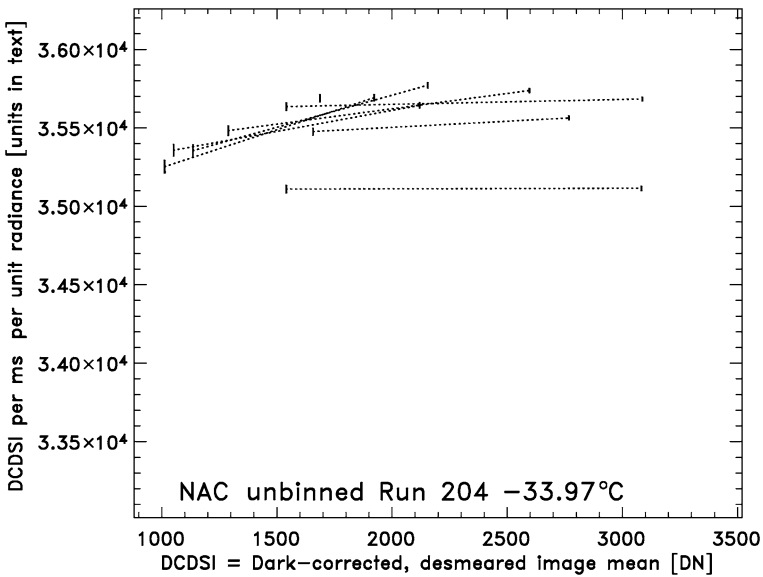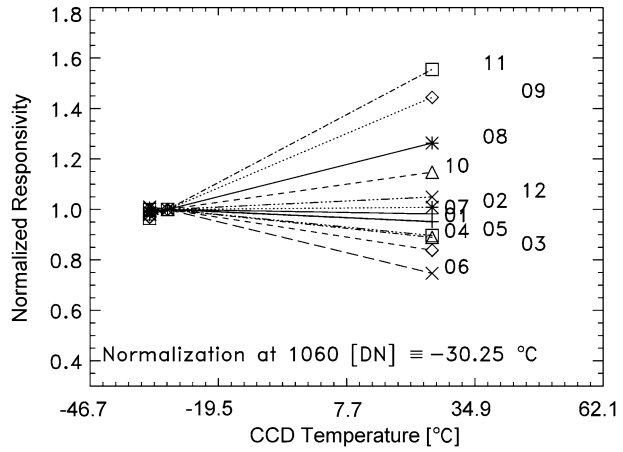

Fig. 52 Full-frame NAC responsivities for CCD temperature 1,057 DN (−34°C). Radiance is in units $W\,m^{-2}\,nm^{-1}\,sr^{-1}$. The lines represent different light combinations

the WAC FOV. Four significant nonuniformities are evident in the data: (1) bright patches around the rim of the sphere opening, nicknamed "clouds," (2) a slight fall-off in brightness with field angle from near the center of the FOV, (3) slight horizontal striping, and (4) darker spots scattered across the FOV. The clouds are believed to be reflections of the integrating sphere off the radiator and thermal blankets that were mounted between the cold wall (on the door) and the chamber door. Removing the thermal blankets in later tests significantly reduced the clouds. The fall-off in brightness with angular distance from the center of the FOV (Fig. 55) is the expected $\cos^4$ fall-off in response with field angle from the optic axis. The horizontal striping is a function of the binning and is absent in the full-frame images.
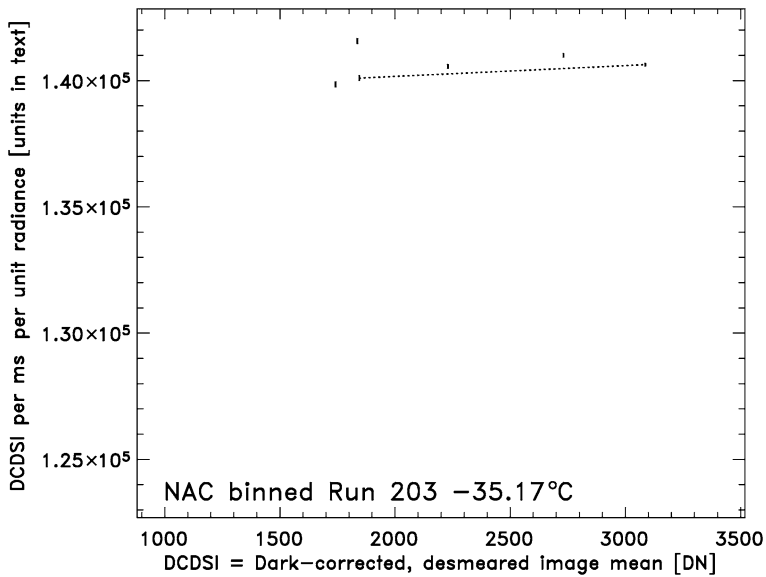
Fig. 53 Binned NAC responsivities for CCD temperature 1,053 DN ($-35.2°C$). Radiance is in units $W\,m^{-2}\,nm^{-1}\,sr^{-1}$

Fig. 54 Nonuniformities are visible in integrating sphere images acquired through the quartz window in the OCF chamber door of the calibration facility
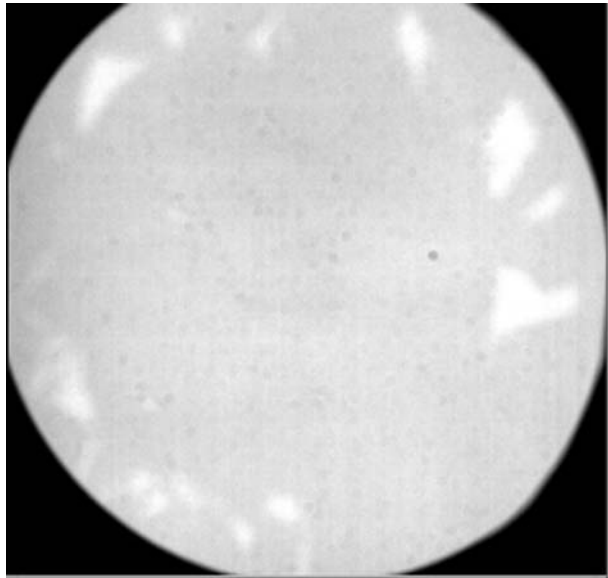
The darker spots scattered across WAC images are fixed with respect to the CCD regardless of filter wheel setting, though their intensities do vary slightly with filter. The sizes of the spots are consistent with shadows of $\ll$35-µm dust on the CCD window, and their number density is consistent with the standards for a class-10,000 clean room in which the camera was assembled. Also consistent with this hypothesis, following instrument vibration during environmental testing, the locations of several spots changed. With the exception of
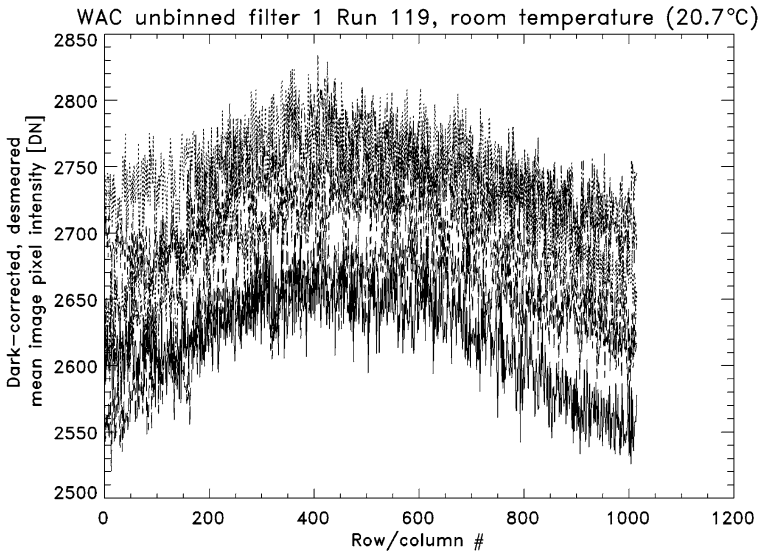
Fig. 55 Profile cuts through an unbinned 699-nm filter WAC integrating sphere image, showing the $\cos^4$ falloff in response off the optic axis. Image is average of 100 images after dark-model and desmearing correction

a single particle (the black spot in the right center of Fig. 54) the dust spots do not significantly affect the DN levels. Given this result, it is likely that the spots themselves will move as the instrument is subjected to the vibrations of launch and flight. Images of the Venus cloud tops acquired during the second Venus flyby will be used to redetermine the flat field post-launch. Preliminary analysis of the flight images acquired thus far shows no significant change in the number or location of spots.

To avoid contaminating flat-field measurements resulting from reflections in the OCF facility, and to avoid having to construct the WAC flat field from tiling image data to form image mosaics, it is desirable to determine the flat field data at room temperature with the door open and the aperture of the camera in close proximity to the integrating sphere aperture. To reduce noise in the derived flat field to approximately 10^{-3}, ~100 images have to be averaged together per filter, camera, and binning mode. Figures 56 and 57 compare the central portions of binned, corrected, and averaged WAC integrating sphere images acquired at room temperature and at cold temperature, respectively. When the images are dark-subtracted, desmeared, averaged, and normalized to the image mean, the relative DN levels are nearly identical on a pixel-by-pixel basis. Since the data are in good quantitative agreement regardless of physical temperature, the flight flat-fields are derived from room-temperature, door-open images.

Full-frame and binned flat fields are shown in Figs. 58 and 59, respectively. The values are normalized to unity in the central part of the images used for responsivity determinations, so that updates to responsivity from non-field-filling sources and to flat field from field-filling sources can be decoupled. The NAC flat field is shown in the upper right panel in both figures, and the 11 narrow-band WAC filters are shown in the remaining panels. Because the spots in the NAC images were not observed to move during environmental qualification of the instrument and they are immobile relative to the detector, redoing the NAC flat field in-flight is not a requirement for the NAC as it is with the WAC.

Fig. 56 Contrast-enhanced, room-temperature, binned WAC integrating sphere image with chamber door open

WAC binned Run 118 Filter 07 at 23.1° C
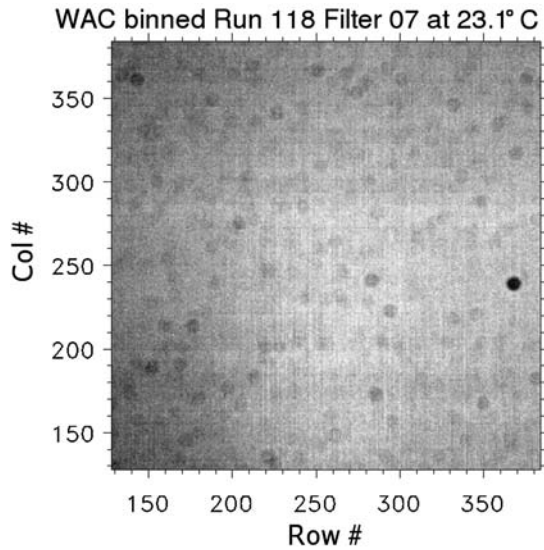
Min 2103.99 mean: 2214.67 Max: 2279.00 [DN]

Fig. 57 Contrast-enhanced, cold, binned integrating sphere image with chamber door closed

WAC binned Run 244 Filter 07 at -43.0° C
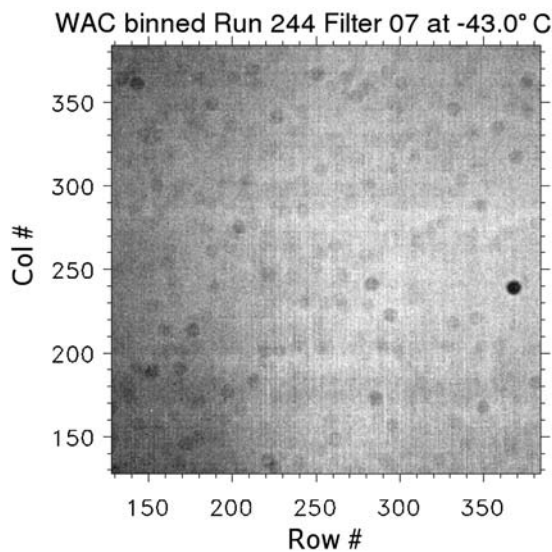
Min 1960.43 Mean: 2069.37 Max: 2128.36 [DN]

4.7 Point Spread Function

The point spread function (PSF) is a measure of the two-dimensional distribution of the radiance measured at the detector emanating from a point source. For a conceptual but non-physical imager, light emanating from a point would all fall into a single detector element. In practice the PSF is broadened by diffraction, surface imperfections of optical elements, and scatter centers on optical surfaces. The expected size of the Airy disk (approximately,
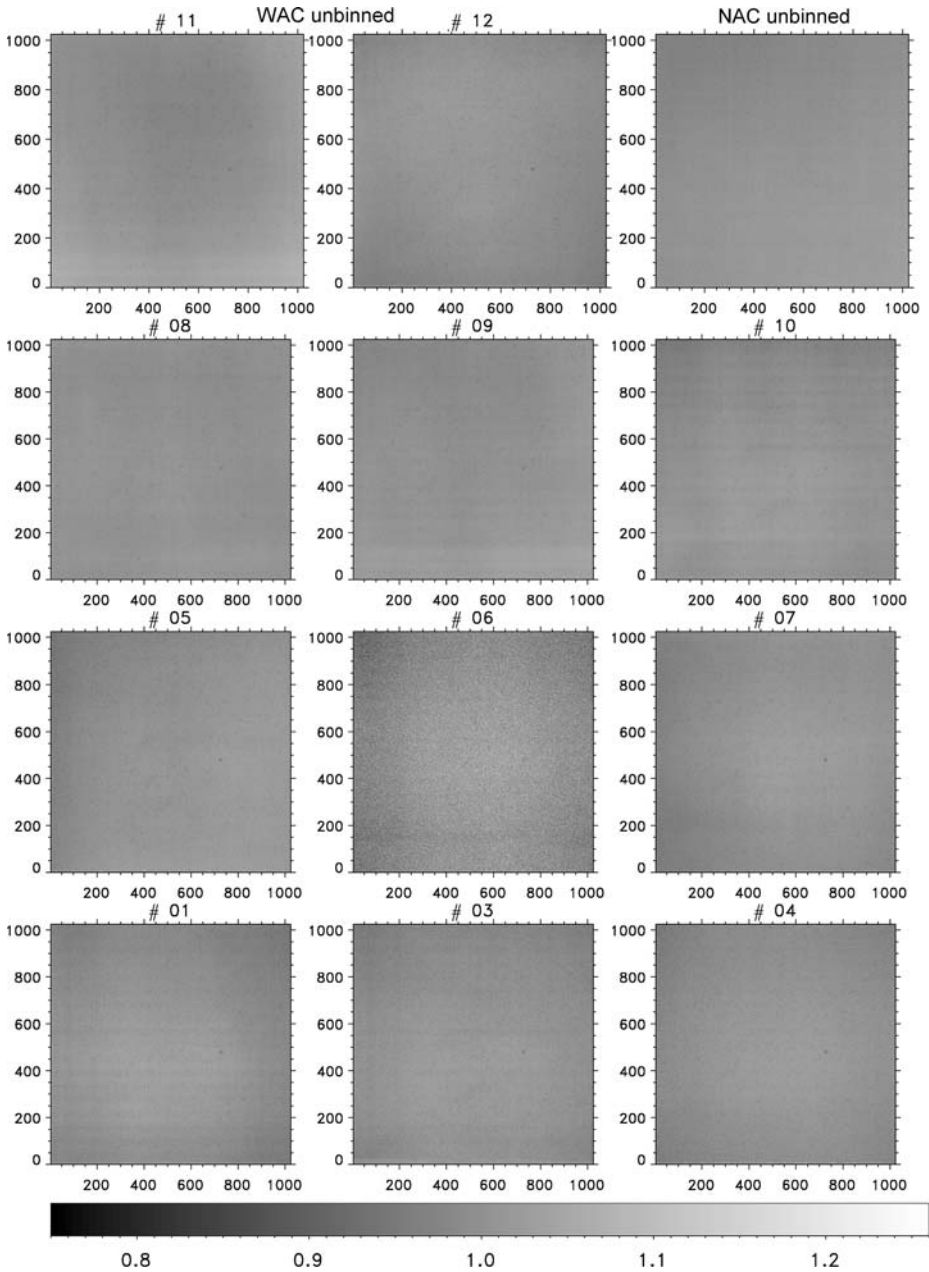
Fig. 58 Contrast-enhanced, unbinned flat fields

the FWHM of the PSF including only effects of diffraction) is >2 pixels for the NAC and ~1 pixel for the WAC. In the particular case of the NAC, the PSF is significantly broader than if the system were purely diffraction limited at the NAC focal length. For nadir imag-
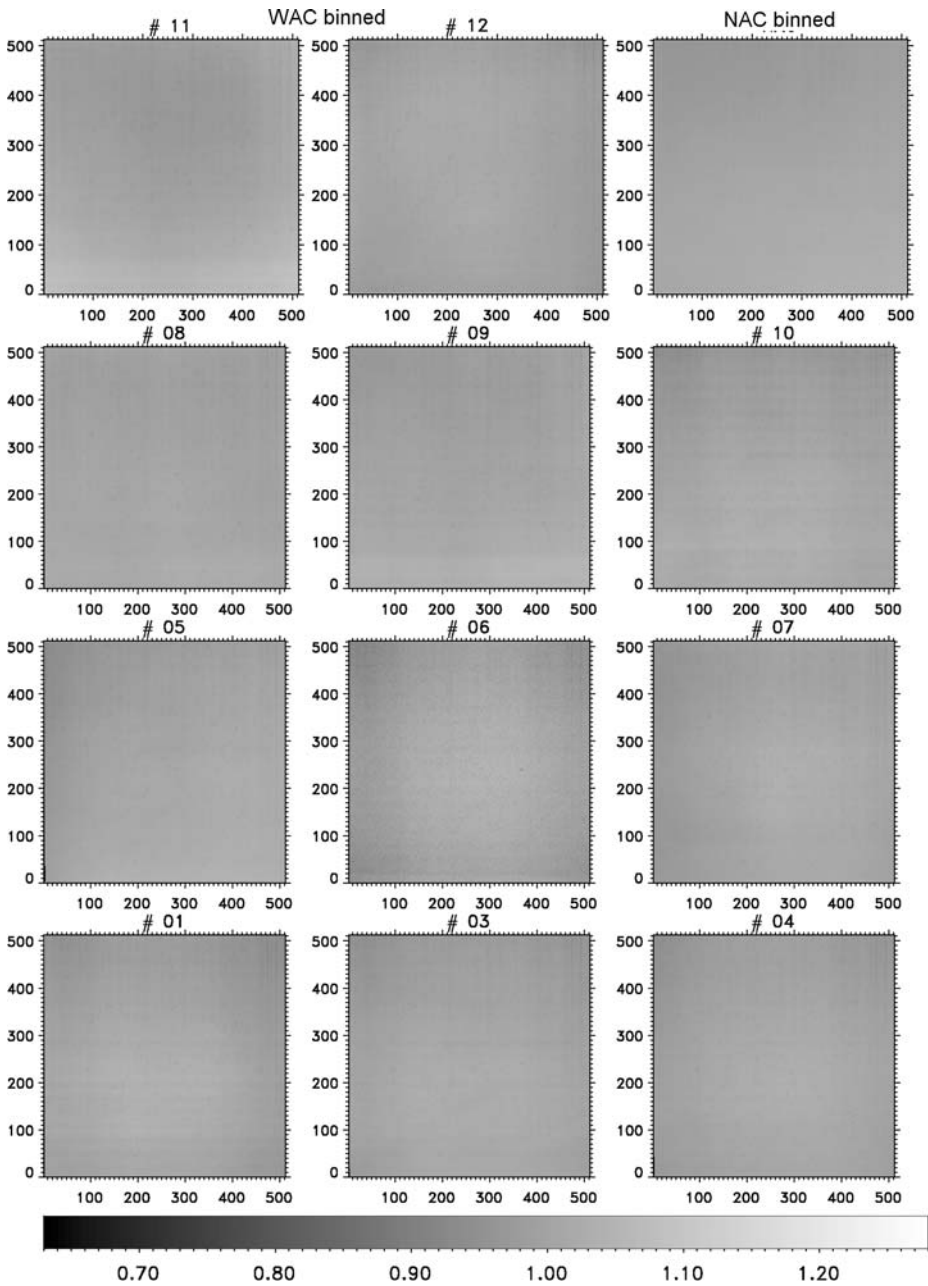
Fig. 59 Contrast-enhanced, binned flat fields

ing at high southern latitudes, this degradation will limit effective sampling of the surface to significantly worse than the desired 250 m/pixel spatial sampling.

The approach adopted for the NAC was to characterize carefully the PSF during ground testing and use Fourier image restoration (optimal filter) techniques to improve the PSF dur-

Fig. 60 Effect of image
restoration using the optimal
filter on an MDIS NAC image of
the Moon obtained during Earth
flyby. The *left* image is before
PSF correction

MDIS NAC PSF correction: pre-launch data, k=3e-12
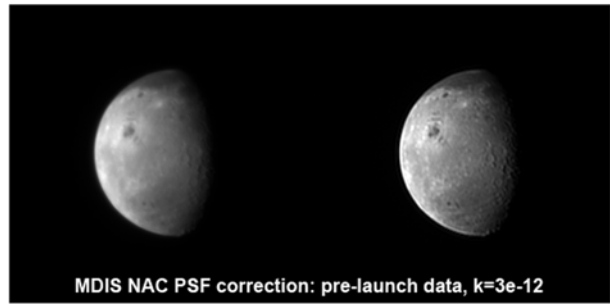
ing calibration. A similar strategy was applied to NEAR images to remediate PSF degrada-
tion due to contaminants on the imager's optics (Li et al. 2002). The optimal filter deblurring
algorithm can be presented as

$$I = CF \frac{|H|^2}{H(|H|^2 + K)}, \qquad (16)$$

where I is the deblurred image, F is the original, calibrated image in units of radiance, H is
the PSF, $|H|^2$ is the norm of complex number H (the square root of the sum of the squares
of the real and imaginary parts of H), K is an empirically determined noise constant, and C
is an empirically determined constant that maintains radiometric accuracy. K is determined
as a value that provides the most sharpening of an image before "ringing" is introduced
at abrupt bright-dark boundaries. The output of the correction is in arbitrary units that are
directly proportional to the input units of radiance, so C is the ratio of the summed pixel
values in the original and deblurred images.

For the deblurring procedure to work effectively, C and K must be validated across a
variety of scenes, and the PSF must be both well determined and nearly constant across
an image. In the case of the NEAR imager, these constraints were all satisfied. There is
no requirement, however, that the PSF be radially symmetric about its central pixel. The
effectiveness of the procedure is shown in Fig. 60, a NAC image of the Moon acquired
during the MESSENGER Earth flyby.

For the NAC, the PSF was assembled from images of a subpixel pinhole imaged in white
light at the focus of the OCF collimator. Multiple exposure times were used, the lowest of
which is unsaturated, and the longer of which are progressively more saturated. At each
exposure time, multiple images are acquired. After correction for dark level, frame transfer
smear, and flat-field nonuniformity, the images are divided by exposure times to convert to
units of DN. The multiple images at each exposure time are averaged to improve statistics.
Starting with the longest exposure, saturated parts of the corrected, averaged image are ze-
roed out and replaced with unsaturated parts of the next longest exposure. The procedure
is continued until the central pixel is reached, and finally all values are normalized to that
of the central pixel. This procedure to assemble the PSF is repeated over a 3×3 grid of
positions within the FOV (center, corners, and edges) to assess uniformity of the PSF across
the FOV.

Figure 61 shows the 3×3 grid of NAC PSFs, displayed using a linear stretch between 0
and 1. The brightest part of the PSF exhibits its expected 2–3 pixel diameter, and the PSF is
closely similar across the FOV; there is no evidence for shapes of the PSF that are related
to position or distance relative to the optic axis. Figure 62 shows the PSFs similarly, except
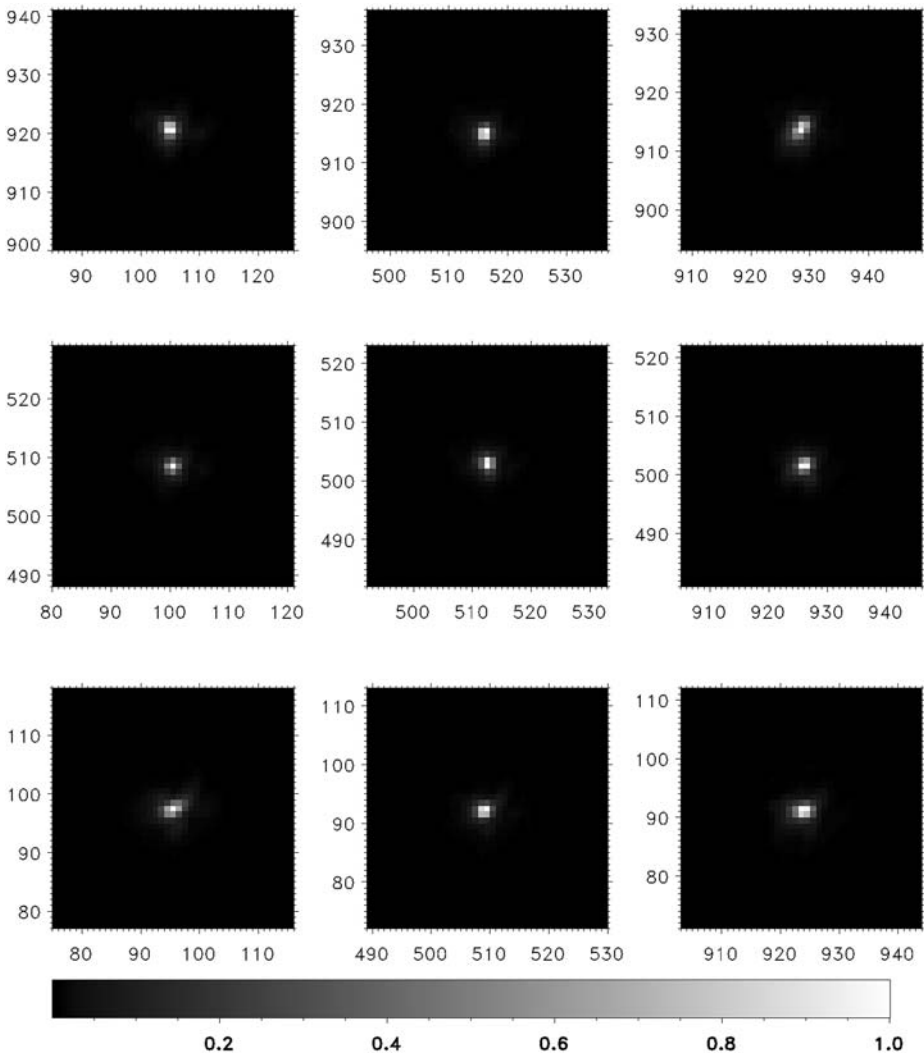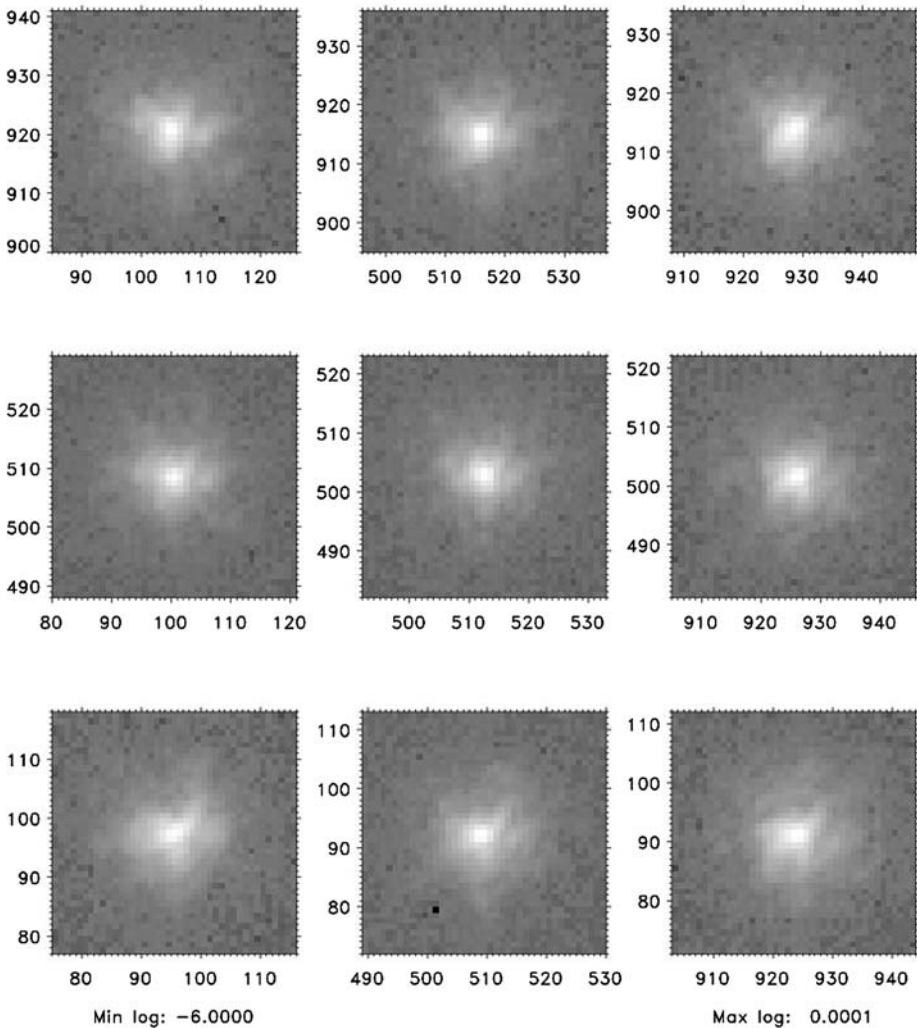displayed using a logarithmic stretch between 10^{-6} and 1. The shape of the PSF is well

Fig. 61 Two-dimensional intensity distribution of the NAC point spread function, at a 3×3 grid of positions across the FOV. The ordinate and abscissa are labeled with pixel location. Pixel $(0, 0)$ corresponds to the lower left. The stretch is from 0 to 1

determined out to a radius of 10 pixels. The shape is not exactly radially symmetric, but it does appear nearly uniform across the FOV. Thus, the measured NAC PSF appears perfectly suited to application of the optimal filter to improve effective spatial sampling of Mercury in the NAC.

5 Mission Operations and Data Products

The MESSENGER Mission Operations Center (MOC) (Holdridge and Calloway 2007) will conduct most spacecraft activities with reusable command sequences. These activities will

Fig. 62 Two-dimensional intensity distribution of the NAC point spread function, at a 3 × 3 grid of positions across the FOV. The ordinate and abscissa are labeled with pixel location. Pixel $(0, 0)$ corresponds to the lower left. The stretch is logarithmic from 10^{-6} to 1

be translated into time-tagged commands that call macros prepared, uploaded, and verified by the MOC using the MESSENGER planning and scheduling system. Typically these activities will include recorder operations, DSN track activities, and orbital and attitude maneuvers and the integration of instrument operations. Instrument commands and housekeeping commands will be merged at the MOC, and the sequences will be checked to ensure that all activities are within operational limits and within available spacecraft resources (e.g., memory, power, thermal, recorder).

These reusable command sequences are built by the MOC with input from the subsystem and instrument engineers. The sequences are built from a hierarchy of command groups. The lowest level consists of fragments, which include one or more commands (with defined rel-

ative timing) required to implement simple actions on a single instrument or subsystem. The next level consists of Canned Activity Sequences (CASs). A CAS includes one or more fragments with defined relative timing required to perform an entire activity. This activity may cross subsystem boundaries. CASs and fragments usually have input parameters to provide flexibility in use, e.g., logic, timing, and command parameter values. An example of a CAS would be an Optical Navigation Sequence, which first commands the Guidance and Control (G&C) subsystem to point the spacecraft at a star using G&C fragments. MDIS is then commanded to take images using MDIS fragments. These CASs and fragments are tested with hardware and software simulators and are configured on the planning and scheduling system. The highest command level is the request, which calls one or more of these CASs and associates a real spacecraft time and a set of input parameters defining each instantiation of each CAS. Request files are created by the MOC for spacecraft commanding and the science teams for instrument commanding. The concept of CASs and fragments is essential to the philosophy of reusing pretested command blocks to save time in the preparation and validation of spacecraft activities.

The MOC compiles spacecraft and instrument flight rules and operational constraints. This rule set is translated into software run on the ground in the planning and scheduling system. These rules assist the MOC and the science team in flagging command sequences that may put the spacecraft or instruments in improper configurations, exceed onboard resources (e.g., CPU memory, SSR space), or pass parameters to CASs and fragments that are not permitted. These flagged errors are eliminated by adjusting timing between CASs, altering CAS input parameters, or changing which CASs are used to make the command sequence.

6 Data Acquisition Strategy

6.1 Flyby Imaging

The MESSENGER trajectory provides three flyby opportunities of Mercury: January 2008, October 2008, and September 2009 (Table 2, Fig. 63). During the first flyby, approximately half of the hemisphere not viewed by Mariner 10 will be illuminated (subsolar longitude
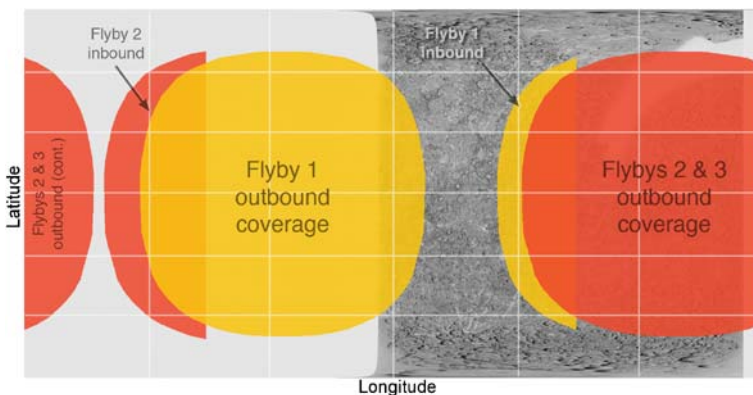

Fig. 63 Preliminary map, in simple cylindrical projection, of MDIS flyby imaging coverage at ≤500 m/pixel (at subspacecraft point) from a range of 20,000 km and emission angle ≤70°

190°E); the first Mercury data return from MESSENGER will thus observe new terrain, including the previously unseen western half of the Caloris basin and its ejecta. During the second flyby, illumination will be centered on the eastern edge of the Mariner 10 hemisphere (subsolar longitude 4°E). The lighting geometry for the third encounter will be nearly identical to that of the second encounter with the subsolar point at the prime meridian (0°E); the approach and departure phase angles will be less extreme, however, resulting in better inbound imaging. During the second and third flybys, most of the remaining unseen portion of Mercury will be imaged. Total coverage between Mariner 10 and the three flybys will exclude only the poles and a small longitudinal gap ∼6°-wide, centered at ∼97°E longitude. Due to the equatorial closest approach on all three flybys, resolution will diminish towards the poles and limb.

Image mosaics from the various photometric geometries obtained during the flybys and from orbit will require an accurate photometric model of the planet at the wavelengths of the NAC and WAC filters. Therefore, MESSENGER will perform a sophisticated photometric characterization of Mercury's surface from data acquired during the flybys, as well as during orbital operations, through observations of the same point on the ground acquired at various emission, incidence, and phase angles. During each flyby one area on the surface will be observed at 11 different phase angles in 10° increments. Because of Mercury's slow rotation these observations will have a fixed incidence angle—only the emission and phase angles will change.

6.2 Orbital Imaging

Global Monochrome Basemap. One of the primary goals of MDIS is to acquire a global monochrome base map at 250-m/pixel average spatial sampling, low emission angle, and moderate incidence angle. For a given area coverage is obtained at the first opportunity when local nadir is viewed at solar incidence angles of 55–75°. Selection of the combination of emission and incidence angles dictates that the spacecraft will be nearly in a dawn–dusk orbit, minimizing thermal disturbances to pointing. The choice of NAC or WAC is driven by the necessity of maintaining both cross-track overlap and near uniform spatial resolution (140 m/pixel, Fig. 64): the NAC will be used to image the southern hemisphere, whereas the WAC will be used in the northern hemisphere (Fig. 64). For monochrome imaging, the 750-nm filter is used in the WAC to match the 750-nm filter of the NAC. The global nadir-viewing basemap is planned for completion during the first Mercury solar day (i.e., during the first half of the orbital mission).

Stereo Mapping. The off-nadir stereo-complement to the basemap will consist of images taken at nearly the same local solar time. This situation occurs with the spacecraft in the same nearly dawn–dusk orbit, again minimizing the thermal disturbance to pointing and the propagation of pointing uncertainty into uncertainty in southern-hemisphere elevations. Off-nadir pointing will be accomplished using the capability of the guidance and control system to point up- or down-track by commandable offsets.

The downlink profile over the course of the orbital mission is heavily front-loaded due to favorable Earth–Mercury distance, so the off-nadir complement will be time-phased to take advantage of this high downlink rate. In the southern hemisphere, stereo mapping will be accomplished entirely during the first solar day. Imaging on one orbit will be at nadir (0° emission), then on the next orbit off-nadir (25° emission), and the sequence will be repeated so that nadir and off-nadir mapping will be built up simultaneously. The northern hemisphere will be imaged at nadir on the first solar day, then on the second solar day the same image sequence will be repeated off-nadir, covering locations at the same local solar time as in the nadir map. The vertical precision of the stereo map will typically be about 100 m.
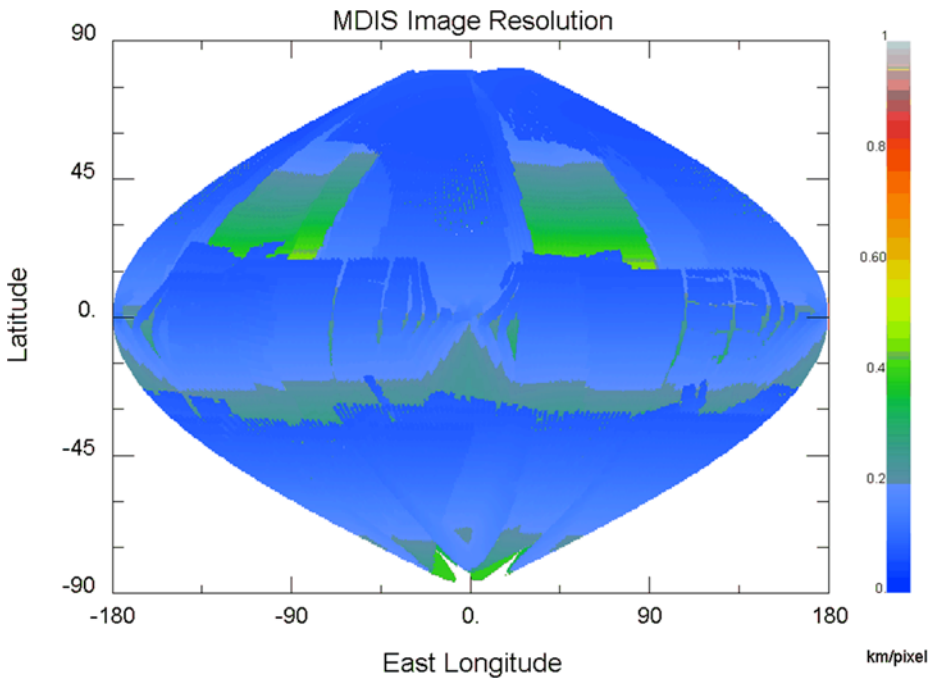
Fig. 64 Preliminary map of spatial sampling in the MDIS global base map, in simple sinusoidal projection

Gap-filling the Flyby Color Map. Once in orbit, the remaining gaps in the flyby color maps will be filled. Details of the mapping strategy are still under development, but acquisition will mesh with the global monochrome and stereo mapping. The southern hemisphere will likely be imaged as mosaics centered on given latitudes and longitudes, while the northern hemisphere will probably be imaged as strips that are pixel-binned on-chip, in order to obtain images in a greater number of filters with no gaps.

Polar Mapping. In order to identify permanently shadowed (and permanently illuminated) areas, polar regions will be imaged repeatedly throughout the Mercury solar day. Over two orbits (24 hours), the subsolar longitude will change by only ∼2°. This strategy provides coverage of all areas near their minimum solar incidence angle. Coverage will extend from 85° or lower latitude to the pole on the night side, and from 80° or lower latitude to the pole on the dayside. At the south pole, the campaign will be divided between the two solar days. On the first solar day, the WAC will be used while the spacecraft is at high altitude, providing ∼1.5 km spatial sampling and extending equatorward to approximately 70° latitude on the dayside. On the second solar day a more limited region will be covered at higher resolution, using one 2 × 3 NAC mosaic per day with its long axis aligned north–south. The latter provides about 200 m/pixel spatial sampling.

For the northern polar region, the entire first solar day is required for the monochrome base map, so the polar campaign will be delayed until the second solar day. The WAC will be used because its wider FOV is required for latitude coverage. The imaging strategy will parallel that used for the NAC in the southern polar region, using one 2 × 3 mosaic per day with its long axis aligned north–south.

High-Resolution Imaging.   Selected areas of the northern hemisphere, identified for the most part in flyby imaging, will be imaged from orbit at resolutions of up to ∼20 m/pixel. For this purpose the NAC has a "fast" 1-Hz mode, which will acquire images binned 2×2 on-chip in continuous strips 512 pixels wide. At low dayside altitudes (280 km), spatial sampling is 11 m/pixel but along-track motion smear is 18 m at the shortest exposure, consistent with low artifacts from frame transfer smear. Because of MESSENGER's highly eccentric orbit, high-resolution imaging is possible only in the northern hemisphere.

Targeted Color.   Selected regions of the planet will be targeted on the second solar day for full-resolution color imaging with spatial sampling up to ∼400 m/pixel using the ability of the guidance and control system to track a commanded latitude and longitude on the surface. The maximum spacecraft angular velocity dictates the minimum altitude and thus best spatial sampling at which this imaging can be done. Initial targets will be identified from Mariner 10 data and MESSENGER flyby results.

Color Photometry.   During the orbital phase of the mission, photometric geometry complementary to that measured during the flybys is possible: incidence angle variations will be measured at nearly constant emission angle. Key features in low southern latitudes will be imaged repeatedly while the spacecraft is high (10,000 km) above high southern latitudes as the subsolar point moves from terminator to near noon-time. Several target areas will be selected: one to represent average Mercury (heavily cratered highlands), another representing intercrater plains, and a third representing smooth plains materials (probably Tolstoj plains).

Including the flyby and orbital observations, the photometric properties of Mercury will be characterized over greater than 80° of emission angle, 100° of phase angle, and 80° of incidence angle. Results from this experiment will not only characterize photometric properties of the surface but also photometric normalization to a standard geometry (30° solar incidence angle, 0° emission angle) for production of mosaicked products.

On-orbit Calibrations.   In order to maintain accuracy of southern-hemisphere elevation measurements, pointing calibrations will be interleaved with nadir and off-nadir global mapping. Once or twice per orbit, depending on orbital geometry, MDIS will be pointed off the planet using the pivot at least at two different pivot angles, permitting star images to be acquired using the WAC. Subframes centered on stars will be used to minimize the data volume required. On-ground, these data will be used to solve for pivot plane orientation as a function of temperature at the base of MDIS.

The MESSENGER project will archive all MDIS Experiment Data Records (EDRs) and Reduced Data Records (RDR) with the Planetary Data System (PDS) in a timely fashion (Table 13). EDRs consist of the raw image data (DNs) fully documented in terms of geometric and radiometric variables. In addition to the raw images, the MESSENGER project will also archive radiometrically corrected versions in units of I/F or radiance, as appropriate. The information contained in this paper and prelaunch calibration files archived with the PDS will allow a user to apply any advances to the state of calibration as needed to the original raw EDRs.

Critical science observations will be obtained during the three Mercury flybys and are of four basic types:

- quadrature monochrome NAC mosaics (200–600 m/pixel),
- medium-resolution NAC quadrature stereo mosaics,

Table 13 MESSENGER MDIS EDR delivery schedule to PDS

Mission data	Product	MESSENGER planned delivery date
Prelaunch calibration	EDR	6 months after launch
Earth flyby	EDR	6 months after 2nd Venus flyby encounter
Venus flyby 1	EDR	6 months after 2nd Venus flyby encounter
Venus flyby 2	EDR	6 months after 2nd Venus flyby encounter
Mercury flyby 1	EDR	6 months after 1st Mercury flyby encounter
Mercury flyby 2	EDR	6 months after 2nd Mercury flyby encounter
Mercury flyby 3	EDR	6 months after 3rd Mercury flyby encounter
Mercury orbit	EDR	every 6 months after Mercury orbit insertion

- synoptic 11-color mosaics (1–8 km/pixel), and
- approach and departure movies (4.4–18 km/pixel).

Data products from these observations will serve as the foundation for assessing the orbital mapping strategy and planning special targeted, high-resolution sequences. RDR products associated with the flyby observations will be reviewed and archived with the PDS on a schedule similar to that for the EDRs.

During orbital operations systematic mapping with both the NAC and WAC will result in:

- a global monochrome basemap with an average resolution of 250 m/pixel,
- merged flyby and orbital multispectral cubes and mosaics in up to 11 spectral filters at ∼1 km/pixel,
- local stereo-based digital elevation models, and
- very-high-resolution NAC local strip mosaics in the northern hemisphere (best resolutions ∼20 m/pixel).

7 Conclusion

The MDIS instrument and its associated DPU form an integral part of the MESSENGER science payload. MDIS will provide critical measurements tracing Mercury's origin and evolution. The pivoting design of MDIS provides for an extra degree of freedom to map the surface of Mercury and acquire critical optical navigation images without violating the stringent Sun-keep-in rules to maintain the spacecraft sunshade in its proper orientation. The innovative thermal design ensures that the MDIS detectors remain within their operating temperature range even during periapsis at local noon.

On August 3, 2004, the MESSENGER spacecraft was launched from Cape Canaveral, FL. At the time of this writing, all aspects of the instrument have been tested in flight and verified to be working as designed. On May 11, 2005, when the spacecraft was 29.6 million km from Earth, the spacecraft was commanded to look toward the Earth to test the pointing of the MLA instrument. Figure 65 shows one of the six images snapped of the ∼0.43 mrad (18-pixel) Earth as observed by the MDIS NAC. In this same frame we observed another bright object—the Moon. This serendipity bodes well for the discoveries yet to be made at Mercury by MDIS and the entire MESSENGER science payload.

Fig. 65 Taken May 11, 2005, this processed image comes from the NAC when MESSENGER was about 29.6 million kilometers from Earth. The Moon is visible in this frame, but its contrast has been enhanced. Although the Earth only subtends about 18 pixels, bands of clouds between North and South America are apparent on Earth's sunlit side
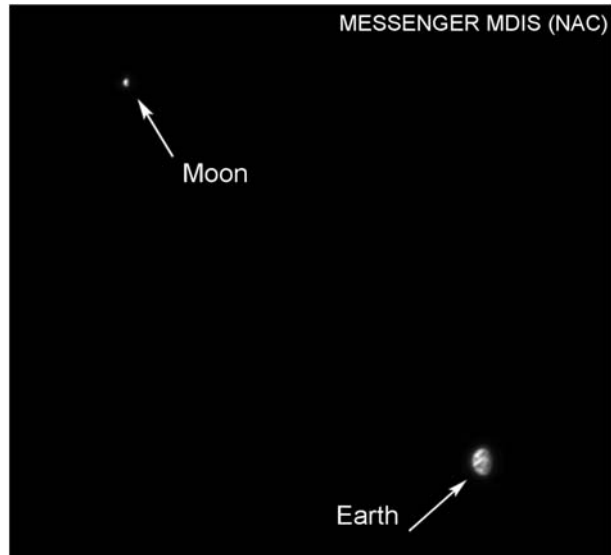
Appendix 1: Radiation Effects on Filters

We deemed it necessary to characterize the degradation in transmission in the long-pass filter glasses used in the WAC by exposure to ionizing radiation. This appendix summarizes the experimental setup and the results of those measurements.

The manufacturer-provided specifications for the Schott colored glass filters were closely matched to the flight filters. The 25-mm diameter filters were 3.00 ± 0.25 mm thick. The polished surfaces had a surface quality of 80–50 scratch and dig and parallelism to 2 arcminutes. Only one filter, S8612, was 0.5 mm thick.

The equipment used in this experiment included a 0.75-m focal length triple-grating imaging monochromator/spectrograph with a sample holding cell, a stabilized light source, a silicon photodiode detector, and a computer-controlled six-slot filter wheel. All data collection was accomplished with a desktop computer to provide control of the monochromator. A ^{60}Co radiation source chamber was used to irradiate the samples.

The transmission of each test filter was measured prior to any exposure to radiation in order to establish the baseline. The test filters were irradiated in a sealed chamber containing a ^{60}Co source and received radiation at a rate of approximately 0.18 krad per minute. The error introduced in the actual dose due to the time taken to lower and raise the samples from the chamber is estimated to be $\pm 5\%$.

The experimental arrangement to measure the transmission of the test filters is shown in Fig. 66. Light from the stabilized source passes through the monochromator order-sorting filter wheel and enters the monochromator through a variable-width slit; it exits on the opposite side through a similar slit to which the sample holding cell is attached. The sample cell consists of a collimating lens, a sample holding base, and another lens to refocus the image

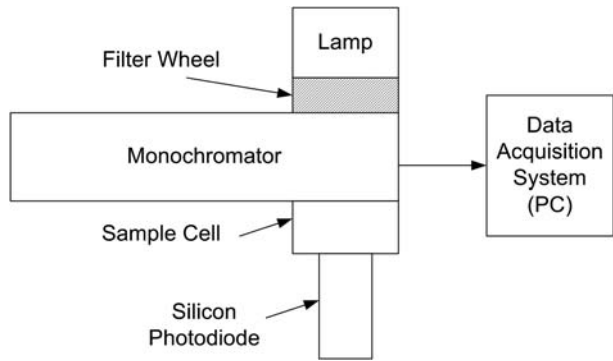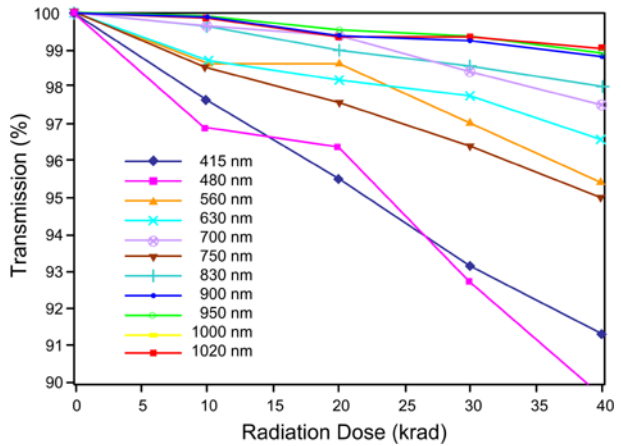**Fig. 66** Experimental test setup for measuring effect of radiation on MDIS filter glasses

Fig. 67 Inferred transmission loss over passbands of WAC filters as a function of radiation dose

onto the silicon photodiode for measurement Every transmission test followed the same test sequence under the same environmental conditions.

A transmission test sequence included acquiring dark measurements for background subtraction to ensure that only the light passing through the filter was considered in the test. The lamp was turned on and allowed to warm up for ten minutes before the test sequence began. Once the lamp warmed up its spectrum was measured with no filter present. The transmission of the short-wavelength filters was recorded over the range 350–650 nm with no order-sorting filter present in the monochromator beam. The longer-wavelength filters were scanned over the range 650–1,100 nm with an order-sorting filter that attenuated all wavelengths below 550 nm in the beam. The spectrum of the lamp was recorded midway through the measurements and at the end of the filter measurements to verify that the stability of the lamp was below 0.2%. At the end of the filter measurements, the lamp was turned off and a spectrum of the background was taken. Finally, the filter transmissions were calculated by subtracting the dark signal from the values and dividing the filter signal by the lamp-only signal.

The measured transmissions of the test filter glasses generally show a drop of transmission with radiation dose that is wavelength dependent. The maximum transmission of the filters, roughly 90%, is limited by the reflection loss from the surfaces. The loss of transmission as a consequence of radiation is smaller at the longer wavelengths. This trend occurred for each individual filter and continued from filter to filter.

The transmission of the glass filters over the WAC filter passbands was inferred by averaging the results for the test filter glasses over the spectral passband for which they are used in each WAC filter. Figure 67 shows the transmission variation with radiation dose relative to the transmission before irradiation. The transmission loss was observed to decrease with increasing wavelength. The legend in the graph identifies the filter for each curve. Note that these curves are for 2-mm thick glass samples, whereas the actual thicknesses may be as high as 2.93 mm. At the estimated mission radiation dose of ∼15 krad the transmission loss will be <4% in the worst case and will average to <2% for all the filters. In-flight calibration will be used to track this change if it is measurable.

References

G.B. Andrews et al., Space Sci. Rev. (2007, this issue). doi:10.1007/s11214-007-9272-5

D.T. Blewett, P.G. Lucey, B.R. Hawke, G.G. Ling, M.S. Robinson, Icarus **129**, 217–231 (1997)

J.F. Cavanaugh et al., Space Sci. Rev. (2007, this issue). doi:10.1007/s11214-007-9273-4

B.M. Cordell, R.G. Strom, Phys. Earth Planet. Interiors **15**, 146–155 (1977)

E.H. Darlington, M.P. Grey, Proc. SPIE **4498**, 197–206 (2001)

R.E. Gold, R.L. McNutt Jr., S.C. Solomon, the MESSENGER Team, in *Proceedings of the 5th International Academy of Astronautics International Conference on Low-Cost Planetary Missions*, ed. by R.A. Harris. Special Publication SP-542 (European Space Agency, Noordwijk, 2003), pp. 399–405

O.L. Hansen, Astrophys. J. **190**, 715–717 (1974)

J.K. Harmon, M.A. Slade, Science **258**, 640–643 (1992)

J.K. Harmon, P.J. Perillat, M.A. Slade, Icarus **149**, 1–15 (2001)

S.E. Hawkins, III et al., Space Sci. Rev. **82**, 31–100 (1997)

M.E. Holdridge, A.B. Calloway, Space Sci. Rev. (2007, this issue). doi:10.1007/s11214-007-9261-8

J.R. Janesick, *Scientific Charge-Coupled Devices*. SPIE Press Monograph PM83 (SPIE, Bellingham, WA, 2001), 920 pp

W.S. Kiefer, B.C. Murray, Icarus **72**, 477–491 (1987)

J.C. Leary et al., Space Sci. Rev. (2007, this issue). doi:10.1007/s11214-007-9269-0

J.S. Lewis, Earth Planet. Sci. Lett. **15**, 286–290 (1972)

J.S. Lewis, Ann. Rev. Phys. Chem. **24**, 339–351 (1974)

H. Li, M.S. Robinson, S. Murchie, Icarus **155**, 244–252 (2002)

H.J. Melosh, D. Dzurisin, Icarus **35**, 227–236 (1978)

H.J. Melosh, W.B. McKinnon, in *Mercury*, ed. by F. Vilas, C.R. Chapman, M.S. Matthews (University of Arizona Press, Tucson, 1988), pp. 374–400

S. Murchie et al., Icarus **140**, 66–91 (1999)

S. Murchie et al., Icarus **155**, 229–243 (2002)

B.C. Murray, J. Geophys. Res. **80**, 2342–2344 (1975)

B.C. Murray, R.G. Strom, N.J. Trask, D.E. Gault, J. Geophys. Res. **80**, 2508–2514 (1975)

J.B. Pechmann, H.J. Melosh, Icarus **38**, 243–250 (1979)

A. Potter, T.H. Morgan, Science **229**, 651–653 (1985)

A. Potter, T.H. Morgan, Icarus **67**, 336–340 (1986)

B. Rava, B. Hapke, Icarus **71**, 397–429 (1987)

M.S. Robinson, P.G. Lucey, Science **275**, 197–200 (1997)

M.S. Robinson, J.G. Taylor, Meteorit. Planet. Sci. **36**, 841–847 (2001)

M.A. Slade, B.J. Butler, D.O. Muhleman, Science **258**, 635–640 (1992)

S.C. Solomon et al., Planet. Space Sci. **49**, 1445–1465 (2001)

P.D. Spudis, J.E. Guest, in *Mercury*, ed. by F. Vilas, C.R. Chapman, M.S. Matthews (University of Arizona Press, Tucson, 1988), pp. 118–164

R.G. Strom, Phys. Earth Planet. Interiors **15**, 156–172 (1977)

R.G. Strom, N.J. Trask, J.E. Guest, J. Geophys. Res. **80**, 2478–2507 (1975)

N.J. Trask, J.E. Guest, J. Geophys. Res. **80**, 2462–2477 (1975)

F. Vilas, in *Mercury*, ed. by F. Vilas, C.R. Chapman, M.S. Matthews (University of Arizona Press, Tucson, 1988), pp. 59–76.

T.R. Watters, M.S. Robinson, C.R. Bina, P.D. Spudis, Geophys. Res. Lett. **31**, L04701 (2004)

G.W. Wetherill, Geochim. Cosmochim. Acta **58**, 4513–4520 (1994)

D.E. Wilhelms, Icarus **28**, 551–558 (1976)